Durham E-Theses

Lipid Bilayers on Deformable Elastic Substrates

STUBBINGTON, LIAM,THOMAS,EDWARD

How to cite:

Use policy

Lipid Bilayers on Deformable Elastic Substrates

Durham University

Submitted in partial fulfilment of the requirements for the degree of

Doctor of Philosophy

Liam Stubbington

June 2018

Abstract

In this thesis an experimental model for the interface between the cell membrane and the supporting cytoskeleton has been developed and analysed. The experimental platform is a novel approach to the design of supported membrane based devices and technologies.

The system consists of a single component lipid bilayer coupled to an elastic substrate, the area of which can be reversibly increased and decreased. We uncover three independent mechanisms that the membrane may use to respond to changes in substrate area.

If the elastic support is partially hydrophilic, the area of the planar portion of the membrane is strongly coupled to the substrate area. The membrane responds to increasing substrate area by absorbing lipid protrusions, and when the substrate area is decreased the excess membrane area is projected back out in the form of lipid tubes. This mechanical remodelling of the membrane occurs above the plane of the support and mimics the passive means of membrane area regulation recently uncovered in live cells.

In contrast, when the surface support is completely hydrophilic, two further mechanisms of substrate stress relaxation are uncovered. When the pH of the solution is greater than 7 the membrane is able to slide over the expanding and contracting substrate. This membrane sliding motion occurs in the plane of the support and is dynamic. The effectiveness at which membrane tension is relaxed is dependent on the rate at which the substrate area is changed.

When the pH is reduced below pH 7, the membrane area becomes strongly coupled to that of the support and the membrane dramatically ruptures, opening large circular pores, in response to substrate deformation. The pores exhibit a dynamic area change, revealing a complex flow of membrane across the support to

equilibrate stress.

This novel supported membrane behaviour reveals the rich physics possessed by supported lipid systems, that may assist in the design of new supported lipid based technologies.

Dedication

This thesis is for my Mum and Dad. For their indefatigable patience, love and support that has not only got me through this, but given me the opportunity to embark on this journey in the first place.

Declaration

The work presented in this thesis has developed under the supervision of Dr. Margarita Staykova in the Physics Department of Durham University. Unless otherwise stated, the results, analysis, figures and text are all my own. No part of this thesis has been presented for any other degree or qualification.

Publication

L. Stubbington, M. Arroyo, M. Staykova. "Sticking and sliding of lipid bilayers on deformable substrates". *Soft Matter*, **13**, 181 (2017).

Acknowledgements

My utmost thanks goes to Dr. Margarita Staykova without whom I would never have been presented this opportunity to work and study in such a beautiful part of the UK. I thank-you for the faith you have placed in me. I am confident of the continued success and development of the Staykova Biophysical research group as part of Durham Soft Matter.

I thank the residents of room PH142 both past and present for making the office such a nice place to sit. A special mention must go to Prof. Del Atkinson and Dr. Beth Bromley for all the pastoral support and advice they have offered throughout.

I could not have got through the some of the more trying experimental moments without encouragement from Ethan Miller and William Trewby. A special thanks is also extended to Alessandro Zunino, who taught how to do an experiment, properly.

Durham is a wonderful place, but it has been made all the more exceptional by the great group of colleagues I have associated with over the years. I thank all the members, of the Durham postgraduate Friday night pub WhatsApp® group for regular trips to the pub and the company in the Bransden room. I would also like to thank Robert Williams, George Wells, Ben Robertson and Rahul Chacko for dealing with me as a house mate.

A fond farewell goes to Durham University Hill Walking Society for countless adventures in some spectacular parts of the world.

And lastly, I thank Rebecca Fong. Thank-you for cajoling me up various fells, for putting my cooking skills to the test and for countless lasting happy memories.

List of Symbols

F	System Free Energy
E	System Energy
T	Thermodynamic temperature
S	System Entropy
H	System Enthalpy
k_B	Boltzmann's constant
ν_{hc}	Hydrocarbon chain volume
l_{hc}	Hydrocarbon chain length
a_0	Equilibrium area per lipid head group
σ	Membrane elastic tension
κ_A	Membrane area elasticity modulus
κ_B	Membrane bending modulus
κ_G	Gaussian bending modulus
η	Viscosity
$v_{||}$	Shear velocity
$F_{||}$	Shear Force
λ	Line tension of a membrane edge
λ_D	Debye screening length
A	Membrane area
ϵ	Areal strain
τ	Viscoelastic characteristic time

b_s	Interfacial friction parameter
$V_{bil-sub}$	Bilayer-substrate interaction potential per unit area
W_{ad}	Interfacial contact potential
K	Reaction constant
M, L, T	mass, length, time *(Dimensional analysis variables)*

List of Abbreviations

AFM Atomic Force Microscopy.

Bis-TRIS Bis(2-hydroxyethyl)amino-tris(hydroxymethyl)methane.

BODIPY™ 558/568 C12 4,4-Difluoro-5-(2-Thienyl)-4-Bora-3a,4a-Diaza-s-Indacene-3-Dodecanoic Acid.

CCD Charge Coupled Device.

CMOS Complementary Metal-oxide Semiconductor.

cSLB Continuous Supported Lipid Bilayer.

DI Deionised Water.

DIC Differential Interference Contrast.

DiIC$_{16}$(3) 1,1'-Dihexadecyl-3,3,3',3'-Tetramethylindocarbocyanine Perchlorate.

DOPC 1,2-dioleoyl-sn-glycero-3-phosphocholine.

DOPE 1,2-dioleoyl-sn-glycero-3-phosphoethanolamine.

DOPS 1,2-dioleoyl-sn-glycero-3-phospho-L-serine.

DOTAP 1,2-dioleoyl-3-trimethylammonium-propane.

EDL Electric Double Layer.

FI Fluorescence Intensity.

FRAP Fluorescence Recovery After Photobleaching.

GUV Giant Unilamellar Vesicle.

HEPES 4-(2-hydroxyethyl)-1-piperazineethanesulfonic acid.

HH Henderson-Hasselbach.

IPA Isopropanol.

ITO Indium Tin Oxide.

MD Molecular Dynamics.

MES 2-(N-morpholino)ethanesulfonic acid.

NBD-X 6-(N-(7-Nitrobenz-2-Oxa-1,3-Diazol-4-yl)amino)Hexanoic Acid.

PC Phosphocholine.

PDMS Poly(dimethyl)siloxane.

PFS Perfect Focus System.

PSF Point spread function.

Rh-DPPE 1,2-dipalmitoyl-sn-glycero-3-phosphoethanolamine-N-(lissamine rhodamine
B sulfonyl) (ammonium salt).

SLB Supported Lipid Bilayer.

SLP Supported Lipid Patch.

SOPC 1-stearoyl-2-oleoyl-phosphatidyl-choline.

SUV Small Unilamellar Vesicle.

SVL Supported Vesicle Layer.

TEM Transmission Electron Microscopy.

TIRF Total Internal Reflection Microscopy.

TRIS Tris(hydroxymethyl)aminomethane.

UV Ultraviolet.

VdW Van der Waals.

Contents

xxiv

Chapter 1

Introduction & Aims

Membranes and Membrane Deformation in Biology

Cells are very good at doing physics and much of this aptitude comes from the unique properties of the membrane that provides the essential compartmentalisation, necessary for life. Cells experience external forces from a range of different sources; hydrodynamic flows [1] in arteries for instance, or at cell-cell and cell-substrate adhesion points [2]. Recently it has become apparent that physical forces are drivers of cell physiology and behaviour. The membrane functions as an essential and powerful server collating and disseminating the information obtained from all the differing types of mechanical stresses. Indeed disease can be a result of the incorrect interpretation of mechanical cues, through the membrane [3, 4]. The cell interface is then a very delicate piece of apparatus. At the same time, the number of cellular life processes that require spectacular deformations of the membrane are innumerable. From the dramatic compression of red blood cells during microcirculation [5], to the brutal polarisation of cell growth and division [6], the distortions that a cell can withstand whilst remaining functional are unparalleled in engineering. On top of all of this the materials required to repair and produce a membrane must not be metabolically taxing to produce and recycle.

It is truly remarkable that nature has developed a system that can meet the design specifications of the membrane. Close inspection reveals a soft, self-assembled, membrane, coupled to a network of dense polymeric filaments. The plasma membrane encapsulates and orchestrates these support filaments whilst also providing the backdrop for a plethora of functional protein molecules [7]. Additionally, be-

cause membranes are so thin, $3-5$ nm, they are extremely soft, with a resistance to bending that has energetic contributions of the order of 20 k_BT [8]. This bendiness allows the cell to store excess membrane in curved structures that form at the junction of cell-cell, or cell-substrate adhesion zones. These include for example, membrane folds, wrinkles, caveolae, vacuole like dilations and blebs [9]. At the same time, the membrane fiercely resists stretching modes of deformation with an area elasticity modulus $\kappa_A \approx 0.24$ Jm^{-2} [10]. For a 1 μm^2 areal dilation this corresponds to an energy expenditure of nearly 60×10^6 k_BT. This steep energetic landscape provides an ideal signalling platform.

In addition the tension in the cellular envelope has recently been identified as a key regulator of many cellular life processes [9], such as membrane turnover and cell spreading. Clearly there exists a complex interplay between the tension in the membrane and the shapes used to store membrane area, as these can be deconstructed in response to rapid changes to cell shape and size. Nanoscale invaginations in the membrane, known as caveolae, have shown a dependence on membrane tension [11]; on completely separate time scales to cell metabolism. Phagocytosis, a complex remodelling procedure involving cytoskeletal reorganisation and biochemical signalling, is also orchestrated by membrane tension [12]. Even minimal cell systems, completely devoid of metabolism and proteins have been shown to reconstitute tension regulated endo/exocytosis [9]. Thus, a large number of the tension buffering processes are instead due to the astonishing physical properties of the lipid membrane, which provides sufficient justification for the study of this remarkable material alone.

Biophysical Model Systems

The intricacy of the cell and the complex feedback loops that connect its components together make studying individual components nigh on impossible. The deposition of phospholipid membranes on solid supports provides a convenient method to study the intrinsic properties of the membrane without the complexity of the whole cell [13]. The presence of the support provides mechanical rigidity whilst the thin layer of hydration water confined between the support and the bilayer is assumed to decouple the support from the lipid [14]. Once more, coupling lipid films to solid surfaces makes the system accessible to an ever growing list of informative surface

sensitive techniques such as Atomic Force Microscopy (AFM) and Total Internal Reflection Microscopy (TIRF) microscopy [15]. Studying the interaction of membranes with supports can even help identify new methods of targeted drug delivery [16].

Typical support choices are rigid and inert materials such as quartz or mica. However, this type of membrane support system is by no means a faithful replica of membrane supports in biology. For one, these supports bind the membrane in a deep adhesive potential well dominated by strong Van der Waals (VdW) interactions [17]. A more faithful mimic for the bilayer-substrate adhesion found in nature is to use a polymeric support. Polymer substrates have indeed recently emerged as attractive tools for supporting lipid membranes in the design of new classes of biosensor and filtration devices [18, 19]. This is because polymer surfaces provide a thicker hydration layer for the reconstitution of proteins, glycolipids and recognition sites, as well as being biocompatible for use in medicine and food technologies. Polymers themselves display a diverse set of tuneable physical and chemical properties and as a consequence the adhesion between a bilayer and polymer can be controlled by changing the polymer surface chemistry [20, 21]. Polymeric materials can additionally be made soft and malleable allowing researchers to explore the effects of substrate stiffness on membrane properties [22] and/or the effects of substrate deformations. As previously mentioned, the support for the membrane found in the cell is a complex network of polymeric filaments that are continually remodelling in response to mechanical and chemical cues. It is therefore possible to extend models of the cellular interface by supporting membranes on supports that are elastic.

PDMS is a biocompatible, deformable and optically transparent polymer [23] and the material lends itself well to microfluidics [24, 20] due to the ease with which the material may be chemically bonded to other silica based materials such as glass. PDMS surfaces therefore represent an ideal substrate choice when developing a system to understand the dynamic nature of membrane support couplings.

This thesis will study the passive means of area regulation available to a simple, single component, lipid membrane supported on an elastic PDMS support. From this, new insights into the importance of the coupling between the membrane and its supporting surface in biology will be gained. The experiments can also develop new guiding principles for the design of future supported lipid based devices.

Aims of this Thesis

This thesis will report on the successful development of a PDMS substrate for lipid bilayers with a controllable area. The system allows for the methodical study of the passive means of area regulation available to a simple membrane. The use of a simple, single component membrane will help elucidate the importance of the lipids alone as a key constituent of the cell.

The aims are to firstly understand and test methodically this system of a reduced complexity membrane coupled to an elastic support. Secondly, by understanding better the bilayer-support system, insights can be gained to assist in the fast developing world of supported lipid bilayer based devices for research and technology. Finally, we seek to replicate some of the passive means of membrane area regulation utilised by cells during life processes.

As the discussion develops, a set of complex membrane responses, to substrate deformation will emerge. The transition between these mechanisms is controlled by the support properties and the conditions of the aqueous environment that surrounds the bilayer; both of which are easily manipulated experimental parameters.

Thesis Overview

The remaining chapters are organised as follows:

Chapter 2 will provide a survey of the accepted theoretical framework for the deformation of lipid membranes. This will summarise the basic physics of membrane deformation as well as what is known about membrane systems that are coupled to substrates, including the interaction potential and the methods of dissipation available when a bilayer and a support surface undergo relative motion.

Chapter 3 focuses on the materials, equipment and protocols used to perform the experiments. Here I will introduce the device and describe its performance metrics as well as the effect of plasma treatment on the surface properties of the device. This chapter will also introduce the image analysis techniques that have proven useful during my time of study. The protocols adopted to ensure that image quantification is transparent and repeatable will be explained; the macros and scripts that facilitate efficient analysis will be provided in an appendix.

Chapter 4 will collate observations regarding bilayer formation via the spontaneous fusion of vesicles on PDMS substrates. Despite the ubiquity of this technique in research the procedure can, in many respects, appear more like an art than a science.

Chapter 5 describes the membrane behaviour on partially hydrophilic supports. The membrane can relax substrate stress by deforming out of the plane. The absorption and projection of lipid will be analysed and discussed. The complex interplay between the substrate properties and the response of the membrane will begin to emerge as a key theme permeating this thesis.

Chapter 6 is dedicated to membranes sliding over hydrophilic supports. Membranes are able to slide and slip over the deforming device if the substrate is fully hydrophilic and the pH is high. The membrane-substrate coupling becomes dynamic, rate dependent and the absorption and protrusion of lipid material is inhibited.

Chapter 7 describes an alternative stress relaxation pathway that exists on the hydrophilic support. Supported membranes can be made to open large, circular pores in response to deformation. Following the dynamics of pore formation can provide insight into the convective flow of lipid throughout a membrane that is induced by substrate stress.

Chapter 8 is describes the difference between the two classes of membrane response on the hydrophilic support and to the experimental evidence of a transition between the sliding regime, the subject of Chapter 7, and the pore formation regime, Chapter 8. The transition will be shown to be reversible and easily controlled in the laboratory environment. The results have implications for the design and development of new classes of bio-sensor, and mechanically responsive materials.

Chapter 9 will describe experimental efforts towards controlling the membrane deposition process by creating a substrate with surface properties that vary with position.

Chapter 10 will conclude this thesis by reiterating the important points. In addition, as with any scientific work, there are questions that remain unanswered.

Here I will list what I believe to be the most important questions that require answering in order to fully appreciate the complexity of the membrane-elastic support system.

Chapter 2

Theory

2.1   Lipids and Amphiphilic Self Assembly
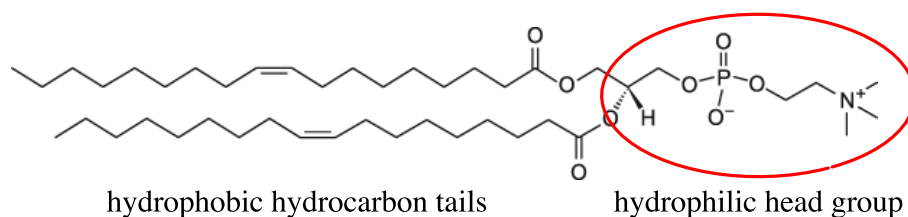
Figure 2.1: Structure of one of the most abundant lipids in nature, 1,2-dioleoyl-sn-glycero-3-phosphocholine (DOPC), which constitutes approximately 17 % by weight of erthrocyte plasma membrane [25].

Phospholipids are a particular type of surfactant found ubiquitously in nature. The molecule is amphiphilic and this means that it has both a water-avoiding hydrophobic domain and a water-loving hydrophilic domain, as illustrated in figure 2.1. Because of this, lipids in aqueous solution force local water molecules to adopt an ordered structure, which carries a substantial entropic penalty. As a consequence, above a critical concentration lipid molecules will aggregate in order to sequester their hydrophobic domain from the surrounding solution. The concentration at which this occurs is known as the critical aggregation concentration and can be derived by considering the change in free energy per molecule when removing a lipid from an aggregate to dispersion. The distinction between an aggregate and dispersed state is illustrated schematically in figure 2.2. The free energy change can be approximated by equation 2.1, where E_{bind} is the work necessary to remove a lipid from

the aggregate and S_{gas} is the entropy of an ideal gas. S_{gas} is given in equation 2.2 and is dependent on the number density, ρ, and the thermal de-Broglie wavelength, λ, which is roughly equal to the average de Broglie wavelength of an ensemble of ideal gas particles at a given temperature [10]. λ has a value of approximately 4 pm for a DOPC lipid at room temperature.
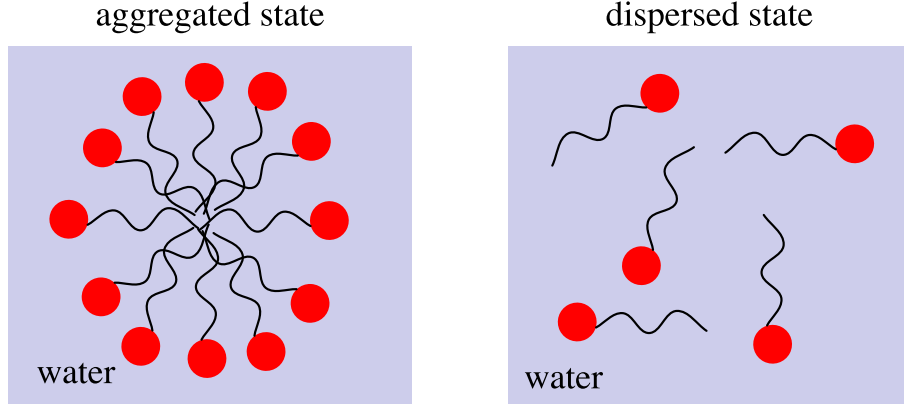
Figure 2.2: A simple two state picture of amphiphilic aggregation, adapted from the book by Boal [10].

$$F_{sol} \sim E_{bind} - TS_{gas} \tag{2.1}$$

$$S_{gas} = k_B \left[\frac{5}{2} - ln \left(\rho \lambda^3 \right) \right] \tag{2.2}$$

In writing equation 2.1 it is assumed that the reduction in entropy of the solution around any exposed hydrocarbon tails is negligible and that the concentration of lipid is sufficiently low such that the entropy of the dispersed state may be considered an ideal gas. Equation 2.1 also sets the total interaction energy and entropy of the aggregate to zero. Because of this definition, the crossover point at which the aggregate state becomes favourable is defined as $F_{sol} = 0$, with the dispersed state being favoured at low concentrations. Setting equation 2.1 to zero yields equation 2.3, an estimate for the critical aggregation concentration ρ_{cat}.

$$\rho_{cat} = \frac{1}{\lambda^3} \exp \left(\frac{5}{2} - \frac{E_{bind}}{k_B T} \right) \tag{2.3}$$

The structure of the aggregate formed depends on many factors, including the chemical and physical properties of the lipid, electrolyte concentration, temperature,

pH and perhaps, most beautifully, the aspect ratio of the individual lipids. The physics of this is captured in the shape factor, $\frac{v_{hc}}{a_0 l_{hc}}$, where a_0, l_{hc} and v_{hc} are the lipid headgroup area, the length and volume of the lipid hydrocarbon chains respectively. This dimensionless parameter describes how lipids can best pack into the aggregate, and in particular for $\frac{1}{2} \geq \frac{v_{hc}}{a_0 l_{hc}} \leq 1$ shape values, the preferred aggregate is a planar bilayer. Lipids for which the shape factor lies outside of this range favour curved structures due to the intrinsic mismatch between head group area and hydrocarbon cross-section.

2.2 The Free-Energy of a Supported Lipid Membrane

The deformation of supported lipid bilayers will be the subject of this thesis. For this reason it is sensible to consider the energetic contributions to the free energy of a supported lipid membrane. All the terms relevant to a continuum description of the total free energy of a membrane of area A are contained in the following equation.

$$E = \frac{1}{2} \int dA \left[\frac{\kappa_A (a - a_0)^2}{a_0} + \kappa_B \left(\frac{1}{R_1} + \kappa_G \left(\frac{1}{R_1} R_2 \right) + \frac{1}{R_2} \right)^2 + 2V_{bil-sub} \right] \quad (2.4)$$

The 3 terms in equation 2.4 are from left to right the energetic contributions due to stretching, bending and the interaction with the underlying support. In the second term, the assumption has been made that the membrane has zero spontaneous curvature due to a symmetrical distribution of lipid between the two leaflets. The second term also includes the Gaussian curvature modulus, which may be omitted from theoretical descriptions of membranes that go through shape changes that do not require a change in topography. As it will be demonstrated in later experimental chapters, the substrate-coupled membrane can form membrane pores, which represents a change in topography. The following sections will describe the origins of each of the terms in more detail.

2.2.1   Elastic Stretching Energy

Individual lipids are able to diffuse within the bilayer plane [26]. A consequence of this mobility is that membranes are fluid and cannot sustain shear stress. The ability of individual membrane components to flow complicates a theoretical description of the response of a membrane to external stress. The simplest description accounts for the surface tension at the hydrophobic interface and the equilibrium structure of the bilayer aggregate. Within the bilayer itself, the optimal area per lipid represents a trade off between the forces of steric and electrostatic repulsion between the lipid head-groups, and the cohesive forces that seek to minimise the area of interface between the hydrocarbon domain and the aqueous solvent. For the bilayer configuration this results in an area per lipid head a_0 and an energy density E that are quadratic in departure from this value, as in equation 2.5, where α is a parameter describing how the repulsive interactions between lipids scale with areal density.

$$E = \gamma a + \frac{\alpha}{a} = 2\gamma a_0 + \frac{\gamma \left(a - a_0\right)^2}{a_0^2} \tag{2.5}$$

Comparing the form of equation 2.5 to the definition of a two dimensional compressibility modulus $E = \frac{K_A}{2} \frac{(a-a_0)^2}{a_0^2}$ yields an area compressibility of $K_A = 4\gamma$, where an additional factor of 2 has been applied to account for the two lipid leaflets that form a bilayer [10, 27]. Based on the analysis of phase transitions of liquid crystals Parsegian obtained values of $0.02 - 0.05 \ \mathrm{Jm}^{-2}$ [28]. This yields an area compression modulus of the order $0.08 - 0.2 \ \mathrm{Jm}^{-2}$. Taking a typical area of membrane of approximately $1 \ \mu\mathrm{m}^2$ then this yields an energy of $20 - 50 \times 10^6 \ \mathrm{k_B T}$. In other words, membranes are extremely difficult to stretch.

2.2.2   Bending Energy

Bilayers are extremely thin with a cross-sectional height of the order of $3 - 5$ nm. Because of this very large aspect ratio bending the membrane also causes a deviation from the equilibrium area per lipid $a \neq a_0$. When the membrane is forced to adopt a curvature, the outer leaflet achieves an areal density $a > a_0$, whilst the inner leaflet is compressed. This alters the energetics of the bilayer. An intuitive grasp

of curvature energy can be obtained by examining the bending energy functional first proposed by Helfrich in 1973 [29], equation 2.6. The equation quantifies the work necessary to deform a membrane of total area A to a geometry with a mean curvature $\frac{R_1+R_2}{2R_1R_2}$. The energy is quadratic in geometrical parameters [30] and the constant of proportionality is known as the bending κ_B modulus. Integration over the area gives the total free energy, which for cylindrically shaped lipids that do not favour curved structures, is clearly minimised for a planar bilayer configuration. That is $\frac{1}{R_1} = \frac{1}{R_2} = 0$.

$$F = \frac{\kappa_B}{2} \int_A \left(\frac{1}{R_1} + \frac{1}{R_2} \right)^2 dA \tag{2.6}$$

Membranes under tension

Experimentally it is possible to measure both the membrane resistance to areal dilation κ_A and bending κ_B for both pure lipid bilayers and reconstituted cells. However, the measurement is made complicated by the soft nature of self-assembled aggregates. Low resistance to bending means that bilayers fluctuate in the thermal breeze. As a consequence, the initial application of tension only suppresses thermal fluctuations, without any change to the value of the area per lipid [10]. This decreases the observed strain for a given tension, making the membrane appear stiffer. Most literature estimates for the mechanical strength of pure lipid bilayers and reconstituted cell membranes originate from micropipette aspiration experiments [31, 32, 33, 34]. Alternative methods include analysis of the fluctuation spectrum of flaccid vesicles and Molecular Dynamics (MD) simulations [35].

Membrane elasticity is found to depend strongly on membrane phase state and lipid architecture. Rawicz *et al.* [36] used micropipette aspiration to determine both κ_A and κ_B for a catalogue of different lipids with the same Phosphocholine (PC) head-group. Area compressibility, κ_A was found to exhibit little variation with acyl chain length or degree of saturation with values within 10% of 0.24 Jm^2. However a progressive increase in bending modulus κ_B is observed for increasing length of the hydrocarbon chain from 13 to 18 carbon atoms. The inclusion of two or more double bonds results in a dramatic decrease in κ_B, reflecting the importance of acyl chain packing in determining the forces of cohesion in lipid bilayers.

Membrane Rupture

hydrophilic pore

hydrophobic pore
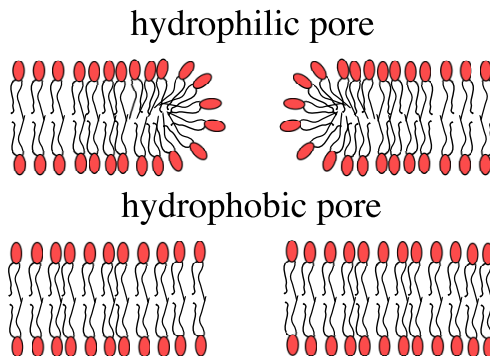
Figure 2.3: Different configurations available to membrane pores.

Discussing membranes under tension leads naturally to questions regarding the forces and shape transformations involved when a membrane ruptures. The membrane distortion required as a membrane forms a pore is illustrated schematically in figure 2.3. Membrane pores can in principle adopt two different configurations. A hydrophilic pore is lined with lipid head groups but has a substantial energetic penalty due to curvature. Alternatively, lipids may stack vertically at a membrane edge at the cost of hydrocarbon tail exposure to solvent, forming a hydrophobic pore. Based on the high experimental value of the water amphiphile surface tension a hydrophobic pore structure would be extremely unstable, even for lipids with a highly cylindrical shape factor. This observation is supported by MD simulations [37], although the hydrophobic pore could form an important precursor structure in the energy landscape of hydrophilic pore formation [38]. The failure of a fluid lipid membrane is a kinetic process [10, 39]. The question of membrane failure is not so much how much force or tension must be imposed in order to break the membrane but how long must one wait before the membrane fails once a given tension is applied. Because of thermal fluctuations, nanoscopic pores are opening in a free unstressed membrane continuously. The membrane remains stable because there is a large activation barrier that must be overcome before a pore can reach microscopically observable dimensions. The activation barrier stems from the membrane shape change during pore formation. This carries an energy penalty which, to a first approximation, may be assumed to vary linearly with the pore radius. At the same time, the formation of a membrane pore relaxes any tension accumulated in

the bilayer. As of consequence one may write down an enthalpy $H_{pore}(r)$ as in equation 2.7 where λ is a line tension associated with the pore circumference, σ is the tension in the membrane and r is the pore radius.

$$H_{pore}(r) = 2\pi\lambda r - \pi r^2 \sigma \qquad (2.7)$$

$H_{pore}(r)$ has a maximum at a tension dependent pore radius of $r_c = \frac{\lambda}{\sigma}$. The enthalpy evaluated at this radius gives the cavitation barrier $E_c = \frac{\pi\lambda^2}{\sigma}$. If the system can temporarily obtain enough energy from the surrounding heat bath to cross over this barrier then the pore radius will grow indefinitely [10]. However, the likelihood of such events follows a Boltzmann distribution $\approx \exp\left(\frac{-H_{pore}}{k_B T}\right)$ and so the vast majority of nucleated pores at finite temperature will reseal rapidly in the absence of applied stress.

This simple description is not sufficient to capture all the rich physics of pore formation in fluid bilayers. The ultimate tensile strain at which a membrane ruptures is often referred to as the critical strain or lysis tension. Membranes are actually found to possess a dynamic strength in a sense that rupture tension depends on the rate at which tension is increased [39, 40, 41]. Vesicles and free membranes achieve statistically higher lysis tensions when stressed rapidly. This may be rationalised on the basis that membrane failure becomes significantly more likely when the tension in the membrane rises above the level when the time needed for the system to borrow enough energy to surpass the cavitation barrier, falls within the lifetime of a precursor pore defect state. Theory and simulation thus predict that the rate-limiting step to pore formation becomes the formation of a rare precursor defect at swift ramp rates, since the tension at which the barrier to cavitation is close to zero is rapidly reached.

MD simulation provides a convenient means to study the molecular rearrangement that occurs as a pore forms [38]. Once a file defect of water molecules percolates the bilayer, the lipids rapidly rearrange to form a hydrophilic pore (figure 2.3). This process of rearrangement alters the energy landscape to pore formation and stabilises the pore.

2.2.3   Bilayer-substrate Interaction Potential

For the simplified case of DOPC lipid bilayers interacting with a chemically homogenous support the adhesion to the substrate is non-specific. The forces that comprise this interaction can be reduced to a few key players, namely, the VdW interaction, the Electric Double Layer (EDL), and entropic forces that arise due to the confined Brownian motion of membrane films. Unique to the case of membranes in very close proximity to surfaces are solvation or hydration forces, which originate from the pressure required to squeeze out the tenaciously bound water molecules that surround lipid head groups [42]. What follows is based on the discussions and equations provided in the excellent texts by Safran [43], Israelachvili [44] and Boal [10].

Van der Waals Forces

VdW forces are experienced by all surfaces regardless of the medium through which they interact. Permanent, instantaneous or induced dipoles can correlate and produce attractive forces between molecules that are often summarised as a potential that obeys equation 2.8, where C_{vdw} is a proportionality constant and r is the separation between molecules.

$$V_{mol}(r) = \frac{-C_{vdw}}{r^6} \tag{2.8}$$

For extended objects the total interaction energy can be calculated by assuming pair-wise addition of point like molecular interactions, which is implicitly assuming no correlation between molecules comprising the same surface. For two infinite surfaces of finite thickness t, at separation d, the energy per unit area $v(d)$ is given by equation 2.9. The quantity $-\pi^2 C_{vdw}\rho_1\rho_2$ is known as the Hamaker constant and is proportional to the product of the densities of the two surfaces ρ_1 and ρ_2. Its value is usually on the order of $25k_BT$. The VdW interaction ultimately wins out when any two surfaces are held sufficiently close together and is in part responsible for the adhesion and subsequent rupture of vesicles adhering to surfaces.

$$v(d) = \frac{-\pi C_{vdw}\rho_1\rho_2 t^2}{2d^4} \tag{2.9}$$

The Electric Double-Layer

Many surfaces become charged in an aqueous solution due to interactions with the strong molecular dipole of water [45]. These surfaces release charged ions into solution, equal in amount and opposite in sign to the charge accumulated at the surface; these ions are known as counterions. At non-zero temperature, these counterions can maximise their entropy by exploring all available configurations in the solution. At equilibrium an ion density distribution emerges which reflects the competition between system entropy and system energy. The result is a layer of tightly bound surface counterions, the so-called Stern layer, followed by a diffuse cloud of ions in solution. Together these two layers are referred to as the EDL. Bringing in two similarly charged surfaces together causes the EDLs to overlap, generating a repulsive pressure P which is described, for modest surface charges by equation 2.10; where d is the separation between the two surfaces.

$$P \propto \exp\left(\frac{d}{\lambda_D}\right) \tag{2.10}$$

The length of the exponential is characterised by the Debye screening length. λ_D is an important length scale, determined entirely by the properties of the solvent between the two surfaces. It sets the rate at which electric double layer forces drop off between charged surfaces in an electrolyte. Numerically the Debye length can be evaluated according to equation 2.11, where $c_{\infty,i}$ is the concentration of electrolyte ion species i in the bulk and q_i is the charge on the ion.

$$\lambda_D^{-2} = \Sigma_i \frac{c_{\infty,i} q_i^2}{\epsilon k_B T} \tag{2.11}$$

Entropic and fluctuation forces

Thermally agitated soft membranes resist confinement through the suppression of membrane fluctuations brought about by the proximity of a nearby surface or second membrane. A free unit area of membrane will oscillate about a root mean square displacement from its mean positional plane proportional to $\sqrt{\frac{k_B T}{4\pi^3 \kappa_B}}$. Due to the suppression of these undulations an external pressure must be maintained in order to keep a fluid bilayer in close proximity to a wall or second membrane. The VdW adhesion of a vesicle in weak adhesive contact with a surface is stabilised

by this fluctuation pressure [46, 47]. The case of weak vesicle adhesion is illustrated in figure 2.4; here the vesicle adheres to the substrate, and deforms due to the adhesion but remains intact. For such systems the mean bilayer substrate separation has been determined, using Differential Interference Contrast (DIC) microscopy, to be $30, 40$ nm [48, 49].

(a) Weak bilayer substrate adhesion.

(b) Strong bilayer substrate adhesion.
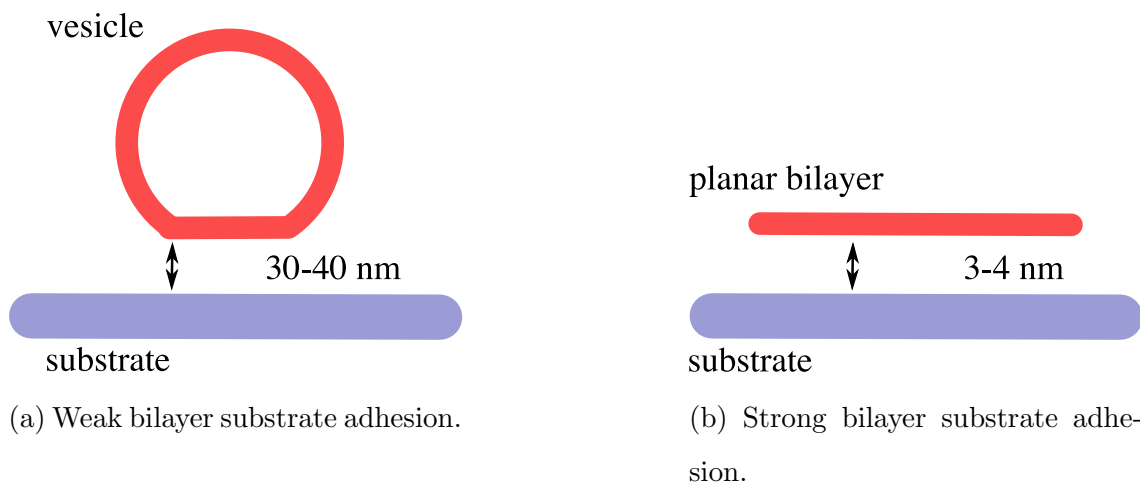
Figure 2.4: (a) Illustration of weak bilayer substrate adhesion, in which a sessile vesicle adheres to a surface and deforms but remains intact. (b) In contrast, for strong bilayer-substrate adhesion, the interaction is sufficient to rupture the vesicle and cause the membrane to spread into a planar configuration, parallel to the substrate. The approximate thickness of the water layer confined between the bilayer and substrate is annotated.

In the case of strong bilayer substrate adhesion (figure 2.4b) the membrane adopts a planar configuration. The stabilising entropic repulsion arises from the force required to squeeze out water molecules that are tenaciously bound to lipid headgroups and/or the charged surface. In this situation the confined solvent layer between the membrane and the substrate has a thickness that lies between $1 - 4$ nm [50], an order of magnitude less than the weak substrate adhesion case. Solvation or hydration forces can superimpose an oscillatory force behaviour on force versus displacement curves as individual water molecules are squashed out [51, 52] from between the approaching surfaces. Although the exact origin of hydration forces is controversial [53], the dominant behaviour is exponential with a potential energy similar to the form of equation 2.12 [42, 48], where, d is the distance between
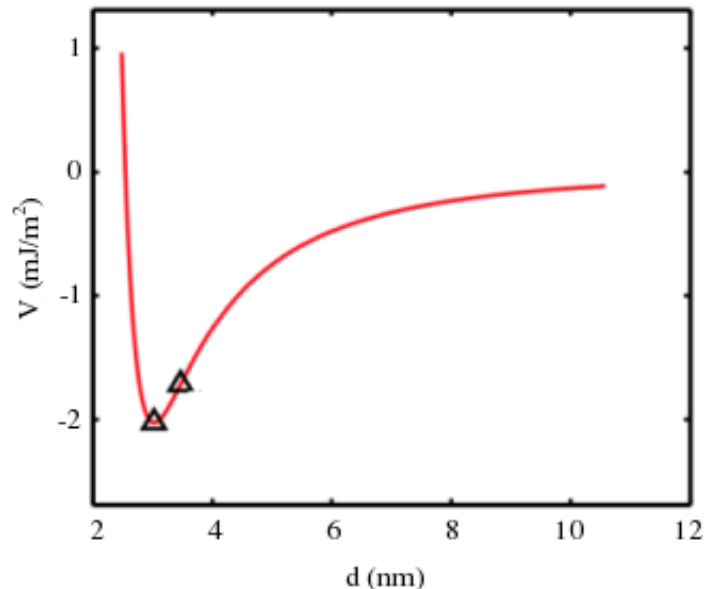
Figure 2.5: Bilayer-substrate interaction energy per unit area V versus separation d. Reproduced and modified with permission from Staykova *et al* [54].

the membrane and the substrate and $\frac{1}{\alpha} \approx 0.2 - 0.3$ nm. The oscillatory nature of the hydration force may be smeared out due to membrane undulations, but its contribution is not negligible.

$$V_{hyd} \propto exp\left(-\alpha d\right) \tag{2.12}$$

Generalised Interaction Potential

Combining all three contributions into the interaction potential $V_{bil-sub}$ is complicated. The parameter space is large and it is difficult to get an experimental foothold on substrate specific effects. However, the potential must have a minimum with respect to distance as this represents the adhered state of the membrane. This minimum is sketched in figure 2.5, for the case of strong bilayer-substrate adhesion. Contributions from entropic repulsion must win out at small separations, with adhesive interactions diminishing at infinity. For most applications, when the substrate topography need not be considered, this energetic contribution can be considered as a single contact potential value, W_{ad} [46].

2.3   Elastic, Viscous and Viscoelastic Dissipation

The concept of viscoelasticity will prove useful in later discussions of the rheology of the hydration film that separates the membrane from the substrate. Solids can be defined as materials that exhibit a constant strain, ϵ that is proportional to the applied stress. In contrast, liquids are unable to withstand forces applied tangentially and flow in response to a shear stress; in particular Newtonian liquids exhibit a strain rate that is proportional to the applied stress. This definition provides two idealisations of material properties; most soft materials exhibit behaviour under shear that is a combination of the solid and liquid behaviours. If the stress is applied quickly, on a time scale much less than the characteristic relaxation time, τ, of the material then the response is elastic; and the strain is fixed in time. On the other hand, if the stress is applied much slower than τ then the material yields and flows in response to shear stress [55].

2.3.1   Sliding and Friction

Together with the classifications of different material responses to shear, it is also important to lay the groundwork for situations in which the membrane and support can decouple and move relative to each another. One must consider the modes of viscous dissipation that can occur when the adhesion mediated friction between the support and the bilayer is overcome. Friction forces in physics are unique in the sense that there is no macroscopic force law describing how friction should behave. Friction arises as a result of motion of one body adjacent to another and it is not always clear how to relate the opposition to motion to the microscopic properties of the systems. There are few unifying principles with regard to friction forces. However, all friction forces are dissipative and involve the transfer of directed energy into random energy or heat. Because of this, friction forces are often observed to depend on the rate at which force is applied and display funicity, which is a behaviour that is dependent on experiment history.

Consider two surfaces in contact, forced into relative motion. A force parallel but opposite in direction to the external force will naturally arise if the two surfaces are rough. Molecular scale roughness forces the interface between the two surfaces

to broaden such that the asperities may slide past one another. This displacement in the normal direction is known as dilation and is detectable in any system where a *top* surface must slide over a *bottom* surface [44]. Because of this motion in the normal direction, work must be done against the external agent holding the surfaces in contact and also against any adhesion that might exist between the two surfaces. These two contributions are contained in the equation for the friction force between two dry surfaces, $F_{||}$ as in equation 2.13. The balance between the two terms in equation 2.13 dictates whether or not the friction between the two surfaces is load $\mu F_{\perp}$ or adhesion $W_{ad}A$ dominated.

$$F_{||} = \mu F_{\perp} + W_{ad}A \tag{2.13}$$

For the case of a bilayer on top of a support, the friction has to be adhesion dominated, as there is no external pressure.

A distinction is often made between the static force of friction that opposes the initiation of relative motion compared to the friction that brings the surfaces to rest when the drive is removed, kinetic friction. This is because kinetic friction is often smaller in magnitude than static friction.

2.3.2   Lubricated Sliding & Boundary Lubrication

The case of dry sliding is actually a rare one. Most surfaces are prevented from coming into molecular contact by a thin lubricating film. When two systems are prevented from coming into contact by the presence of an adsorbed layer of macromolecules, such as charged polymeric brushes or lipid bilayers, then the system is said to be boundary lubricated. The lubricating film can reduce or enhance the observed friction. The simplest case to consider is that of Couette flow where the friction force can be described mathematically by equation 2.14, where d is the film thickness. The case described by equation 2.14 is identical to the Newtonian liquid already described in section 2.3, where the intervening lubricating film exhibits a constant viscosity.

$$\frac{F_{||}}{A} = \frac{\eta v_{||}}{d} \tag{2.14}$$

2.3.3   Friction in the Supported Lipid Bilayer system

The problem of the friction experienced by bilayers moving over hydrophilic surfaces can be addressed from another angle. The process of bilayer formation *via* vesicle fusion has three important steps. First the vesicles approach the substrate due to colloidal interactions, and the vesicles then fuse and rupture which requires that the membrane spreads over the support. Not a great deal is known about this spreading but the most informative class of experiments in this regard come from the wetting of rehydrated lipid films over surfaces [49, 56]. In these experiments a dried lipid crystal is deposited on a substrate. The entire system is then submerged into water and the spreading kinetics of the bilayer are analysed *via* fluorescence microscopy. The driving mechanism for bilayer propagation is the bilayer-substrate interaction, W_{ad} [44]. Free energy is gained when a unit area of bilayer adsorbs onto the surface. If no tension is developed in the membrane all of this energy is converted to heat by the viscous dissipation processes that occurs during the spreading.

(a) Hydrodynamic shear of the interstitial water layer.

(b) Inter-leaflet shear, bilayer rolling.
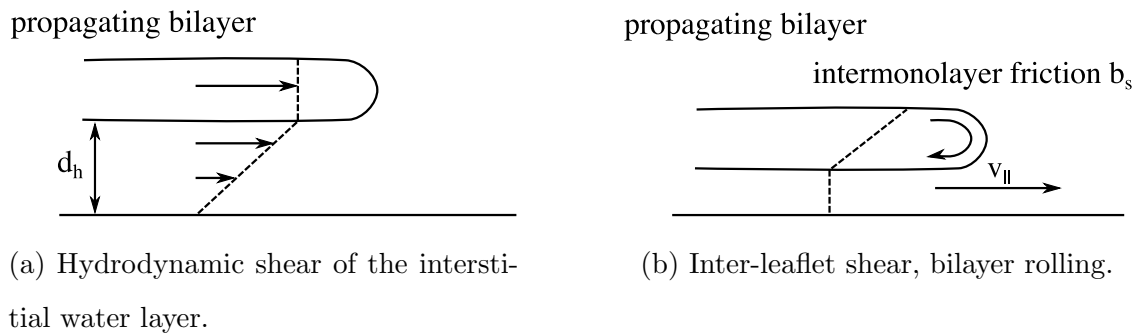
Figure 2.6: Schematic illustration of modes of viscous dissipation when a membrane slides over a surface.

The methods of dissipation when the surface is hydrophilic depend on the position of the slip plane and are illustrated in figure 2.6. In the first case the interstitial water layer is sheared and there is no relative flow of the bilayer leaflets (figure 2.6a). In the second case the resistance to shear is determined entirely by the viscosity associated with shearing the two leaflets of the bilayer (figure 2.6b). These two mechanisms are not independent and may occur in parallel [49, 56]. In the case of hydrodynamic shear of the interstitial water layer the shear force per unit area is given by equation 2.15. This is written on the assumption of simple linear rheology of the confined water film; with d_h the thickness of the hydration

layer. In comparison, for bilayer rolling (figure 2.6b) the friction force F, is given by equation 2.16, where b_l is the membrane leaflet viscosity.

$$\frac{F_{||}}{A} = \frac{\eta v_{||}}{d_h} \tag{2.15}$$

$$\frac{F_{||}}{A} = 2b_l v_{||} \tag{2.16}$$

Comparison of equations 2.15 and 2.16, suggests that the dominant mode of dissipation is due to shear of the water layer for any physically meaningful water layer thickness; $d_h > d^* = \frac{\eta}{2b_l} \approx 0.03\ nm$, which is about the diameter of a single water molecule. However, the actual method of dissipation might include a combination of both modes since the use of the bulk viscosity of water may be unwarranted under these conditions.

Chapter 3

Materials & Methods

3.1 Materials

DOPC lipids and fluorescently labelled 1,2-dipalmitoyl-sn-glycero-3-phosphoethanolamine-N-(lissamine rhodamine B sulfonyl) (ammonium salt) (Rh-DPPE) were purchased in powder form from Avanti Polar Lipids Inc (Alabaster AL) and used without further purification. Fluorophores 4,4-Difluoro-5-(2-Thienyl)-4-Bora-3a,4a-Diaza-s-Indacene-3-Dodecanoic Acid (BODIPY$^{\text{TM}}$ 558/568 C12), 1,1'-Dihexadecyl-3,3,3',3'-Tetramethylindocarbocyanine Perchlorate (DiIC$_{16}$(3)) and 6-(N-(7-Nitrobenz-2-Oxa-1,3-Diazol-4-yl)amino)Hexanoic Acid (NBD-X) were purchased from Invitrogen® (ThermoFisher). Sugars, salts and buffering reagents including 4-(2-hydroxyethyl)-1-piperazineethanesulfonic acid (HEPES), Bis(2-hydroxyethyl)amino-tris(hydroxymethyl)methane (Bis-TRIS), Tris(hydroxymethyl)aminomethane (TRIS) and 2-(N-morpholino)ethanesulfonic acid (MES) were purchased from Sigma-Aldrich and used without further refinement. Deionised Water (DI) was obtained from a Merck Direct-Q® 3UV-R dispensing unit. PDMS elastomer and curing agent was purchased from Dow Corning.

Prior to use all laboratory glassware items were sonicated for 10 minutes first in Decon-90 solution before being rinsed first in DI, then Isopropanol (IPA) and then finally DI twice before drying.

3.2 Methods of Vesicle Preparation

3.2.1 Supported Lipid Patches

Giant Unilamellar Vesicle (GUV)s are prepared using an adapted version of the electroformation technique pioneered in reference [57]. Lipid stocks are dissolved in chloroform, mixed in appropriate molar proportions and diluted to a total lipid concentration of 2.5 mgmL^{-1}. Approximately 8 μL of lipid solution is spread onto the conductive side of cleaned Indium Tin Oxide (ITO) coated glass and vacuum desiccated over night to remove all traces of organic solvent. An electro-formation cell is created by placing a 1.5 mm Teflon spacer between the two ITO plates and filled with 300 mM sucrose solution *via* a disposable syringe and a small hole in the Teflon spacer which is subsequently sealed with vacuum grease. The sucrose has two purposes; firstly the sucrose solution provides additional contrast for microscopy and secondly, the sucrose osmotically balances the internal and external contents of the GUVs when transferred to buffer solutions.

The chamber is held together by bull clips and connected to a sinusoidal voltage of amplitude 1.5 V$_{\mathrm{pp}}$ and frequency 10 Hz overnight. Hydrodynamic flows induced in the electrofomation cell as a result of the sinusoidal field promote the detachment of closed spherical vesicles from the ITO surface. The vesicle solution contains a poly-disperse mixture of GUVs ranging from $10 - 100$ μm in diameter. Centrifugation of the GUV solution after removal from the ITO chamber can be used to separate aggregates and other impurities from the sample[1]. To prepare supported lipid patches, a small volume of GUV solution is diluted into a buffer of ionic strength 150 mM and the substrate surface is left to incubate in this GUV plus buffer suspension for approximately 10 minutes. During this time, vesicles come into contact with the substrate, rupture and spread [58], providing the surface is sufficiently hydrophilic and/or the buffer conditions are chosen appropriately. After patch formation the

---

[1]The sucrose solution typically purchased has a purity grade of 99.5 %. At a concentration of 300 mM this translates to an undefined impurity concentration of 1.5 mM. The electroformation chamber has a volume of $20 \times 15 \times 2$ mm^3, and this typically contains around 5×10^{-8} mol of lipid which is equivalent to a concentration of lipid equal to 85 μM. Thus, the concentration of unknown impurities in the *store bought* supply is likely to exceed the number of molecules of interest in each sample.

chamber is washed with fresh buffer to remove excess vesicles from the suspension and reduce the background fluorescence for subsequent imaging.

3.2.2   Continuous Supported Lipid Bilayers

To prepare continuous lipid films a volume of lipid mixture equivalent to 2 mg total lipid is transferred to a clean glass vial and the chloroform solvent is removed by drying with a flux of nitrogen. Residual chloroform is evaporated overnight. The dry lipid film is rehydrated in 2 mL of a buffer of ionic strength 150 mM to yield a final lipid concentration of 1 mgml^{-1}. The rehydration procedure produces a turbid solution of multilamellar vesicles. To create Small Unilamellar Vesicle (SUV)s with sizes narrowly distributed between $150 - 200$ nm a tip sonicator is inserted in the vial and the solution is sonicated for 2.5 minutes. At the end of this procedure the vial contains a homogeneous mixture of SUVs. If further refinement of the vesicle size distribution is required, in for instance ζ potential measurements, the solution may be passed through a 100 nm poly-carbonate extrusion filter. After extrusion the vesicle size distribution exhibits a narrow peak around 150 nm which can be verified using differential light scattering in a Malvern ®Zetasizer. The SUV solution is subsequently diluted to 0.1 mgml^{-1} using fresh buffer. This solution is used to wet the substrate of interest and left to incubate for 30 minutes during which time vesicles come into contact with the substrate, adhere and possibly rupture and spread to form a continuous lipid film, depending on substrate surface energy and buffer properties. The chamber is rinsed with fresh buffer or deionised water several times to remove residual suspended lipid and the sample is transferred immediately to the microscope for imaging. At this stage, the SLB is subjected to a Fluorescence Recovery After Photobleaching (FRAP) test to confirm, qualitatively, the continuous nature of the bilayer through the recovery of fluorescence intensity in the bleached region.

3.2.3   Fluorophores

Fluorescent lipids come in many different forms. Lipophilic fluorophores consist of lipid molecules with a covalently attached fluorophore. The position at which the fluorophore attaches to the lipid can either be at the hydrophilic head or the
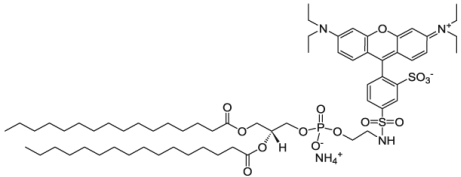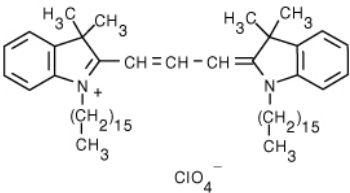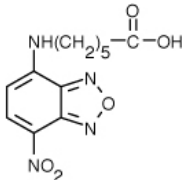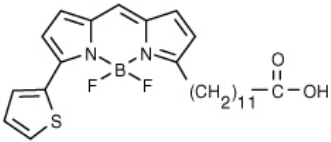
Chemical Structure	Full name (abbreviation)
	1,2-dipalmitoyl-sn-glycero-3-phosphoethanolamine-N-(lissamine rhodamine B sulfonyl) (ammonium salt) (Rh-DPPE)
	1,1'-Dihexadecyl-3,3,3',3'-Tetramethylindocarbocyanine Perchlorate (DiIC$_{16}$(3))
	6-(N-(7-Nitrobenz-2-Oxa-1,3-Diazol-4-yl)amino)Hexanoic Acid (NBD-X)
	4,4-difluoro-5,7-dimethyl-4-bora-3a,4a-diaza-s-indacene-3-dodecanoic acid (BODIPY$_{C12}$)

Table 3.1: Fluorophores used in experiments.

acyl chains, see section 2.1. Fatty acids and sterols can also be covalently modified and partition the bilayer in the hydrophobic core. It is generally assumed that the inclusion of a small molar fraction of fluorophore does not alter the physical or chemical properties of the bilayer substantially. However, in at least one study fluorophore concentration has been shown to alter the mechanical properties of lipid bilayers [59]. For this reason experiments are repeated with different classes of fluorophore to decrease the likelihood that results could be attributed to fluorophore specific artefacts. Fluorophores used are listed in table 3.1.

3.2.4   Buffer Preparation

Proton transfer in solution is extremely important in biology. Slight changes in the concentration of hydronium ions, or pH, can have profound effects from the denaturing of proteins to changes in cell signalling and metabolism [60]. In particular, a large number of membrane mechanical and chemical properties are functions of solution pH [61]. For this reason it is important to control pH in experiments. A buffered solution is one that contains molecules that can supply protons to the aqueous environment in a controlled way.

Buffer Equations

The pH scale, a logarithmic scale of hydronium ion concentration, is defined by equation 3.1a. Pure water, being polar by nature, can dissociate on its own. The product of the concentration of ionic species from this dissociation is known as the ionic product of water and it given by equation 3.1b. At pH 7, the sum of hydroxide and hydronium ions is minimised, or the water is as electrically neutral as can be [62].

$$pH = -\log[H^+] \tag{3.1a}$$

$$K_{H_2O} = [H^+][OH^-] \simeq 1 * 10^{-14} M \tag{3.1b}$$

Weak acids and bases are defined as those that do not dissociate fully in water. Instead these molecules come to an ionisation equilibrium where the rate at which the acid loses protons is exactly compensated by the rate at which protons are reabsorbed by the base, equation 3.2a.

$$\text{HA} \rightleftharpoons \text{H}_3{}^+ + \text{A}^- \tag{3.2a}$$

$$K_a = \frac{[H_3O^+][A^-]}{[HA]} \tag{3.2b}$$

$$pH = pK_a + \log\frac{[A^-]}{[HA]} \tag{3.2c}$$

This dissociation of buffer molecules can be described mathematically using the law of mass action 3.2b. This states that for a simple acid at equilibrium the ratio of dissociated species to protonated acid is constant for a given temperature. Taking the logarithm of equation 3.2b yields the Henderson-Hasselbach equation 3.2c; where $[A^-]$ represents the concentration of conjugate base species, K_a is the dissociation constant for the acid and $[HA]$ is the concentration of conjugate acid species. It is not strictly so that the base species carries a negative charge or that the acid is neutral, despite the notation. Rather it is only true that the base has lost a proton relative to the conjugate acid. If the pK_a of the chosen buffer is known then the pH of the solution is determined entirely by the ratio of acid to base of the buffer species. Thus the Henderson-Hasselbach equation 3.2c, can be used to design a solution that can maintain a given pH.

Controlling Ionic strength

pK_a is a function of temperature and the ionic strength of the solution. In general lab temperature is ambient and determined by the building conditioning systems, however ensuring that solutions have an equivalent ionic strength is easy to overlook.

The ionic strength of a solution, I is defined by equation 3.3; a sum of the number of each charged species present, weighted by the charge of that species. The ionic strength of mammalian cells is an approximately constant at 0.154 M [62]. Variable ionic strength has important consequences as electrostatic interactions and membranes have been shown both experimentally and theoretically to have dramatically different properties in the presence of varying salt concentration [63, 64, 65, 66].

$$I = \frac{1}{2} \sum_{i=1}^{n} (c_i z_i^2) \tag{3.3}$$

The matter of performing experiments at fixed ionic strength is complicated by the coupled effects of charged acid and or base species of the buffer contributing to ionic strength. Equation 3.4 quantifies how pK_a changes as ionic strength I is increased or decreased. The screening effects of high charge density means that solutions behave like lesser concentrated solutions.

In this thesis results reported are conducted in buffers of equal ionic strength.

The steps used to calculate and prepare a buffer of constant ionic strength are given in appendix C.

$$pK_a' = pK_a + (2z_a - 1) \left[\frac{A\sqrt{I}}{(1 + \sqrt{I})} - 0.1I \right] \tag{3.4}$$

3.3   The Device
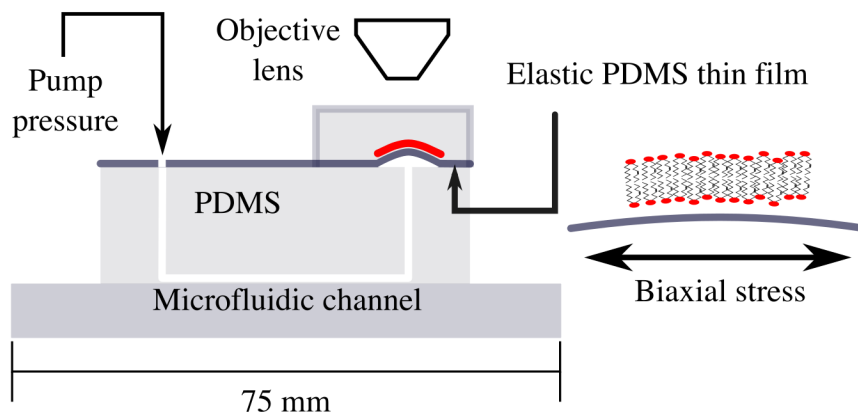
Figure 3.1: Schematic representation of the device used to stress lipid bilayers.

Biaxial stretch of supported membranes is accomplished using the device illustrated in figure 3.1. This device can be used to support lipid membranes on an elastic thin film of PDMS. The area of the PDMS can be changed through the application of a controlled pressure. The device consists of an array of 50 μm high air channels etched into a block of PDMS. A thin disc of PDMS is used to cover one entrance to each channel. The second entrance is connected to a syringe pump. Application of positive pressure to the pump results in an inflation of the PDMS film which changes from a flat disc to a hemispherical cap. Lipids supported on the centre of this hemispherical PDMS cap are thus subjected to a biaxial areal strain.

To produce the channel in the PDMS block, Ultraviolet (UV) lithography is used to pattern a silicon wafer with an array of 50 μm tall features. The silicon wafer is subsequently cleaned, dried and filled with a desired depth of uncured PDMS and left to cure overnight in an oven at $\approx 50°C$. Once cured, the PDMS device may be cut from the silicon wafer complete with the negative imprint of the channel features of the silicon wafer. Holes are made at either end of each channel using

a biopsy punch and the PDMS is covalently bonded to a thick microscope slide through plasma oxidation. The PDMS thin film is prepared by spin coating 1 mL of uncured PDMS onto a clean Petri dish for 10 s at 500 rpm followed by 2 minutes at 2000 rpm using a laboratory spin coating apparatus. The channels are sealed with the thin film of PDMS, also by surface activation through plasma oxidation.

PDMS is natively hydrophobic, hence the PDMS surface is cleaned and rendered hydrophilic through plasma exposure prior to bilayer deposition. A gasket is placed over the ends of the channels covered by the elastic PDMS film and the device is wetted with lipid solution at the desired concentration. Devices are usually made immediately prior to experiments and used within 3 days to avoid deterioration in quality and or contamination of the surface.

3.3.1   The Performance of the Device

Optimisation of the device has meant that the device can achieve reversible deformations of up to 50% in the plane. Such a stretch can be applied over tens of minutes or a few seconds.

(a)   (b)
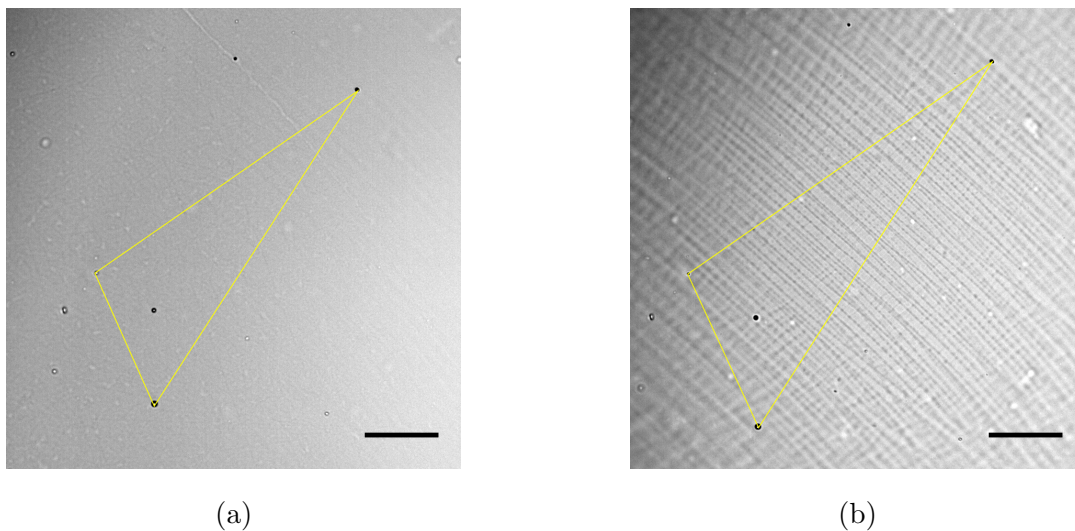
Figure 3.2: The substrate is imaged in the brightfield and sampled at the same rate as fluorescence images. (a) An image of a typical substrate prior to deformation. (b) Typical image after substrate expansion of approximately 33%. Scale bars 50 μm.

The area change of the PDMS is measured by following the displacement of micrometer sized air bubbles embedded in the polymer matrix. These bubbles are

(a)   (b)
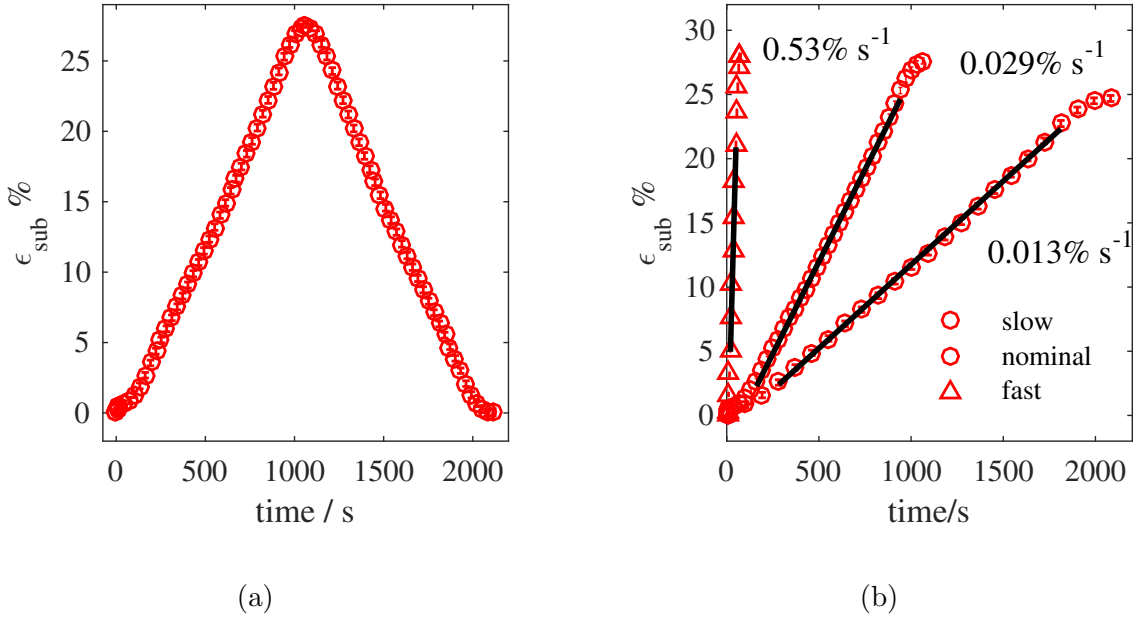
Figure 3.3: (a) Substrate strain, ϵ_{sub}, versus time for an experiment conducted at *nominal* strain rate. (b) Substrate strain versus times for different pump infusion rates. Strain rates are calculated and annotated. Error bars are smaller than the data points.

residual from the degassing process and can be imaged under brightfield illumination.

To calculate the substrate deformation, the coordinates of three or four large features in the brightfield are tracked over time. These coordinates are converted into a polygon area and a substrate strain ϵ_{sub} is defined by equation 3.5; where $A_{sub}(t)$ is the area of the polygon superimposed on the substrate at time t.

$$\epsilon_{sub}(t) = \frac{A_{sub}(0) - A_{sub}(t)}{A_{sub}(0)} \tag{3.5}$$

An example brightfield image at $\epsilon_{sub} = 0$ is shown in figure 3.2a; air bubbles are visible as dark spots embedded in the grey background. Also marked on figure 3.3 are the polygons constructed from 3 brightfield features used to determine a substrate area, in this example the area is a triangle and marked in yellow. Coordinate extraction is achieved efficiently through the use of home-built Fiji [67] plugins that, crop, adjust and segment features of the bright-field image stack and export their coordinates to a spreadsheet (Mircosoft® Excel for Mac® 2011). An estimate of the uncertainty in the substrate area is generated from the size of the tracked features, where it is assumed that the true centre of the feature can lie anywhere

in the segmented zone. This procedure thus weights larger features with a greater uncertainty, in line with the notion that out of focus features will generate a larger, more blurred, image. Figure 3.3a shows the substrate area at *nominal* strain rate, illustrating that the deformation is reversible and elastic. The elasticity is demonstrated by the linear relationship between ϵ_{sub} and time, since this experiment is performed at constant pump infusion rate.

In comparison, figure 3.3b compares the expansion of the substrate area when strain rate is varied. The strain rate of the PDMS substrate can reliably vary over two orders of magnitude. There is some departure in the linearity of the substrate area versus time at high strain amplitude which can be explained by the tracked features moving toward the extremities of the substrate. As mentioned in section 3.3, the PDMS transitions from a flat disc to hemispherical cap when inflated. Only the very centre of this hemispherical cap remains in focus. If the tracked features approach the edge of the substrate then the measured ϵ_{sub} becomes exaggerated. The dynamic range of the device is limited by the rate at which air leaks from the pump-syringe coupling at low strain rate and the speed at which one can maintain focus of the central region of the PDMS disc during expansion and contraction at high strain rate. The focal plane of the objective must be tracked vertically to account for the displacement of the top of the PDMS hemisphere. For experimental reproducibility this is accomplished using the Perfect Focus System (PFS) on the Nikon Ti microscope, the operating principles of which will be described later.

In practice the device can be used to apply controlled strain at rates of between $0.001 - 0.8\,\%\mathrm{s}^{-1}$. Indeed in figure 3.3b one can see the device limitations beginning to show in the substrate strain versus times curves. The maximum amplitude obtained is marginally less for each decreasing deformation rate suggesting that the expansion is competing with a small loss of air volume in the channel. Experiments are usually confined to within a maximum stretch of $\epsilon_{sub} = 50\%$, not due to the elasticity of the PDMS, but rather due to the unknown implications of the appearance of striations in the brightfield images. An example of these striations is shown in figure 3.2b. These patterns could be a consequence of the spin coating procedure of the PDMS thin film onto a Petri dish and may indicate a change in topography at high stretch amplitude.

3.3.2 The Effect of Plasma Treatment

PDMS is a silicon based elastomer that is natively hydrophobic. To render the surface hydrophilic, the PDMS is exposed to a low pressure air plasma using a Tantec®vacuLAB apparatus. Exposing silica surfaces to oxygen plasma has several effects. Notably, the production of silanol Si−OH groups at the surface [68], along with the removal of organic impurities and a subtle decrease in mean square roughness [69]. As a result of the creation of these polar silanol groups, the surface becomes more hydrophilic and interacts with liquid water more favourably.
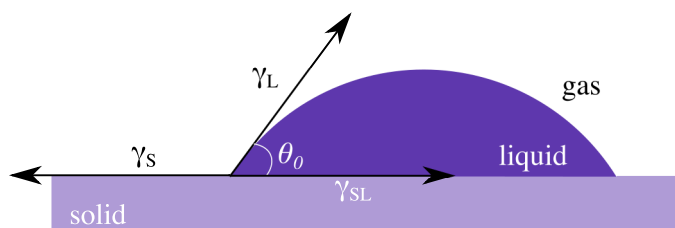
Figure 3.4

The surface hydrophilicity may be conveniently assessed in the laboratory by measuring the angle at the three-phase boundary formed by a liquid droplet sessile on the solid surface. The balance of horizontal forces at the three phase line (figure 3.4), may be used to derive the Young-Dupré equation, equation 3.6 for the angle θ_0 subtended by the tangent from the liquid phase and the solid surface.

$$\gamma_L \left(1 + \cos(\theta_0)\right) = W_{SL} \tag{3.6}$$

γ_L is the surface tension of the liquid phase, defined as the free energy change when the surface area of liquid is increased by one unit. W_{SL} is the adhesive energy of the solid-liquid interface; the reversible work done in separating two unit areas of the interface to infinity in a vacuum [45]. A contact angle of $\theta_0 \leq 90°$ is generally understood to indicate a hydrophilic surface, whilst surfaces with a contact angle of $\theta_0 \geq 90°$ are described as hydrophobic. Strictly speaking, equation 3.6 is only valid if the gas phase is a saturated vapour of the liquid in contact with the solid, otherwise W_{SL} in equation 3.6 must be replaced by the equivalent work of adhesion for the separation of two units of the solid and liquid interface in the gaseous medium. The contact angle θ_0 is a thermodynamic quantity, that is, it tells us nothing about the

nanoscale organisation of molecules at the surface. Its value should only depend on the choice of substrate, and the liquid used [44]. In practice, contact angle values are notoriously hard to reproduce and depend on many non-thermodynamic quantities such as surface chemical heterogeneity, surface roughness and droplet size [70].

(a)   (b)
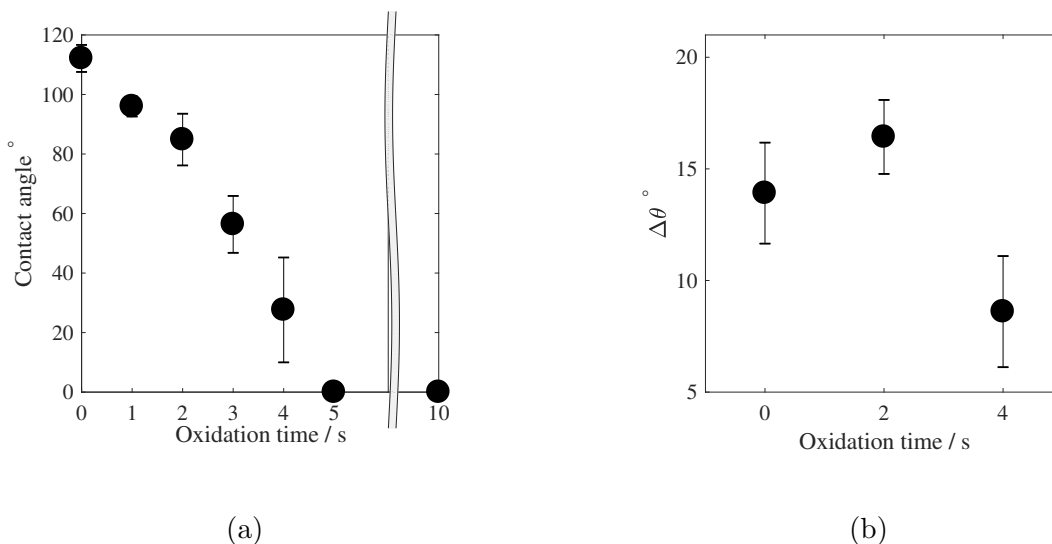
Figure 3.5: Contact angle of a sessile water droplet on PDMS at low oxidation exposure times. Data points represent the average of at least three independent samples and error bars represent the distribution of this data about the mean value. (a) Static contact angle versus plasma exposure time. (b) Advancing and receding contact angles measured on PDMS versus plasma exposure time.

Figure 3.5a shows the angle of a sessile 20 μL drop on PDMS coated glass slides exposed to plasma oxidation for varying times. Data points are obtained over several days and the error bars reflect the range of data collected. A monotonic decrease in water droplet contact angle with respect to PDMS plasma exposure time is evident; indicating an increase in surface hydrophilicity.

It is impossible to know the exact effect of a given plasma exposure time on the substrate on a given day. This is a consequence of either day-to-day changes in the efficacy of the plasma treatment process and/or the aforementioned non-thermodynamic quantities that can stabilise a contact angle at a value that is different from the true thermodynamic value. In addition, it is difficult to account for variations in the laboratory pressure, humidity and temperature.

In order to maximise the reproducibility of the contact angles, PDMS films were

spin-coated onto cleaned glass microscope slides and the droplet volumes were fixed at 20 μL. The contact angle measuring apparatus was also mounted above a large beaker of water to saturate the vapour around the sessile droplet, in line with the requirements of equation 3.6 and to minimise the effects of droplet evaporation. The static contact angles on PDMS provide a useful means of characterizing the hydrophilicity of the substrate. A partially hydrophilic substrate is defined for a plasma oxidation time of $2 - 3$ s, that yields a static contact angle of $40 \geq \theta \leq 90$. A hydrophilic substrate is defined for fixed plasma exposure time of 30 s.

It is also useful to comment on the observed contact angle hysteresis reported in figure 3.5b. The difference between the contact angle for a droplet of increasing volume, compared to a droplet of decreasing volume, is known as the adhesion hysteresis, $\Delta\theta$. The value of $\Delta\theta$ can be used to asses the degree of chemical or topographical heterogeneity that a surface may posses. The adhesion hysteresis displays no obvious correlation with plasma oxidation time but the magnitude of $\Delta\theta$ is at least $6\,°$ even at 4 s. What can be taken from figure 3.5b is that the PDMS surface, at low oxidation times of $0 - 5$ s is not a uniform interface and must exhibit some chemical or topographical heterogeneity sufficient to stabilise a macroscopic water droplet at the interface and support adhesion hysteresis.

3.3.3   Solution Exchange

In later experiments it will be shown that the way in which the bilayer responds to substrate deformation can be tuned by using different buffers. Therefore some experiments require the exchange of buffer between substrate stretch and compression cycles. This is best accomplished using devices set-up for imaging under the confocal microscope. For such experiments one may use a water-dipping lens and consequently there is no need to seal the chamber with a cover slip. This does however create a protocol issue. The solution cannot be completely removed because this would destroy the bilayer, which must remain in aqueous solution. Instead the chamber contents must be exchanged by removing most of the chamber volume with a pipette and replacing this volume with the new solution. The immediate problem is that the contents of the solution now surrounding the sample is not a *pure* solution but is instead a weighted average of all the previous solutions.

To answer this problem quantitatively one may start with simple solution of pure x. If a fraction f of this solution volume is removed and replaced with solution y, how many times must the chamber be washed in this way before, within the limits of experimental confidence, one can say that the chamber contents has been replaced?

A simple way to find a lower limit to this problem is to fill a PDMS gasket with a fluorescein solution of concentration $c0$ and repeatedly replace a fraction of the volume f with pure water. Over the course of n washes the concentration of fluorescein exponentially decreases to zero. Thus, the mean intensity recorded at the Charge Coupled Device (CCD) of the confocal after sufficient equilibration time should fit well to equation 3.7.

$$c_n = c_0 \exp^{-\ln(f)n} \tag{3.7}$$
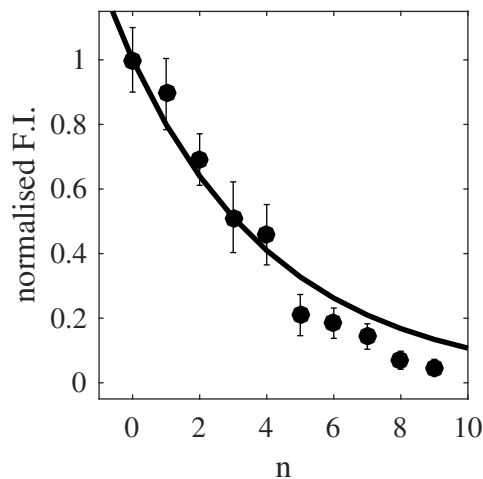
Figure 3.6: Mean image intensity obtained after n dilutions of a fluorescein chamber. Error bars represent the standard error in intensity over 3 repeat measurements. Equation 3.7 is superimposed on the data in solid black.

Figure 3.6 plots the mean intensity of a 512×512 pixel confocal scan at the same focal plane as a function of the number of washes n of the chamber with the volumetric exchange fraction $f = 0.2$. Equation 3.7 is also plotted over the same data. For the experiment a factor $f = 0.2$ was used to capture a sample of fluorescence images without the requirement of changing the pixel dwell time or laser intensity. The data are in reasonable agreement with the equation 3.7 except at high n. This is likely a result of the breakdown of the assumption of a linear relationship

between measured fluorescence intensity and fluorescein concentration. Regardless, it is clear that after only 10 washes at a volume factor of $f = 0.2$ a substantial reduction in fluorescein concentration is achieved. On this basis, all experiments reported that require chamber volume exchange will have had at least 20 washes at a minimum volume exchange factor $f = 0.5$.

3.4   Microscopy

Microscopy is useful as a tool for the study of biological structures and hierarchies. This is due to the non-invasive nature of imaging and the typical length scales over which a microscope can operate; approximately $0.1 - 10000$ μm [71]. Optical microscopic techniques can broadly be divided into two main types of image contrast, brightfield and fluorescence. In brightfield microscopy the image contrast is generated primarily by differences the way in which components of the sample redirect or absorb light [72]. Fluorescence staining is more frequently used in biophysics [71]. In this technique part of the specimen is labelled with a fluorophore, a molecule that absorbs optical light of one wavelength and emits at longer wavelength after a characteristic lifetime [73, 74]. In particular, lipid bilayers can be made visible under fluorescence excitation by the incorporation of a low molar fraction of a lipid, fatty acid or sterol derivative with a fluorophore chemically attached, typically $0.1 - 0.5$ mol%.

Inverted Nikon Ti: The inverted Nikon® Ti microscope can be used for epifluorescence illumination and TIRF microscopy. Under epifluorescent illumination light is coupled in from an arc discharge lamp through a filter cube, which selects the wavelength of excitation. This may then be condensed onto the sample *via* the objective lens where all fluorescent molecules in a cone of illumination are excited. The resulting emission is then recollected by the objective lens and diverted *via* the same filter cube to the binoculars or a Complementary Metal-oxide Semiconductor (CMOS) camera where photon intensity is recorded. The Nikon Ti is also equipped with a laser box, VersaLase®, and an oil immersion lens with sufficient numerical aperture, $NA = 1.49$, to perform TIRF imaging. In this configuration, incident laser light is first focused onto the back focal plane of the objective such that all

rays emerging from the objective are parallel. The beam is then translated to the outskirts of the objective at an angle of incidence that exceeds the critical angle θ_c. Total internal reflection subsequently ensures the production of an evanescent wave at the interface that excites fluorophores only in a thin portion of the specimen. The emitted light is then collected by the objective and directed toward the binoculars or camera as in epifluorescence mode.

A particularly useful feature of the Nikon Ti is the PFS. This system makes use of the reflection of an infrared beam from the sample cover glass to fix the distance between the objective and sample. As a consequence, the microscope is able to maintain focus over long periods of time by adjusting for thermal expansion and/or displacements of the sample plane caused by acoustic vibrations. This system gives the microscope the unique ability to track surfaces with a translating z coordinate. The device described in section 3.3 has a focal plane that moves in the z direction thus, the PFS system is extremely useful. Deformation of the elastic surface causes the glass cover-slip to bend, due to the incompressibility of water. The PFS uses interference of an infra-red beam, reflected from the cover-slip, to track the displacement of the cover-slip and subsequently fix the distance between the objective and the sample focal plane (figure 3.7).
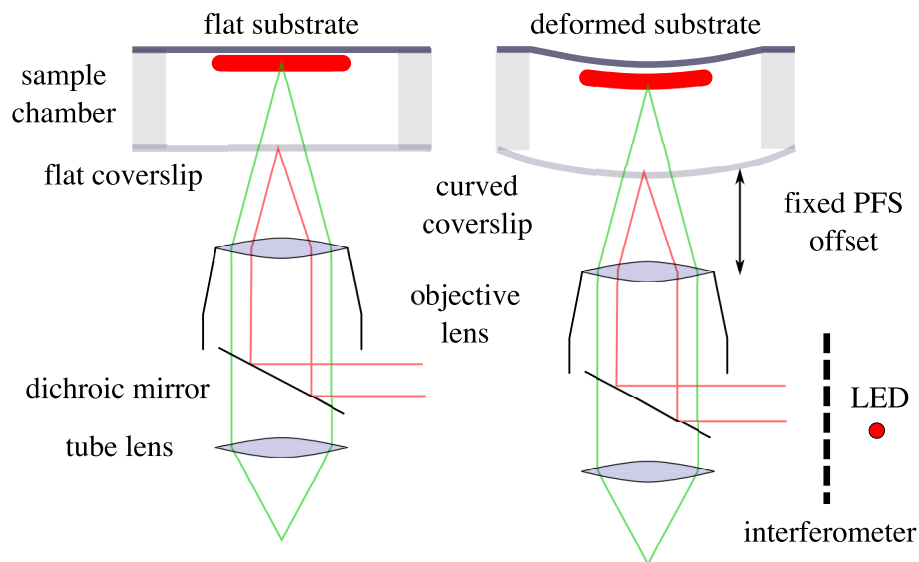
Figure 3.7: Schematic illustration of the operating principles of the perfect focus system installed on the Nikon Ti microscope.

The Nikon-Ti, due to its inverted configuration, can only be used for fixed exper-

imental conditions. The buffer surrounding the sample must be sealed with a cover slip and therefore cannot be exchanged between substrate deformations. Despite this limitation, the automated focussing afforded by the PFS system produces superior image quality in comparison to the confocal microscope; therefore the Nikon-Ti provides the majority of the experimental data reported here.

Confocal Microscope:

The confocal microscope makes use of a pinhole to block the emission from fluorophores that are excited in the illumination volume, but are positioned above or below the focal plane of the objective. Laser light is focused and rasterised across the sample, thereby generating optical sections. Fluorescence emission is subsequently captured and amplified by a photomultiplier tube. The confocal is particularly useful for imaging thin sections of very thick samples, for instance cells. However, the experiments reported in this thesis refer only to very thin bilayers. The signal to noise increase afforded by the confocal system is therefore not fully appreciated here. On the other hand, the upright configuration and compatibility with water dipping lenses makes the confocal ideal for experiments in which the contents of the buffer need to be exchanged between substrate deformations. The confocal can also be used to perform FRAP fluidity tests, the full protocol for which will be described shortly.

Good Microscopy Practice

Prior to any brightfield imaging, Köhler illumination was always tested for. This ensures that the illumination light is focussed onto the front focal plane of a condenser lens, such that all source rays passing through the sample plane are parallel. This results in even illumination of the sample and prevents the formation of the image of the light source on the retina; as is the case for critical illumination. Regular checks for dust accumulation in the optical pathway were performed as part of the laboratory cleaning procedure and the point-spread function of the microscope was used as a quality assurance metric for the Nikon Ti. Appendix D, documents how the point spread function may be imaged.

3.5   Fluorescence Recovery After Photobleaching

Fluidity of both SLBs and Supported Lipid Patch (SLP)s is easily confirmed using the Confocal microscope. A FRAP test can be used to distinguish between Supported Vesicle Layer (SVL)s and SLBs. Increasing the laser power and rapid scanning of a small area delivers enough laser intensity to permanently kick a fraction of the fluorophores in the sample into a state where they are no longer able to fluoresce. Because individual lipids within a bilayer diffuse within the plane, the fluorescence intensity in the bleach zone will equilibrate with the rest of the sample over time, as fluorescent molecules move into the bleach zone, and non-fluorescent molecules move out. The numerics of fluorescence recovery after photobleaching under diffusive conditions were first described by Axelrod in 1976 [75] and later adapted for practical implementation [76] and for alternative bleach spot geometries [77]. Robust measurement of 2-dimensional diffusivity requires that the bleaching time is less than 5 % of the characteristic diffusion time of an individual lipid[2]. In addition, the bleach area must be negligibly small in comparison to the extent of the bilayer. The protocol for FRAP analysis, adopted herein, is an adaptation of that that found in reference [78]. An area measuring 5×5 μm^2 is bleached for 12 frames, each frame typically lasting 1.040 s. The field of view is then expanded to 224×224 μm^2, and the recovered intensity is recorded for a further 120 frames each lasting approximately 2 s. Whilst these criteria do satisfy that the bleach area is significantly smaller than the imaging window, typical characteristic times for this protocol are around 5 s, less than the bleaching time of 12.5 s. This results in the blurred edge that is usually observed in the FRAP recovery image stacks. Inactive fluorophores are diffusing out of the bleach zone during the bleaching. Because of this, the diffusion coefficient obtained is used only as qualitative comparison between samples and as a means of verifying fluidity in supported lipid bilayers. The only meaningful quantitative distinction is a diffusion coefficient of zero, which indicates a supported vesicle layer.

---

[2]The characteristic diffusion time is the mean time required for an individual lipid molecule to traverse an area equal to the bleach spot.

3.6 Image Segmentation

Quantitative feature extraction from images can be a subjective process. Indeed the act of rendering an image on a computer screen cannot be achieved without some form of data manipulation. This is because most cameras record photon intensity in a format with a bit depth that exceeds monitor pixel range [79]. The human eye is, additionally, more sensitive to certain colours. As a consequence the process of image rendering can in itself make objects appear artificially brighter, relative to others. An image, ultimately, is a matrix of numbers. The image header may contain other information such as how the grid of numbers should be arranged spatially and/or information about the image acquisition parameters. Features within images are gradients in intensity values. The process of image analysis is identifying and extracting these gradients. However, due to image and experiment noise, these gradients can be difficult to identify.

Image noise contributes to the uncertainty in all quantities extracted from microscopy experiments. Sources of image noise include the quality of focussing, photon and read noise[3] from the camera and the resolution of the microscope itself. Out of focus images or frames in video acquisitions are convoluted with the Point spread function (PSF) of the microscope; this has the effect of increasing the apparent size of features. The resolution of the microscope only becomes important when the feature size is comparable to the size of a diffraction-limited spot or the separation between feature sizes is similar to the wavelength of the illumination light. However, another important source of uncertainty arises from the methods of feature extraction applied, using software, post image acquisition. To delineate features or areas the spatial distribution of brightness must be contrasted across the image. This procedure involves, at same point, the imposition of a certain cut-off value in intensity, to which you weight a pixel as being either being part of the feature or not. There exist algorithmic methods of choosing this threshold value but the

---

[3]Read noise is Gaussian such that the mean value is zero and the standard deviation of the noise is the same across the entire image. The noise arises from the quantification of photon count at the camera. In contrast, photon noise is Poisson and depends on local image brightness. Its origin stems from the inherent randomness of photon emission from a given fluorophore. To detect something meaningful, one must collect an average of a large number of observations to obtain the mean rate of photon emission [74].

choice of algorithm is user dependent. Therefore, the process of feature extraction can yield different results when a different operator performs the analysis. This means that one must take care to assign meaningful and significant error bars to extracted quantities. In the following section some of the fundamentals of image analysis as well as some of the precautions taken to ensure that the quantification of images has been performed methodically and transparently will be reviewed.

3.6.1 Filters & Background Subtraction

Firstly, the process of changing individual pixel values within an image is known as filtering [80]. Filtering can be used to remove noise from images and subsequently enhance gradients [45]. The process of image filtering is demonstrated in figure 3.8. Computationally, image filtering is established by convoluting an image matrix with a smaller image known as a kernel. The kernel is a matrix of weights describing how each neighbouring pixel value in the original image should contribute to the value displayed in the new image. By translating the kernel across all pixels in the source image, a new image may be generated which is a linear combination of the pixel intensities in the source. It is often impossible to recover the original image post manipulation. For this reason, filtering should always be applied to duplicate copies of raw data.

One of the important uses of filters is the process of background intensity removal. All images inherently have some form background signal onto which image features are added. Even if the acquisition is well calibrated according to the image contrast, a finite signal to noise ratio will exist. Background intensity can come from image noise, out of focus features, stray illumination light or anything in the light path that produces undesirable scattering. If the background varies across the sample, as is the case for uneven sample illumination in brightfield microscopy, then this may show up in any attempt to automate feature detection in acquired images. For this reason it is often desirable to *subtract* a background image from data. This is akin to forming and then subtracting an artificial image that would have been generated in the absence sample features. There are many ways to accomplish background subtraction [81]. In this work an image that is the convolution of the source image with first a minimum, then a maximum and finally a Gaussian blur kernel,

Original image

Kernel image

w1	w2	w3
w4	w5	w6
w7	w8	w9

12	255	14	5	6
38	42	128	55	1
30	254	22	21	92
148	101	118	21	43
5	1	122	155	19

Figure 3.8: Applying a filter to an image involves replacing each pixel value in the original image with a weighted average of neighbouring pixel values. The new value of the pixel outlined in red in this example would be $w1 \times 42 + w2 \times 128 + w3 \times 55 + w4 \times 254 + ...w9 \times 21$.

whose radius exceeds the size of the features to be extracted, is constructed and then subtracted from the source image. The minimum filter has the effect of replacing each pixel with the minimum intensity value within the radius of the kernel, the maximum replaces each pixel intensity with the maximum value in the kernel radius and Gaussian blur weights each pixel according to a two dimensional Gaussian function that peaks at the kernel centre. For example, the maximum filter acting on the simplified example in figure 3.8 would replace the value of 22 in the red pixel with 254 because this is the maximum value within the the 3 pixel kernel radius. The effect of this method of background subtraction is illustrated in figure 3.9. Figures 3.9a and 3.9b show brightfield images of a thin film PDMS substrate before and after background subtraction respectively, whilst figure 3.9c plots the fluorescence intensity across both images. The lower red line in figure 3.9c represents the fluorescence intensity values extracted from the background subtracted image; an arbitrary constant has been added to the signal for easier comparison. It is clear that the signal is much flatter for the background subtracted image (figure 3.9b) compared to that obtained from the source image (figure 3.9a).

(a)   (b)   (c)
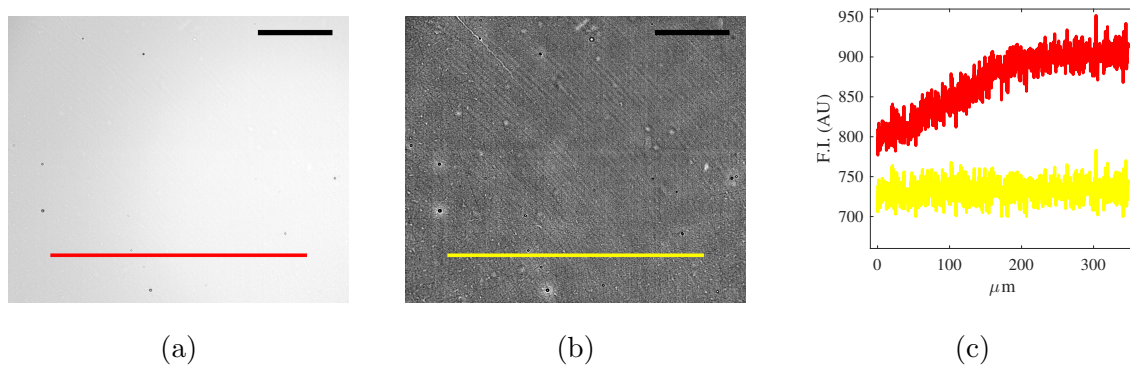
Figure 3.9: Background image subtraction. (a) sample brightfield image of a PDMS substrate. (b) the same micrograph shown in (a) with the background removed. (c) line scan fluorescence intensity across the red line in (a) and yellow in (b). Scale bars 100 μm, shown in black.

3.6.2 Thresholding

When it comes to extracting features a threshold must be imposed in order to classify pixels as either part of the feature or not. This has the effect of creating a binary image where a pixel has an intensity value of either 1 or 0. The choice of thresholding method affects the value obtained from the image analysis; the example given in figure 3.10 shows systematically larger areas attributed to the moments method of thresholding. Standard procedure for reporting errors is to report the mean of a preferably large number of observations together with the standard error, which is derived from the standard deviation in the data. This is not always possible in the experiments documented here due to the difficult task of setting up identical initial conditions. As a consequence individual samples are often selected as faithful representations of the behaviour observed for a class of experiment. When it is necessary to report an experiment in this way an error must be assigned based on the accuracy of the features extracted. Area changes or trends are reported frequently and as a consequence, the most common choice of error is one that is proportional to the perimeter of the shape measured. The reason for this is that the threshold position moves the interface between pixels belonging to the feature and pixels not belonging to the feature. The pixels for which the uncertainty is greatest can thus be found at the edge. Assuming a normal distribution of erroneous classifications of pixels as feature or non feature, the perimeter can be multiplied by a number drawn

from a normal distribution ranging from 0 to 1, which gives us an estimate of the number of uncertain pixels in our classification. This is the most common practice used to generate uncertainties for the experiments documented in this thesis. The method does produce an uncertainty that is proportional to the size of the feature detected. However this makes sense because features with a larger perimeter have more *chances* to have pixels erroneously classified as belonging to the feature or not.

In practice, when it comes to choosing a threshold algorithm, one can use visual inspection to identify the more reliable transformation to binary. In figure 3.10, the Otsu method of thresholding (figure 3.10b) is clearly a better representation of figure 3.10a than the moments based method (figure 3.10c). For this reason it is desirable to use the same method of thresholding for each experiment reported. Using the same method of thresholding ensures that the pathway from experiment to numerics is repeatable. This is where ImageJ® scripts and macros become extremely useful.

(a)   (b)   (c)
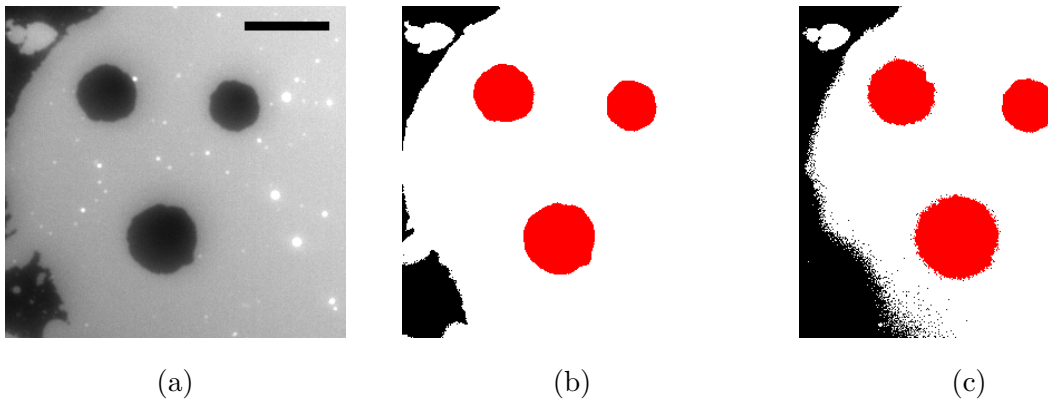
Figure 3.10: The choice of threshold can alter the value obtained from feature extraction. (a) example gray scale fluorescence micrograph supported membrane patch showing 3 dark circular pores. In this case, the pores are the features to be segmented from the image. Scale bar 25 μm. (b) Otsu's [82, 83] method of thresholding. (c) Threshold determined using the moments algorithm [84]

3.6.3   A Workflow for Image Analysis

Images are stored in raw format as well as tif images, which have the benefit of not modifying any intensity values during conversion. Tif files are subsequently duplicated prior to any modification before being transferred to the desktop for

further processing in ImageJ. ImageJ is a cross-platform, open source and powerful piece of software for quantitative image analysis[45, 80], and has proved extremely robust for the experiments reported herein. ImageJ can easily be extended and customised to achieve tasks specific to a given workflow. This is achieved through the generation of macros and macro sets that allow for rapid implementation of repetitive tasks to a reasonably large sample set. By recording the analysis procedure in a macro the pathway from image data to numerical data is made transparent and repeatable, to combat the subjectivity associated with positioning of thresholds in images. A large class of images can then be analysed efficiently and in the same way, increasing our confidence in the trends reported. All of the more frequently used macros used to extract numerical features are included in appendix A.3.

Data is extracted and stored in an Excel® spreadsheets before being transferred to MATLAB® for subsequent plotting.

Chapter 4

Methods of Supported Lipid Bilayer Formation

4.1 Review of Continuous SLB Formation by Spontaneous Vesicle Fusion

The process of forming a bilayer on a solid support can be achieved in many ways, but a particularly facile approach, pioneered by McConnell *et al.* [14], is the method of SLB preparation *via* the spontaneous fusion of vesicles. The process is now ubiquitous in research laboratories but is still poorly understood [15, 85]. Successful rupture of vesicles into a continuous lipid film depends on an enormous list of experimental factors. These include the valency and concentration of ions in the buffer, the buffer pH, the chemical and physical properties of the lipids, substrate charge, substrate hydrophilicity and the temperature at which the deposition occurs [86]. Indeed in circumstances where the membrane-substrate interaction is highly unfavourable fusogens, such as polyethylene glycol, may be required to promote SUV rupture and spreading [87].

The formation process can be broken down into steps. Firstly, vesicles adsorb from the solution onto the surface where they may become trapped in a metastable state [85]. The adhesion of a single vesicle to the substrate represents a competition between the adhesive and repulsive forces acting between the membrane and the substrate. This interaction will include the Van der Waals force of adhesion, EDL

repulsion and steric repulsion due to either solvation forces and or the confinement of membrane undulations [44]. For successful adhesion of the vesicle to the surface, this potential energy must have a minimum with respect to the vesicle's lateral displacement. Since, even for SUVs, a typical vesicle radius will be in excess of 100 nm, which is much larger than the equilibrium separation in this potential energy function, it is safe in most circumstances to encompass all of the interaction potential into a single bilayer-substrate contact potential, W_{ad} [46]. It is obvious that increasing this value of W_{ad} will increase the probability of vesicle adhesion and subsequent rupture and spreading. Experimentalists have numerous tools available to modulate the value of this contact potential.

The inclusion of neutral salts in the buffer can screen EDL repulsion between charged membranes and surfaces, thereby increasing the likelihood that the VdW adhesion wins out over repulsive forces. In particular Anderson *et al.* identified the importance of a high ionic strength buffer when forming a bilayer from zwitterionic SUVs on silica substrates. Silica, or glass surfaces, dissociate in aqueous solution by losing protons and therefore obtain a negative surface potential [88]. By combining the use of a surface force apparatus, together with a quartz crystal microbalance to follow mass adsorption, the adhesion of the vesicles to the substrate has been shown to be significantly less in a buffer of 1.5 mM ionic strength compared to 150 mM NaCl [89].

The EDL repulsion is important, but the picture is not complete. Notably absent from the work of Anderson *et al.* is a discussion of the hydration force, the force required to squeeze out the water of hydration from the lipids, or remove water which may be bound to the charged substrate [51, 90]. Hydration repulsion between incoming vesicles and the substrate is regularly described as being the dominant barrier to successful bilayer formation. Substrates with well defined levels of hydration such as aluminium or titanium oxide provide unique insights in this respect [91, 92, 93]. For such systems the degree of surface hydroxylation[1] can be titrated with the pH of the aqueous environment. As a consequence the buffer pH emerges as a useful tool to encourage successful bilayer formation by diminishing the amount of water that must be removed before the vesicle can bind to the substrate. These ob-

---

[1]Dissociation of protons from the surface.

servations have also been confirmed on nanoparticle substrates [94] where the degree of surface hydroxylation can additionally be controlled by heat treatment.

Related to the hydration force is the substrate hydrophilicity, which is macroscopically defined by the contact angle between a water droplet and the surface. Substrate hydrophilicity not only affects the probability of successful bilayer formation and the physical properties of the bilayer once formed [69], but also the ability of the bilayer to propagate and spread over the surface [95, 56]. There must then exist an analogy between the way a water droplet spreads on a surface and the way a vesicle, composed of highly hydrated phospholipids, spreads over a substrate [96].

i.) Colloidal interactions

ii.) Adhesion

iii.) Fusion & Rupture

iv.) Spreading

Substrate
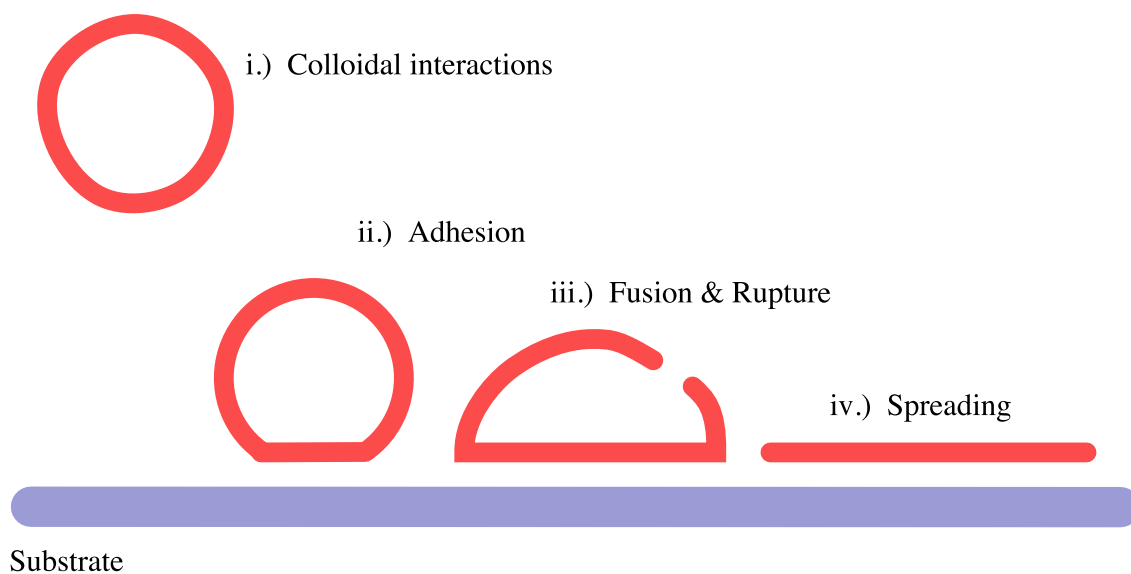
Figure 4.1: Schematic illustration of the spontaneous adhesion, rupture and spreading of a single vesicle interacting with a support.

As the adhesion energy increases, the vesicle is encouraged to spread and cover more of the surface, transitioning from the shape of a truncated sphere to a flat pancake. Since the internal volume and membrane area must be conserved there exists a tipping point at which the bending energy due to the shape change can become comparable to the contact potential, W_{ad}. If this situation arises, the vesicle spreading process will be arrested and a metastable SVL will be formed [47]. If the contact potential is increased further and begins to exceed the energy due to bending then tension will begin to accumulate in the membrane [97]. This heightened tension increases the probability of vesicle rupture and subsequent spreading. Rupture involves a topological change from a closed bilayer shell to a flat supported

membrane that necessitates the formation of a pore in the membrane. This reconfiguration of lipid at the pore edge is the origin of the activation energy barrier to vesicle rupture [10]. Once surpassed, however, the presence of a bilayer edge due to the rupture of a single vesicle can drive the rupture of nearby vesicles, creating a cascade of rupture events and the spreading of a continuous lipid film [98]. Each of the 4 stages during vesicle formation *via* spontaneous vesicle rupture are illustrated in figure 4.1.

4.1.1   Bilayer Formation by the Spontaneous Fusion of Giant Vesicles

Fusion of GUVs to substrates has been exploited to great effect in recent years [99, 100] as an alternative mechanism for the formation of a supported lipid bilayer. The volume of literature associated with SUV rupture on substrates dwarfs the number of studies conducted on the rupture of GUVs on planar supports. However, the thickness of the hydration layer on the substrate has, likewise, been shown to act as an effective tool for controlling GUV rupture and spreading as well as the inclusion of divalent salts in the buffer, which are known to adsorb preferentially to lipid head groups [101]. Fluorescence microscopy has been used to follow the rupture of GUV on glass substrates [102]. Here the authors identified multiple mechanisms of GUV rupture, the kinetics and probability of which were found to be strongly influenced by the average curvature of the lipid.

In many respects the use of giant vesicles over small vesicles has numerous advantages; the process is governed by the same colloidal type interactions and the fusion can be monitored directly by optical microscopy. Moreover, the lateral size of the bilayer film formed from the spontaneous wetting of SUVs usually greatly exceeds the field of view of most microscope objectives. In contrast GUVs can be prepared readily with diameters between $1 - 100\ \mu$m, hence forming lipid patches with areas that fall within an objective field of view. This makes the system convenient because the changes in the membrane plane can be tracked whilst simultaneously measuring any changes to the total membrane area.

In the following I will present experimental results referring to the conditions necessary for the formation of supported patches from giant vesicles on PDMS. The

process is strongly dependent on the PDMS oxidation time, and hence hydrophilicity, as well as the chemical constituents of the buffer. A parallel may be drawn to the available literature regarding the spontaneous rupture and spreading of small unilamellar vesicles.

4.2 Results

PDMS is a silicon based elastomer, section 3.3.2, which is natively hydrophobic, but can be rendered hydrophilic through exposure to low oxygen plasma [23]. The use of silica surfaces for membrane supports has already been justified [13] but successful bilayer formation depends on many factors. The question that naturally arises is, what can be learned from imaging the interaction of a single GUV, with a diameter easily imaged using optical microscopy, on a polymer substrate that has chemical properties which are analogous to silica?

This problem can be addressed by preparing a simple substrate, consisting of a glass coverslip with a spin coated layer of PDMS 60 μm thick. A chamber can be made using a PDMS gasket. The GUV rupture process can then be imaged by filling this chamber with buffer and adding a small concentration of GUV suspension. Vesicles approach the substrate, adhere and subsequently rupture, depending on experimental conditions. Key players emerge in the vesicle substrate interaction and these can be identified by studying the rupture probability in different experimental conditions.

The results are divided according to the substrate plasma exposure time, for which four categories are identified, native PDMS , insufficiently hydrophilic, partially hydrophilic $(2-3)$ s and hydrophilic for which the contact angle $\theta_0 = 0$ and the oxidation time is greater than 10 s. This categorisation is explained in section 3.3.2.

4.2.1 Monolayer Formation on Native PDMS

In figure 4.2a a sample of GUVs have come into contact with a hydrophobic PDMS substrate. In this case the GUVs have been made sessile by a density mismatch between the internal and external contents of the solution. The GUVs are

(a)   (b)
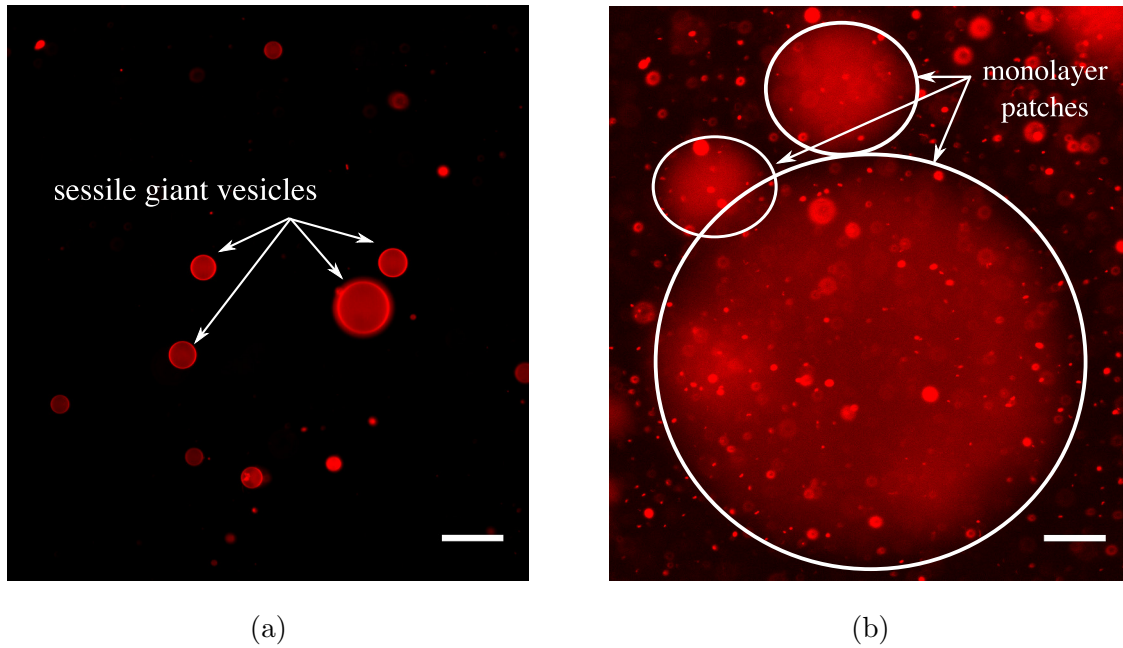
Figure 4.2: Giant Unilamellar Vesicles interact unfavourably with hydrophobic PDMS substrates. (a) Sessile GUVs, in glucose solution, at the hydrophobic PDMS surface. Scale bar 50 μm. (b) In a buffer of high ionic strength (150 mM) GUVs burst and form monolayer patches on hydrophobic PDMS. Scale bar 50 μm.

prepared in sucrose solution and then suspended in glucose solution of equal osmolarity. Since sucrose has a greater molecular mass than glucose, and both molecules are membrane impermeable on experimental timescales, the GUVs sink to the bottom of the imaging chamber. Clearly, under these conditions, where the ionic strength of the solution is zero, the interaction between the vesicle and the hydrophobic PDMS due to the lack of buoyancy is insufficient to promote GUV rupture or adhesion. GUVs cannot be made to interact with the PDMS substrate simply due to a density mismatch of the internal and external contents of the vesicle.

If instead the GUVs are incubated above the hydrophobic PDMS in a high ionic strength buffer then, consistent with reports of monolayer formation on unoxidised PDMS, GUVs burst to form monolayer patches [103, 104]. Figure 4.2b, shows an example patch of monolayer lipid formed from such an event, in 150 mM NaCl, TRIS buffer. The diffuse edge of the lipid patch in this image is characteristic of a lipid monolayer [69]. In addition, there is a large amount of fluorescent aggregate visible in suspension in image 4.2b. This is a direct consequence of the violent pathway from bilayer vesicle to monolayer patch, which releases a large quantity of lipid into the

solution. These amphiphiles presumably assemble rapidly into micelles and small vesicle aggregates; based on the arguments of section 2.1. The redistribution of the lipid from vesicle to monolayer patch is induced only by the presence of the support and the vesicle support interactions. The buffer is designed such that no osmotic perturbation is applied to the vesicle (section 3.2.4).

4.2.2   Supported Vesicle Layer
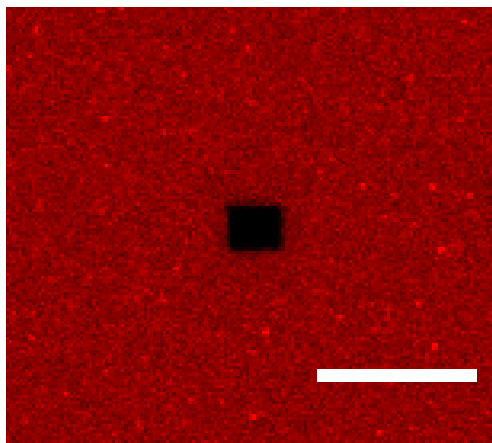
Figure 4.3: Supported vesicle layers do not recover after photobleaching. Scale bars 20 μm.

If the PDMS hydrophilicity is somewhere between the low surface energy required to produce a monolayer and the higher surface energy required for vesicle fusion a stable adhered vesicle layer can form. This situation can be achieved by oxidising the PDMS for a very brief period of between $1 - 2$ s.

The formation of an SVL is common when working with SUVs on PDMS exposed to plasma oxidation for short periods of time. Figure 4.3 shows a supported vesicle layer with a 5 μm^2 square of zero fluorescence achieved through photobleaching. At first it is difficult to distinguish an SVL from a continuous lipid bilayer. However an unchanged bleach spot 240 s after bleaching indicates an absence of long range diffusivity which is characteristic of a supported vesicle layer. The square edge tells us not only that lipid is unable to move into the bleach spot to recover fluorescence, but also that the bleached lipid is also unable to diffuse out of the bleaching region. The high frequency with which supported vesicle layers occur when working with SUVs on PDMS exposed to plasma for short periods is because of the broad distribution in

the measured contact angle between a sessile water droplet and a PDMS substrate for a given oxidation time in the $1-5$ s range; see section 3.3.2. It is very difficult to correlate the formation of a SVL with a specific oxidation time because of the day to day fluctuation in the effectiveness of the plasma treatment. In other words just 2 s of treatment on one day may be enough to produce a continuous membrane, but insufficient on another.
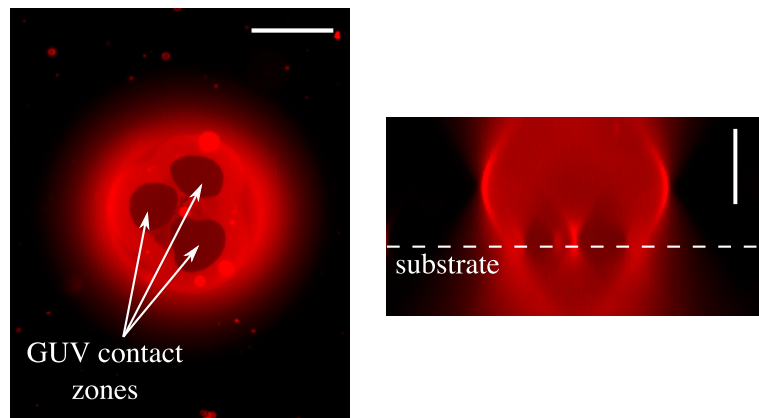
Figure 4.4: Supported vesicle formed from a single GUV. A single vesicle, exhibiting multiple contact zones (left) together with the lateral axis projection of the same vesicle (right). Scale bar 50 μm.

Supported vesicles can also be formed using GUVs. For similar substrate hydrophilicities, where the substrate-vesicle interaction is insufficient for the complete rupture of a vesicle and the formation of a patch, GUVs may adhere to the surface. In such situations, it is frequently possible to see a flattened *contact* zone between the deformed vesicle and the surface. Circular contact zones are clearly visible in figure 4.4 as dark circles within the high fluorescence of the adsorbed vesicles. In figure 4.4 there are three disconnected contact zones visible in the same vesicle. Figure 4.4 also includes the lateral projection of the vesicle, assembled by resequencing images acquired at different focal planes. The lateral axis projection in figure 4.4 demonstrates that the vesicle is *squashed* against the substrate surface.

4.2.3   Partially Hydrophilic Supports

A marginal increase in PDMS plasma treatment time is sufficient to increase the probability of GUV rupture, leading to successful patch formation. A sample of a few
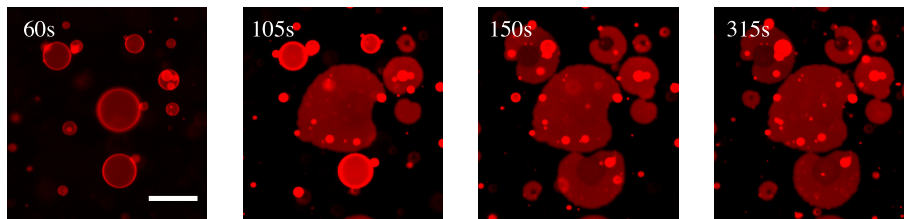
Figure 4.5: Timelapse images of several GUVs fusing onto a partially hydrophilic substrate. Scale bar 50 μm.

rupture events are illustrated in the montage of figure 4.5. Not all GUVs rupture at the same time and GUVs can remain in contact with the surface for varying lengths of time prior to rupture, even on identical substrates. The individual rupture events are therefore stochastic. Another important thing is that as the vesicle ruptures on the partially hydrophilic substrate there is an excess of lipid that sits on top of the patch. This extra lipid is visible as bright fluorescent circles on top of the patches in the later images (figure 4.5). In chapter 5, it will be shown that this excess lipid can serve as a reservoir of membrane to buffer substrate stress in dynamic experiments. This lipid is present immediately after the individual GUV rupture event. The final remark that should be made is that the patches are not circular. Although, one would expect circular membrane patches to form as this minimises the length of the patch edge with respect to membrane area, this is not experimentally realised.

Comparing the differences between the ruptured vesicles in figure 4.5 and the unruptured but adhered vesicles in figure 4.4, suggests that the partially hydrophilic substrate is just on the cusp of being able to promote vesicle rupture. A mere 1 s difference in oxidation time is sufficient to trigger the transition from the adhered vesicle layer to the fully planar patch. As such, it should be possible to experimentally modulate the probability of GUV by using appropriate experimental parameters.

Indeed, this turns out to be the case. By examining a large number of individual GUV rupture events, one can determine a probability of GUV fusion and this probability is seen to vary according to the buffer pH (figure 4.6). A slight problem is encountered here because a single buffer molecule that can span the entire pH range of the experiment has not been used. As a consequence one must use multiple independent buffers to verify observations to avoid buffer molecule specific effects.
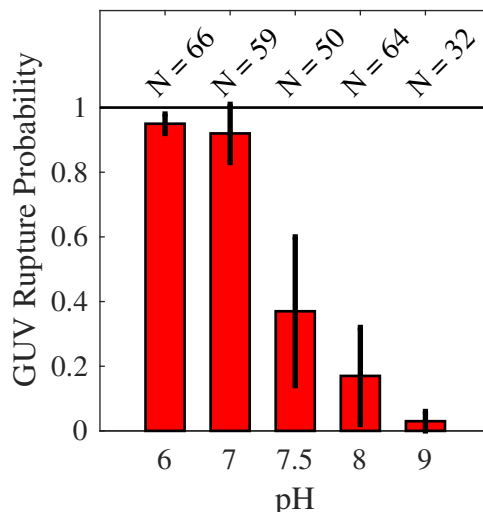
Figure 4.6: GUV rupture probability, as a function of buffer pH, on partially hydrophilic PDMS substrates. Data points correspond to the mean of N independent measurements at the same pH; the errorbars are the standard deviations about the mean.

In figure 4.6, the data points are determined from the mean of several measurements using different buffer species at the same pH. For example, the pH 6 data averages rupture probabilities conducted in both Bis-TRIS and MES buffer to ensure that the increased rupture probability is not due to the interaction of MES or Bis-TRIS molecules with the membrane. The giant vesicles therefore exhibit an increased affinity to rupture at low pH values independent of the choice of buffer used. The different buffer species used at a given pH are given in table 4.1; at least two buffer molecules apply to each pH value assessed. Importantly, all buffers listed in table 4.1 are made up to an equivalent ionic strength of 150 mM. The result cannot therefore be due to anomalous changes in membrane properties due to the charge content of the solution.

Buffer Species	Bis-TRIS	MES	TRIS	HEPES
pH	6,7	6	7,7.5,8,9	7.5,8,9

Table 4.1: Table of experimental conditions used to examine the pH dependence of DOPC giant vesicles rupture probability on partially hydrophilic PDMS supports.

4.2.4   Hydrophilic Supports
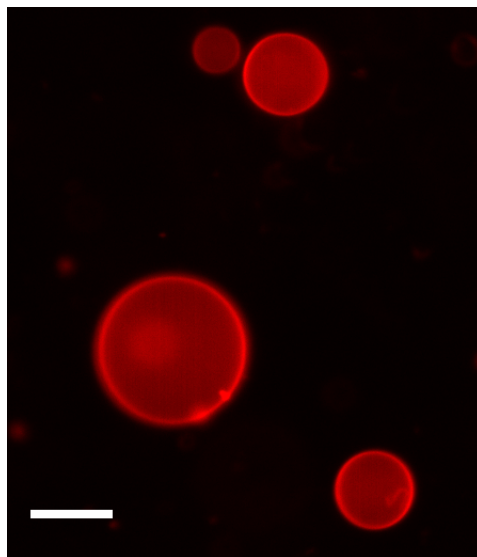
Figure 4.7: GUVs made sessile through a density mismatch between the internal and external contents, in an aqueous environment of 0 ionic strength, do not rupture on hydrophilic PDMS. Scale bar 25μm

If the oxidation time is increased to 15 s or more the support becomes fully hydrophilic. Importantly, mismatching the densities of the internal contents of the GUV and the external medium, under isoosmotic conditions, is still insufficient to promote GUV rupture and fusion (figure 4.7). Instead the vesicles simply sink to the PDMS surface due to their lack of buoyancy. The mere contact of the GUV with the hydrophilic surface is not enough to promote fusion and the ionic strength of the medium must be increased. The exact value of this threshold ionic strength is not investigated here.
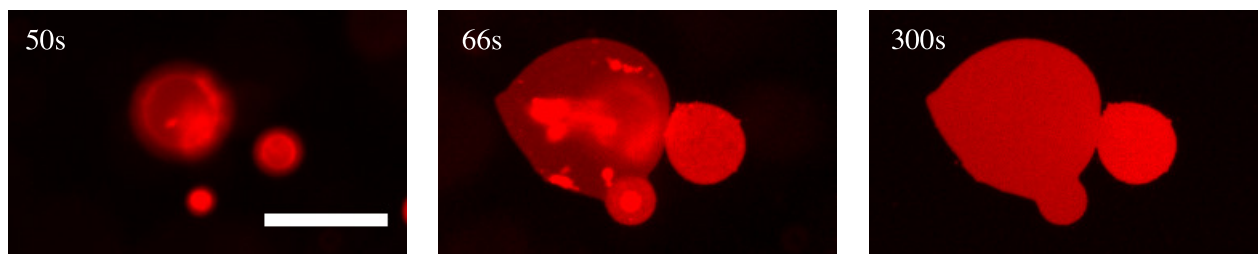
Figure 4.8: GUV rupture events on hydrophilic PDMS . Scale bar 50 mum.

Additionally on the fully hydrophilic support the probability of GUV rupture becomes pH independent, at least for the range of pH values studied (6-9). Instead

the predominant factor governing the vesicle-substrate interaction in this case appears to be the substrate hydrophilicity and the adhesion energy W_{ad}. An example of a GUV rupture event is shown in figure 4.8. Again, not all vesicles rupture at the same time as can be seen by comparing the left and right images; the vesicle rupture appears to be stochastic. Importantly, at the end of the observation, the patch carries little to no additional material on its surface. It would appear that the lipid is forced to maximise the area of membrane in contact with the hydrophilic support.

4.2.5   FRAP

For reasons already stated, the current confocal set-up is not calibrated to measure accurately the diffusion coefficient of supported lipid membranes using FRAP. However it is instructive to compare relative values of diffusivity as long as the protocol is the same for each sample. Table 4.2 contains the diffusion coefficient extracted by fitting the fluorescence recovery profile to equation 4.1. This analysis was adapted from the protocol outlined in reference [78].

$$I(t) = a_0 + a_1 \left(1 - \sqrt{\frac{25}{25 + 4\pi Dt}} \right) \tag{4.1}$$

Within experimental error it is clear that there is little statistical difference between the diffusion coefficients obtained across the full pH range studied and across the two classes of substrate, namely the hydrophilic and partially hydrophilic substrates.

Substrate	pH6	pH7	pH8
partially hydrophilic	0.24 ± 0.01	0.26 ± 0.01	0.23 ± 0.01
hydrophilic	0.24 ± 0.03	0.31 ± 0.02	0.27 ± 0.05

Table 4.2: FRAP diffusivity in $\mu m^2 s^{-1}$ of supported lipid bilayers in buffers of different pHs and on PDMS substrates of different hydrophilicity.

Figure 4.9 shows the before and after bleaching images of several continuous

bilayers formed in buffers of differing pH, thus indicating that a fluid membrane can be formed across the full pH range under study. The diffuse edge of the bleach spot in figures 4.9a, 4.9c and 4.9e immediately shows us that the bleaching period is comparable to the characteristic diffusion time of the lipids in the membrane.

Recovery of fluorescence intensity in the bleach zone is used to distinguish between a supported vesicle layer and a continuous supported lipid bilayer as a diffusion coefficient of zero is still meaningful.
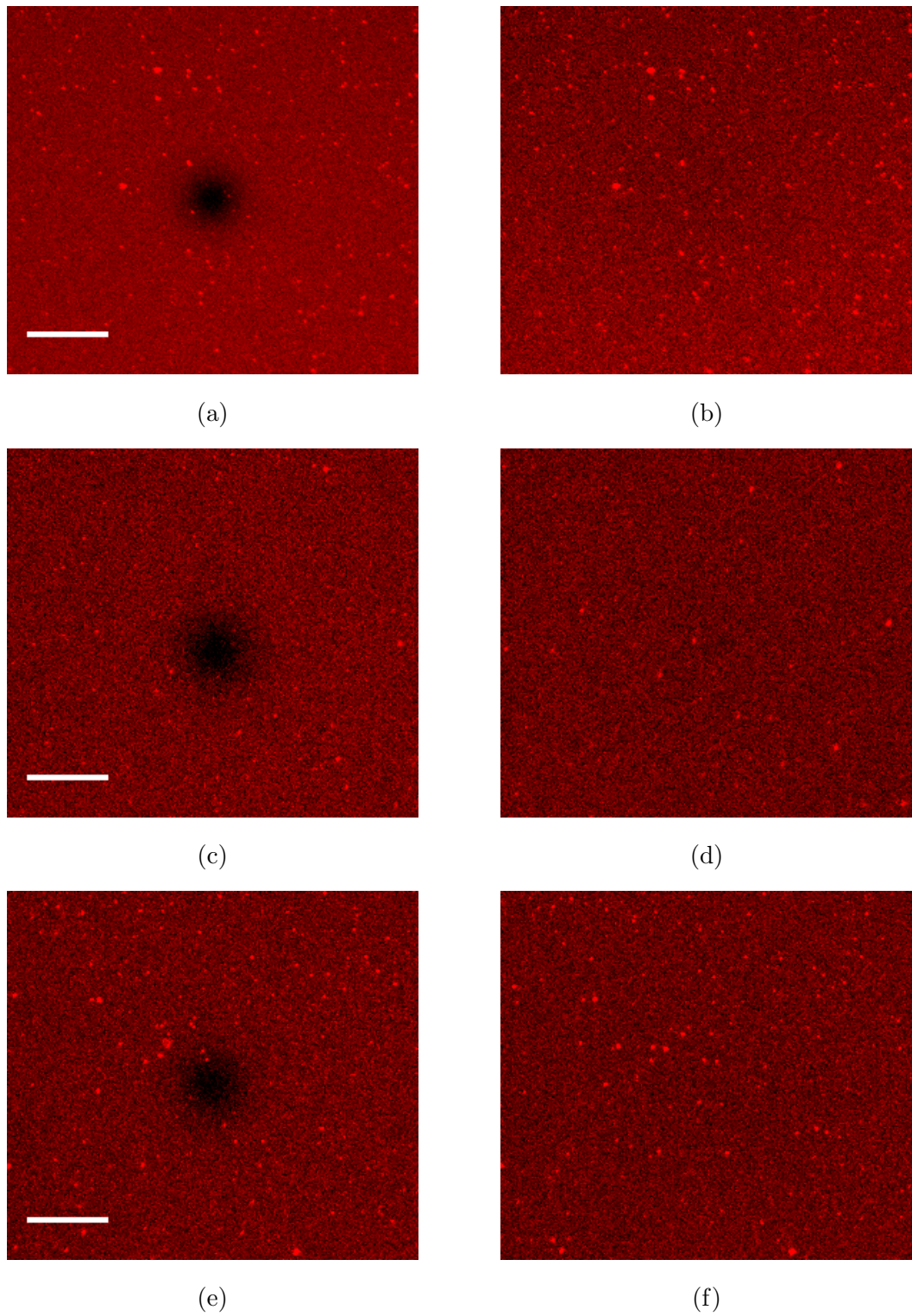
Figure 4.9: Continuous lipid bilayers recover fluorescence intensity after photobleaching. Fluorescence micrographs of a PDMS supported lipid bilayers immediately after photobleaching and 240 s after bleaching when formed at (a,b) pH 6, (c,d) pH 7 and (e,f) pH 8. Scale bars 25 μm.

4.2.6   Zeta Potential Measurements
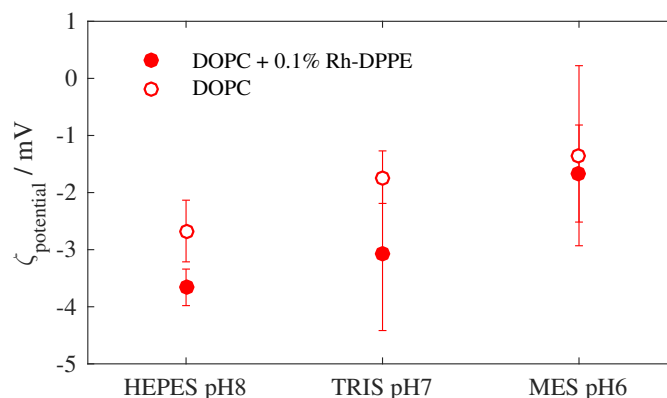
Figure 4.10: Zeta potential of DOPC vesicles in 150 mM NaCl as a function of solution pH. Data is included for DOPC SUVs both with and without 0.1 mol% Rh-DPPE fluorophore. Data points represent the average across 3 independent measurements with error bars denoting the range of values obtained. All zeta potential data is extracted from SUV samples for which the size distribution peaks around 200 ± 50 nm.

Given the pH dependence of GUV rupture probability, it is reasonable to assume that electrostatics are playing an important role in the vesicle substrate interaction. For this reason, it makes sense to measure the potential at the surface of the vesicles as a function of pH. The exact surface charge of a fluid interface is difficult to determine but a closely related parameter, known as the zeta potential can be determined by subjecting vesicle solutions to an oscillatory electric field. The majority of experiments reported herein are carried out using DOPC bilayers. DOPC molecules are zwitterionic, and carry no net charge. As a consequence the electrostatic pressure, described by equation 2.10 is zero. However, measurements of the zeta potential at the surface of DOPC vesicles (figure 4.10) demonstrate that a modest negative potential, and therefore charge, still surrounds the vesicles. The finite charge is rationalised by a model in which the lipid head group rotates according to the solution conditions [105]. This orientation causes a build-up of counterions at the vesicle surface and hence results in the non-zero zeta-potential. In any case, evaluating the Debye length, equation 2.11, for a 150 mM NaCl saline solution, gives a value of approximately 1 nm. Thus, any electrostatic interaction is quickly screened with

distance away from the bilayer.

Zeta potentials of 200 nm DOPC vesicles were determined using a Malvern®Zetasizer Nano apparatus.

4.3   Discussion

4.3.1   Monolayer Formation on Native PDMS

Increased understanding of the pathway from vesicles to supported lipid bilayer *via* spontaneous vesicle fusion is essential if one wishes to control the deposition of the bilayer on the substrate [103]Understanding the importance of the bilayer-substrate interaction is imperative to this aim. The results reported here demonstrate that the substrate hydrophilicity is key, and that the interaction of the vesicle with the support is dependent on the experimental conditions. GUVs provide unique mechanistic insights in this regard because the bilayer formation process can be directly imaged with microscopy. For instance GUVs can be made to sink to the bottom of the imaging chamber using a density mismatch between the internal and external contents of the vesicle. The membrane will hence come into contact with the substrate. Regardless of plasma treatment time, in low ionic strength buffers, the vesicles are stable at the substrate surface, therefore the mere proximity of the membrane to the substrate is not enough to promote vesicle fusion. On the other hand, if the ionic strength of the buffer is increased from 0 to 150 mM then the rupture probability becomes dependent on substrate properties.

Monolayer formation on native PDMS is unsurprising (figure 4.2b). The hydrophobic force is known to be long ranged, extremely strong [44] and to be pivotal in membrane disruptive processes such as fusion and adhesion [106]. The observation of GUVs bursting to form monolayer patches, together with the number of fluorescent aggregates in suspension immediately after vesicle rupture tells us that the native hydrophobicity of PDMS has dramatic consequences for the integrity of membranes. It is therefore obvious that unmodified hydrophobic PDMS cannot be used as a substrate for cells, or indeed in biomedical devices without some form of surface modification [24].

4.3.2   Supported Vesicle Layers

On PDMS exposed to plasma for very short times, strong repulsive interactions are suffcient to prevent the full rupture and spreading of vesicles. Instead sessile vesicle layers form from both SUVs and GUVs. The PDMS in this case may be compared to glass surfaces decorated with a hydrophobic self assembled monolayer of dodecane [58] for which GUVs can be immobilised at the substrate surface. Vesicles, immobilised at the substrate, provide an important, yet understudied, means of probing intermediate states in the pathway to membrane fusion, hemifusion and the mechanics of vesicles.

The presence of multiple contact zones seen within a single GUV in figure 4.4 warrants further discussion. In section 3.3.2, the distribution of advancing and receding contact angles on partially hydrophilic PDMS is given. There is substantial contact angle hysteresis for all values of oxidation time less than 5 s. From this, it can be inferred that the partially oxidised PDMS presents some degree of spatial inhomogeneity with respect to surface energy. This helps rationalise the observation of multiple contact zones in figure 4.4 because the membrane-substrate adhesion energy, W_{ad}, varies locally. The vesicle-substrate interaction thus varies across the cross-section of the vesicle in contact with the support. The contact zones themselves are interesting; the decreased fluorescence intensity suggests that there may be lipid monolayer in the region of close contact between the vesicle and the substrate. However, this configuration would require the existence of a junction between monolayer and bilayer, which constitutes an extreme membrane distortion unlikely to be stable.

4.3.3   Hydrophilic PDMS

Partially Hydrophilic PDMS

On the partially hydrophilic substrate, the GUV rupture probability can be modulated with the pH of the external buffer, in line with experiments reporting successful bilayer formation on titanium and aluminium oxide supports. These oxides have a surface charge that varies discretely with pH, with a near zero surface charge when the pH is neutral. Vesicles display an increased probability of fusion
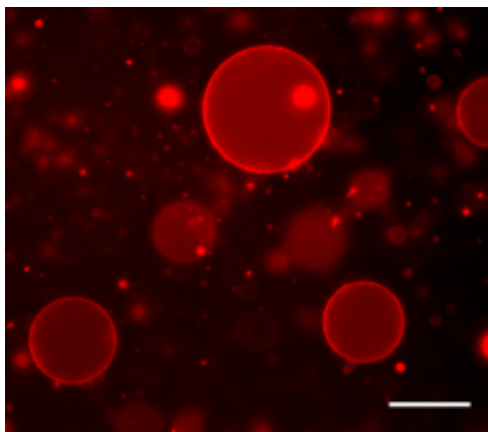
Figure 4.11: Vesicles containing 10 mol % charged lipid, 1,2-dioleoyl-sn-glycero-3-phospho-L-serine (DOPS), in contact with hydrophilic PDMS in a 150 mM ionic strength buffer. Scale bar 50 μm.

at low pH, whereas a stable vesicle layer forms at high pH [93]. Oxidised PDMS is analogous to silica, and therefore its surface charge and degree of surface hydration can be controlled with the pH of the external medium [93, 94]. From this, it should be possible to tune the vesicle substrate interaction. At low pH the PDMS surface is electrically neutral because the high concentration of protons in solution which forces protons to recombine with the surface. In comparison, at high pH, protons can dissociate from the PDMS surface with a low probability of recombination, thus rendering the surface negatively charged. Due to this modulation of the surface charge density, it is thought that the buffer pH can be used to encourage complete bilayer wetting in otherwise unfavourable conditions. Plasma oxidation decorates the PDMS surface with ionisable silanol groups; it may be assumed that increased plasma exposure time increases the density of these ionisable groups and therefore the surface charge. Figure 4.10 shows that zwitterionic DOPC vesicles carry a modest negative surface charge, even in 150 mM NaCl, and the silanol groups on the oxidised PDMS surface will give the surface a negative potential when wetted. Thus, the interaction between the vesicle surface and the PDMS involves the close approach of two negative surfaces, presumably creating a strong EDL repulsion that must be overcome prior to rupture and spreading [95]. In line with these observations, doping the DOPC vesicles with 10% mol negatively charged DOPS is sufficient to completely inhibit GUV adhesion and rupture on hydrophilic PDMS

(figure 4.11). Also consistent with these observations is that incorporating 10% mol positively charged 1,2-dioleoyl-3-trimethylammonium-propane (DOTAP) into the membrane leads to GUV fusion under all pH and oxidation conditions studied other than native, hydrophobic PDMS.

A variation in EDL repulsion force with pH is an enticing explanation; perhaps the increased proton concentration screens the interaction of the two negative surfaces at low pH. It is difficult to pin the change in GUV rupture probability entirely on electrostatics however because the vesicle zeta potentials reported in figure 4.10 are modest and vary only minimally with pH. How then to explain the increased likelihood of GUV rupture on partially hydrophilic PDMS as low pH values?

Alternatively, the increased rupture probability could be due to a decrease in the hydration repulsion experienced by an approaching vesicle to the PDMS at lower pH. Water molecules order differently next to charged or uncharged surfaces [107] and this ordered or disordered water could have significant impact on the hydration repulsion experienced by an incoming vesicle.

Finally, it is also plausible that the pH could change the strength of cohesive interactions between the lipids within the vesicle membrane. A decrease in lipid cohesion at low pH would decrease the energy barrier to GUV rupture and therefore promote fusion. However, only modest changes in membrane mechanical parameters have been reported as a function of pH in the literature [61, 108, 109]. In addition, a change in lipid cohesive interactions would likely change the diffusivity of individual lipids within the bilayer plane, with increased lipid cohesion creating an effectively more viscous medium in which each lipid diffuses [110]. Fluidity of the membrane is confirmed but not the diffusivity values, therefore the effects of pH on membrane cohesion remain unknown.

Hydrophilic PDMS

A density mismatch between the internal and external contents of the GUV using sucrose and glucose is never sufficient to generate GUV rupture, even on hydrophilic PDMS (figure 4.7). Although the exact value of this threshold of ionic strength has not been investigated here, this result is in line with the studies by Anderson [89] and Cremer [95], both of which used AFM to identify an increase in bilayer coverage

on silica substrates as the ionic strength of the buffer was increased. The threshold value of the ionic strength necessary to promote full GUV fusion is not assessed here; instead the ionic strength is fixed at 150 mM as described in section 3.2.4.

On hydrophilic PDMS GUVs rupture with a probability of almost unity in a buffer of 150 mM ionic strength. Individual rupture events are stochastic and the GUVs come into contact with the surface for varying amounts of time before rupturing. From this one can conclude that a thermally activated energy barrier must be crossed as part of the rupture pathway [10]; the supported vesicle is in some way metastable. The fact that the pH dependence of vesicle rupture probability is lost now that the oxidation time is increased also tells us that the substrate properties are the overriding factor in determining the success of bilayer formation *via* GUV fusion. The tuning of the GUV rupture probability is only possible on the partially hydrophilic substrate where the vesicle-substrate interaction is on the cusp of being sufficient enough to promote vesicle rupture and spreading.

4.3.4   The Shape of the Membrane Patches Formed

The shape of the patch formed after GUV rupture is almost never perfectly circular and this is surprising because the circle is the two dimensional shape that minimises the length of the patch perimeter for a given membrane area. The membrane edge represents an extreme curvature distortion to the bilayer as the lipids have to pack unfavourably to prevent exposure of the hydrophobic core of the bilayer to water. The rupture event itself is violent and happens during a time period that is inaccessible to the minimum microscope frame time; lipid is literally thrown across the substrate. Indeed, in some rupture events, macroscopic pores are visible in the membrane patch immediately after rupture suggesting that the membrane spreading is sufficient to overcome the substantial energy barrier to membrane poration [10]. It is entirely possible that during this spreading, the membrane is stretched to an area per lipid greater than the equilibrium area per lipid in a freely suspended GUV. This non-circular shape of this tense lipid patch could then be stabilised by a static friction force acting between the membrane and the substrate [111], which prevents relaxation to a circular perimeter.

4.4   Conclusions and Summary

Several important conclusions can be drawn from the work presented in this chapter, which documents the procedure of bilayer formation *via* the spontaneous fusion and spreading of giant and small vesicles. These findings are important precursors to the work that follows, involving the biaxial stretch of lipid membranes coupled to the PDMS device described in section 3.3.

Firstly, regardless of PDMS substrate hydrophilicity, a high ionic strength buffer is necessary to generate sufficient interaction between the membrane and the substrate for successful bilayer fusion. A simple lack of buoyancy that promotes contact between the vesicles and the substrate is not enough to generate rupture and spreading.

Secondly, the PDMS surface cannot be used in its native form. PDMS is a hydrophobic polymer and if vesicles are placed in a high ionic strength medium and left to interact with hydrophobic PDMS monolayer patches form. The PDMS therefore requires some plasma treatment prior to bilayer deposition.

Thirdly, if the oxidation time is extremely short then the interaction between the membrane and the substrate is insufficient to form a supported membrane but the vesicles adhere to the surface, sometimes distorting the GUV and forming optically resolvable contact zones (figure 4.4). This leads to the formation of a stable vesicle layer that does not recover fluorescence after photobleaching (figure 4.3).

If the oxidation time is increased marginally then the substrate becomes partially hydrophilic and the rupture probability of GUVs can be tuned with the pH of the buffer. The GUVs exhibit a higher probability to rupture in low pH environments demonstrating that the fusion process can be controlled by simply adjusting the pH. The pH might therefore prove useful in research efforts that require the coupling of membranes to other types of partially hydrophilic substrate. FRAP recovery was used to demonstrate the long range diffusivity of the membrane across the pH range studied and to distinguish between a successful bilayer deposition and the formation of a stable vesicle layer.

Finally if the oxidation time is increased beyond 5 s then the GUV rupture probability becomes independent of the buffer pH, but still requires that the buffer has sufficient ionic strength.

Using GUVs provides a simple experimental framework for studying the key players in the bilayer formation process *via* spontaneous fusion. Here only DOPC membranes are studied, with the exception of the addition of a small fraction of DOPS to assess the sign of the substrate charge. The complete pathway from vesicle to bilayer requires that the membrane is deformed substantially. It is therefore likely that the rupture probability will depend strongly on the mechanical properties of the vesicle, such as the elastic modulus. It would therefore be interesting to extend these observations with GUVs formed from lipids with longer acyl chains, to increase the degree of lipid cohesion.

In subsequent chapters, the dynamic properties of the membrane-substrate coupling are explored.

Chapter 5

Membrane Tubes on Partially Hydrophilic Supports

5.1 Overview

When the surface of the device is partially hydrophilic, a lipid patch can alleviate the stress imposed by changes in support area by mechanically remodelling. The area of the patch in contact with the support is strongly coupled to the area of the substrate and changes to the substrate area drive changes in the shape of the membrane. Lipid is absorbed during substrate expansion and projected above the plane of the patch during substrate compression. The shape of the membrane protrusions undergo a complex transition from spherical caps to tubes during the experiment.

5.1.1 Substrate Expansion

Prior to substrate deformation, supported patches always exhibit spherical protrusions, examples of which are shown in figure 5.1a. Spherical protrusions are highly fluorescent circular structures visible on top of the patch. These spherical protrusions are not removed by washing the chamber with fresh buffer, even if the system is agitated vigorously. The caps are therefore strongly coupled to the portion of the membrane that is bound to the planar support. Indeed, if the camera acquisition settings are adjusted properly it is common to see the connection point between the cap and the surrounding planar membrane. Figure 5.2a shows a par-

(a)   (b)
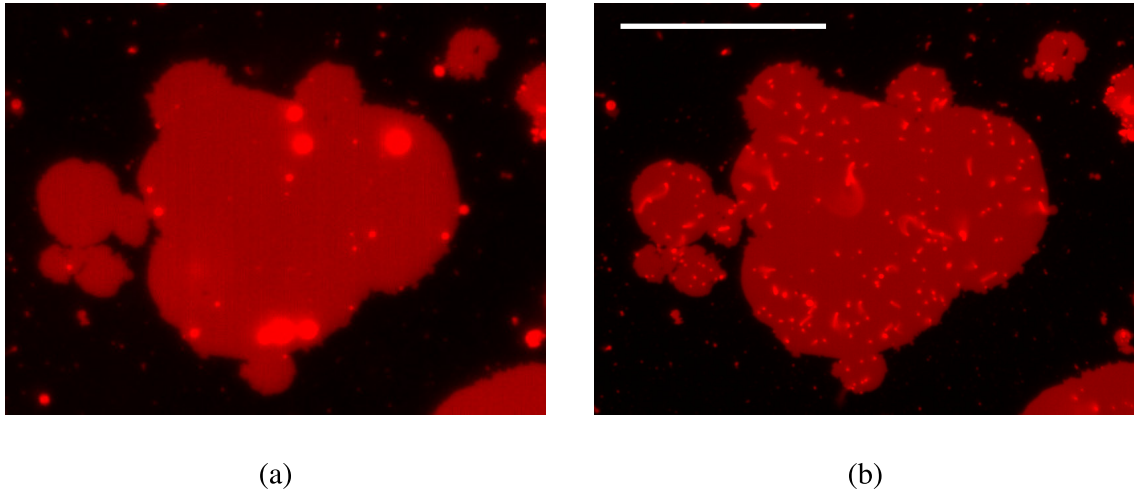
Figure 5.1: DOPC lipid protrusions on partially hydrophilic supports. (a) Prior to substrate deformation the patch supports numerous spherical protrusions. (b) After deformation tubular projections are clearly visible. Scale bar 50 μm.

ticularly clear example. The spherical protrusion has an almost circular region of decreased fluorescence in its centre. This is an example of what is perceived as a membrane neck, which is shown in cross-section by the cartoon in figure 5.2b. This is entirely different to the contact zones of a GUV coming into contact with a hydrophobic PDMS substrate (figure 4.4), where the decrease in fluorescence is due to the contact between the membrane and the PDMS surface. In figure 5.2a the membrane neck has substantially lower fluorescence compared to the surrounding vesicle because only a single fluorescent membrane is seen from the microscope point of view.

As the substrate area is increased, the volume of the spherical protrusion around the neck decreases, but the dark circle within the protrusion persists. The volume decrease continues until complete absorption and at this point the membrane becomes fully planar. The spherical protrusions behave as reservoirs of membrane as the substrate area is increased. As the protrusions are absorbed there is an increase in the amount of membrane in the substrate plane. This allows the patch to offset the increased substrate area and avoid the accumulation of energetically costly membrane tension, section 2.2.

(a)

increasing ε_{sub}

(b)
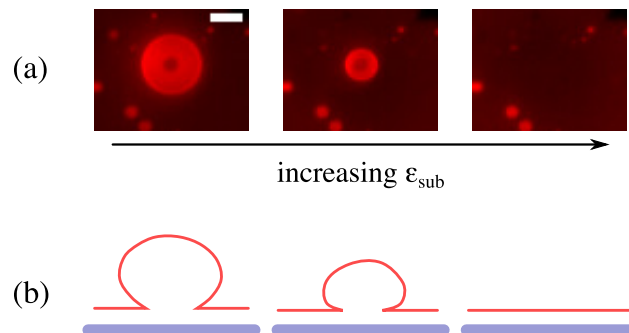
Figure 5.2: Absorption of protrusions during substrate expansion a.) Fluorescence images of a spherical cap, with a visible neck, that is absorbed during substrate expansion. Scale bar $10 \, \mu$m. b.) Illustrative cross-section of the absorption event captured in (a).
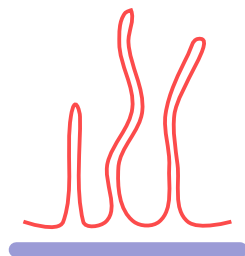
Figure 5.3: Schematic illustration of membrane tubes, shown here in cross-section.

5.1.2 Substrate Compression

When the PDMS is compressed back to its original dimension, the additional lipid in the membrane, due to the absorption of lipid during substrate expansion, must be displaced to avoid an energetically unfavourable increase in lipid areal density, i.e. an increase in membrane tension. This excess of lipid is projected out of the plane of the patch in the form of lipid tubes. A very small portion of the membrane in contact with the support unbinds from the substrate and lipid flows, by convection, toward this unbinding site forming a cylindrical tube which is capped at one end; tubes are shown in figure 5.1b and schematically in figure 5.3. Because the tubes are thin they move diffusively above the plane of the patch, making estimates of the mean tube length and spatial distribution complicated. The projected tube area in the microscope field of view fluctuates wildly during observation. During substrate compression, not all tubes nucleate at the same time or achieve the same length. Rather, additional tubes can nucleate concomitant with the increase in

length of nearby tubes.

Further application of substrate stretch and de-stretch leads to the repeated absorption and projection of lipid tubes. Tubes are retracted when the substrate area is increased and tubes are expelled when the substrate is compressed.

5.2   Results and Analysis

5.2.1   Analysis Framework

A protocol for the analysis of fluorescence images needs to be introduced. A distinction must be made between the lipid that resides in the substrate plane and any lipid area that belongs to a spherical or tubular projection.

| (a) | (b) | (c) |
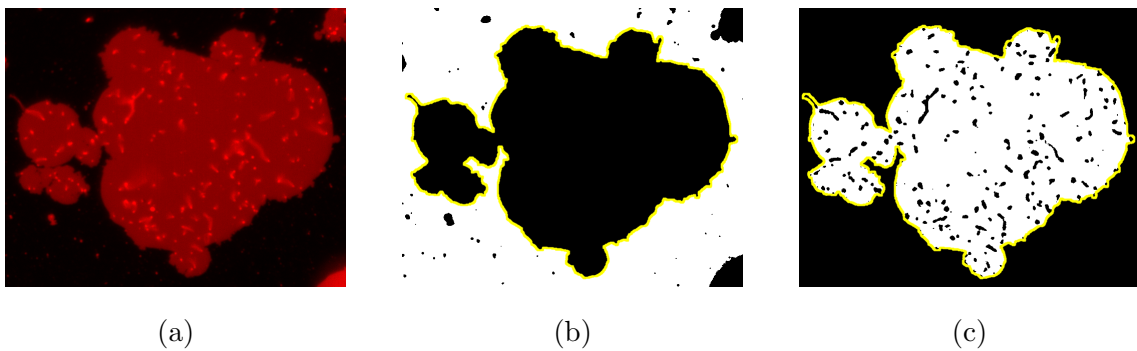
Figure 5.4: Example image constructions used to quantify the membrane behaviour. (a) Original fluorescence image. (b) Binary image of the lipid in contact with the support. (c) Binary image of projected lipid tubes.

Since the membrane projections are comprised of two fluorescent membranes very close to one another, their intensity is statistically higher than the membrane that is flat and in close proximity to the support. Careful application of a dual value threshold, where both low and high pixel intensities are set to zero, enables the measurement of the area of the membrane that lies parallel to the support. An example binary image is shown in figure 5.4b which identifies, in black, what will be referred to as the patch area. For reference, the original fluorescence micrograph is shown in figure 5.4a. For the analysis that follows the membrane strain is defined by equation 5.1. This quantity does not include the protruding lipid as the patch area is generated from the number of pixels contained within the patch perimeter,

indicated by the yellow line in figure 5.4b. The membrane strain is effectively the change in patch area normalised by the initial patch area.

$$\epsilon_{mem} = \frac{A_{patch}(t)}{A_{patch}(0)} - 1 \tag{5.1}$$

An estimate of the amount of protruding lipid can be generated by further adjusting the threshold to identify only statistically high values of pixel intensity that reside within the patch area. Figure 5.4c shows an example binary image where the small black features, within the white patch area, represent the measured projection area. Through appropriate normalisation, the dynamics of membrane remodelling can be followed.

5.2.2 The Dynamics of Membrane Remodelling

The ratio of patch strain to the substrate strain over the course of substrate stretch and de-stretch cycles is plotted in figure 5.5a. The ratio of patch area to substrate area is very close to unity throughout the deformation; in other words the membrane area closely follows the substrate deformation. The data points in figure 5.5a are averaged over the full working range of substrate strain rates available to the device; thus the result is independent of strain rate. For every unit increase in substrate area there is a unit increase in patch area.

The absorption of spherical caps during substrate expansion does not occur linearly with increasing substrate area. Instead, the absorption occurs during substrate expansion from $\epsilon_{sub} = 0 - 8\%$ in a set of discrete steps (figure 5.5b). This behaviour is explained by the distribution in size of the spherical protrusions. When a large cap is absorbed a concomitant large change in normalised protrusion area is measured. In contrast, the increase in tubular projection area as the substrate area decreases is more linear, a reflection of the fact that the tubes have a narrower size distribution in comparison to the caps.

Finally, figure 5.5c reports the stability of the tubes at fixed substrate area. In the experiment the substrate is expanded and compressed to form tubes and then held $\epsilon_{sub} = 0$ for the duration of the experiment. The normalised projection area is calculated by dividing the projection area by the value in the first frame. Regression of the data to a constant value of unity yields a χ^2 statistic equal to 0.8, which is good

(a)

(b)

(c)
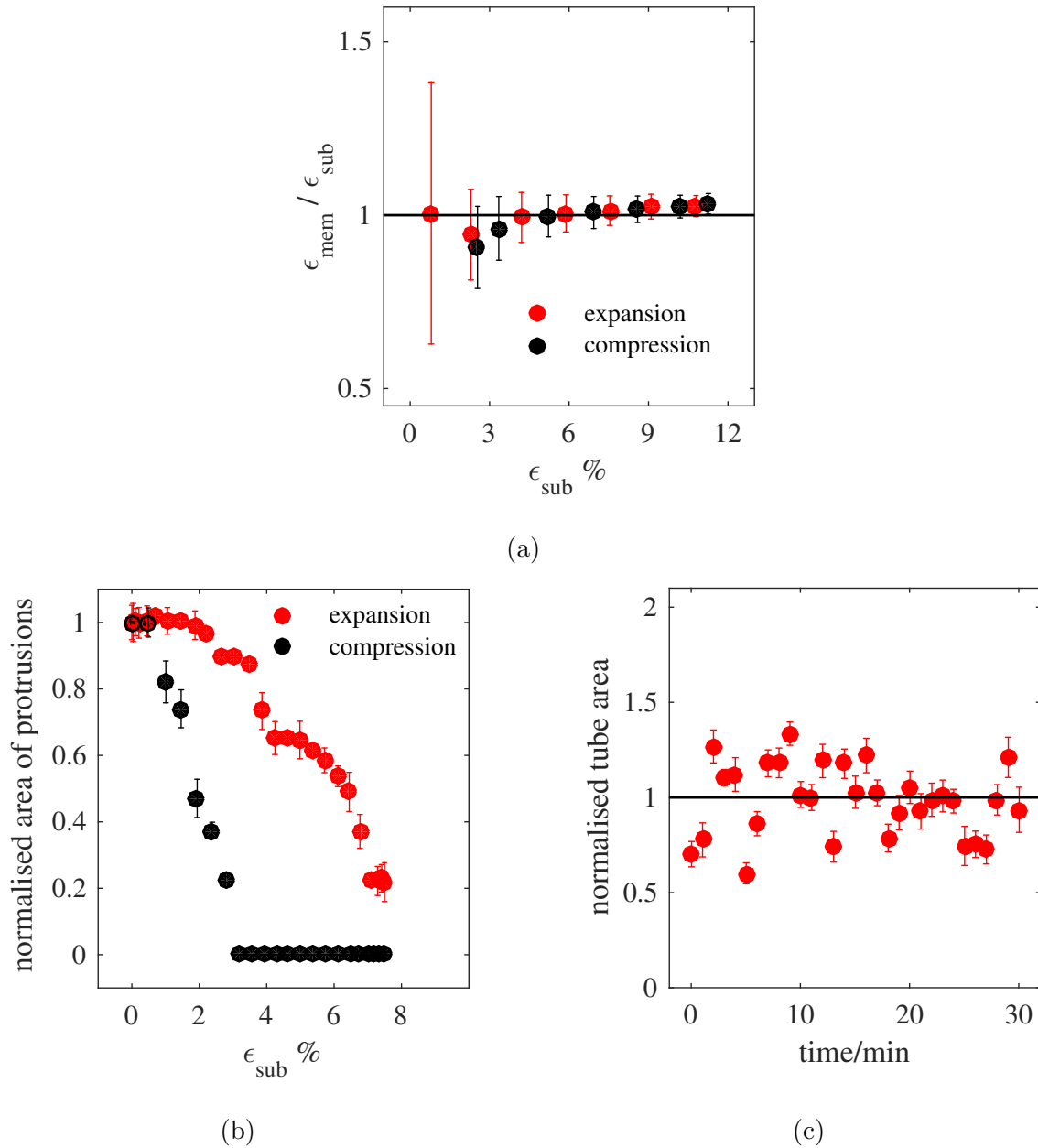
Figure 5.5: (a) Ratio of the membrane strain, ϵ_{mem}, over substrate strain, ϵ_{sub}, as a function of substrate strain for complete substrate stretch and de-stretch cycles. Data points represent the average of measurements obtained across 5 independent samples and the error bars indicate the spread of this value about the mean. (b) Protrusion area as function of substrate strain. Data points correspond to observations from a single representative experiment. Error bars are estimated from the likelihood of correct area segmentation (c) Tubular protrusion area as a function of time for an experiment in which the substrate area is held constant at $\epsilon_{sub} = 0$.

evidence that the tubes are stable on timescales comparable to typical experiments. The large scatter present in the data can be attributed to the Brownian motion of the tubes, which causes large deviations in the projected protrusion area during the image acquisition.

5.2.3   Large Substrate Deformations

So far, only modest substrate deformations of the supported patch system have been considered. It is possible to continue the substrate expansion above and beyond the point at which the patch exhausts all available lipid from the initially spherical protrusions. Continual substrate stretch leads to membrane rupture and pore formation (figure 5.6). The threshold substrate deformation above which further expansion leads to the formation of holes in the membrane is typically around $\epsilon_{sub} \approx 10\%$ for supported patch systems.

| (a) | (b) | (c) |
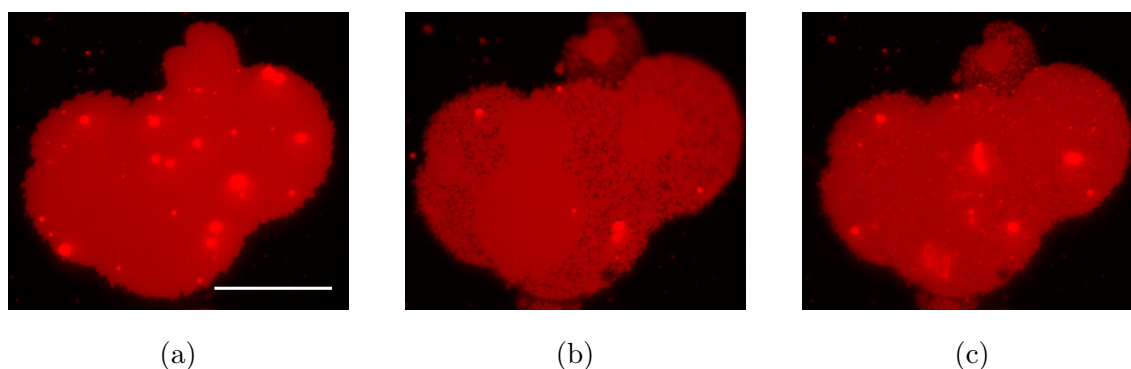
Figure 5.6: Large amplitude deformations lead to the formation of small pores in the membrane. (a) $\epsilon_{sub} = 0$, scale bar 50 μm. (b) $\epsilon_{sub} = 12\%$ (c) $\epsilon_{sub} = 0$.

Protrusion and pore area, normalised by the patch area, are plotted in figure 5.7a. Analysis of the protrusion and pore area within the confines of the patch reveals that there is a gap of approximately $\epsilon_{sub} = 2\%$ between the exhaustion of lipid material and the emergence of pores. This delay is consistent with the 2% area dilation that GUVs can sustain, *via* micropipette aspiration prior to lysis [32, 36].

The formation of pores in the membrane, does not compromise the ability of the patch to form tubes on compression, even if some holes in the membrane do not reseal (figure 5.6c). Consistent with this observation is the hindered FRAP recovery of patches on an expanded substrate. An example FRAP recovery curve is
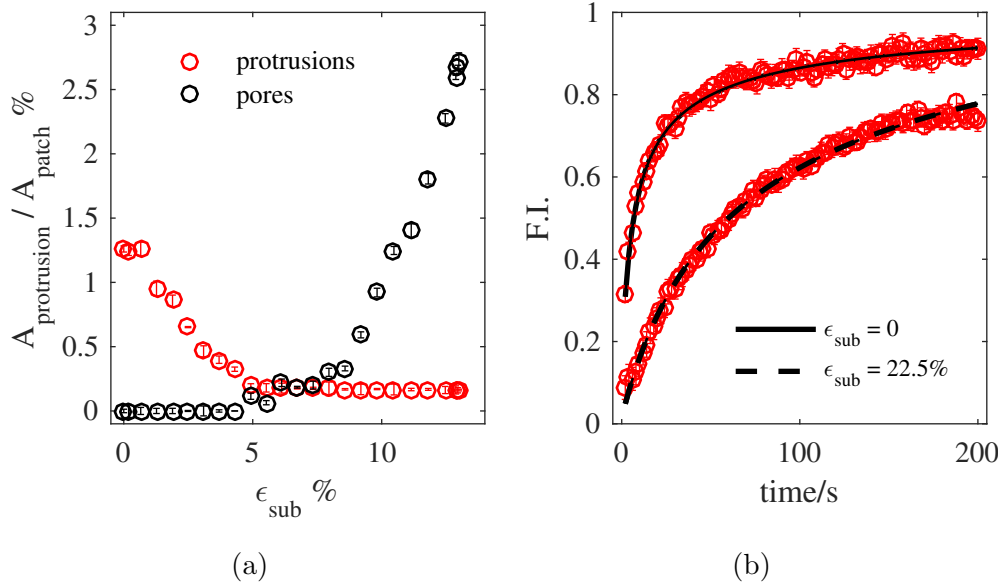
Figure 5.7: (a) Area of spherical projections and area of pores, as a percentage of the patch area during substrate expansion. (b) FRAP recovery curve of a patch, at $\epsilon_{sub} = 0$ and $\epsilon_{sub} = 12.5\%$. Diffusion coefficients of $0.28\ \mu\mathrm{m}^2\mathrm{s}^{-1}$ and $0.06\ \mu\mathrm{m}^2\mathrm{s}^{-1}$ respectively.

given in figure 5.7b for a patch at $\epsilon_{sub} = 0$ and $\epsilon_{sub} = 12.5\%$. The FRAP recovery is slower by a factor of approximately five and also less complete in the expanded state, in line with the notion that individual lipids must diffuse around any holes in the membrane in order for the bleach spot to recover fluorescence intensity.

5.3 Discussion

5.3.1 Insight Gained From Studying the Isolated Lipid Patch System

Mechanical remodelling of the supported lipid membranes has been studied previously [54, 112] using SUVs to form a continuous lipid bilayer. In this system the bilayer covers an area in the mm^2 – cm^2 range. In the publication by Staykova *et al.*, it was argued that the lateral confinement of the membrane plays a pivotal role in the observed mechanical remodelling of the lipid membrane. In contrast, in the supported lipid patch system discussed in this thesis the membrane area is not arbitrated by the substrate area; instead the confines of the patch can be completely imaged. Membrane protrusion absorption and projection in the supported patch system therefore offers new insight into the mechanical remodelling of substrate supported membranes by removing the requirement of lateral confinement of the membrane.

Here a 1:1 mapping between the planar patch area and the normalised substrate area during substrate area expansion or contraction is reported. This coupling between the membrane area and substrate area on partially hydrophilic supports indicates that lipid cannot collectively flow over the substrate in response to substrate area dilation. For every unit area of substrate increase there must be a unit area increase in the membrane coupled to the surface. High static friction must exist between the membrane and the substrate that resists flow. This friction is determined by the adhesive strength with which the membrane adheres to the substrate [44], suggesting that, despite the PDMS being only partially hydrophilic, the value of W_{ad} for the contact potential between the bilayer and the substrate is large enough to drive the membrane through the observed shape transformations.

5.3.2 Spatial Variation of the Adhesion Energy on the Partially Hydrophilic PDMS Substrate

Both the heterogeneous distribution of membrane tubes across the patch and the contact angle hysteresis reported in section 3.3.2 suggest that the membrane-

substrate adhesive energy varies with spatial position on the substrate.

The expected distribution of tubes from a substrate of uniform membrane-substrate adhesion is difficult to predict. What is the expected mean length of the tubes or the mean separation between the sites of tube nucleation? Surely if flow was permitted everywhere then all the lipid would flow towards a single tube to avoid an increase in free energy due to further loss of membrane area in contact with the substrate? The experimental data tells us that the tubes do not all nucleate at the same value of substrate compression and that they do not all grow to the same length. This tells us that the flow of lipid across the substrate, towards the tube, is not isotropic. Immediately from this observation it may be deduced that the substrate must organise membrane flow towards sites where tube nucleation is easiest.

Similarly, it is not the case that all the spherical protrusions coupled to the patch are absorbed at the same value of ϵ_{sub}. Rather it is the case that once a threshold membrane distortion, or stretch, is obtained the protrusion is absorbed continuously by the expanding planar membrane. This suggests that the absorption of a cap is an activated process requiring external mechanical triggering and that local tension gradients can exist with finite lifetime within the patch. In other words, the absorption of a single cap does not relax tension in the entire membrane patch; instead the effects are felt over a finite distance from the absorption event. A maximum distance over which an absorption event can be felt must be a consequence of hindered or organised lipid flow across the substrate.

The degree of spatial heterogeneity in adhesion energy has been directly assessed through experiment in our laboratory [113]. An AFM tip was functionalised with hexanethiol to render the tip hydrophobic and the force required to pull the tip from a partially hydrophilic PDMS substrate was recorded as a function of spatial position. The retraction force and hence the strength of the adhesive interaction, W_{ad}, was found to exhibit significant heterogeneity. In an analogous way, the membrane must feel a surface potential that binds the membrane with varying degrees of strength. This distribution in adhesion strength might also explain the strong friction observed between the membrane and the substrate. The areas of high membrane-substrate affinity act as discrete pinning points that prevent the large

scale collective redistribution, or flow, of lipid.

5.3.3 The Energetics of Lipid Protrusion Projection and Absorption

Consider for a moment the implications of what must occur for a membrane to unbind from a substrate and form a tubular projection. This transformation requires that the work of adhesion between the membrane and the substrate to be overcome as well as an energetic cost due to the high curvature of the structure formed [114]. This must be balanced by the alleviation of membrane tension caused by the projection of membrane area. Recall from section 2.2 that bilayers have a large elastic modulus in the plane of the membrane but a small resistance to bending. Clearly, for the partially hydrophilic PDMS the bilayer-substrate adhesion energy is, at least locally, of an order of magnitude similar to that of the membrane bending energy in order to support spherical and tubular projections.

Tubes and caps are highly curved membrane structures and can only exist if a portion of membrane becomes unbound from the substrate. The protruded state is therefore has a higher free energy in comparison to the planar configuration. The membrane could, conceivably, relax to the planar state by sliding over the substrate and allowing all of the membrane to couple to the surface. The combination of tube long-term stability and the 1:1 mapping of the patch area to substrate area suggest that the friction at the patch edge is enough to arrest such relaxation processes. The membrane is in some way confined to the area of the patch perimeter on top of the support.

The delay in the onset of protrusion absorption until the substrate is stretched by approximately $\epsilon_{sub} = 2\%$ also tells us that the protrusions do not spontaneously adsorb and that the membrane accumulates tension for a brief period during substrate deformation, prior to absorption. This value of 2% is again similar to the values of vesicle lysis tension observed for GUV systems using micropipette aspiration [32, 36]. This observation supports the hypothesis that protrusion absorption is an activated process that requires external impetus. Elastic energy must be stored in the membrane to kick the patch out of the metastable projection state and into the lower energy, planar configuration. Further evidence of this interpretation comes

from the observed hysteresis in projection area when comparing substrate expansion to compression. The membrane temporarily moves up an elastic energy potential well, before relaxing by absorbing or projecting material.

5.3.4   The Formation of Membrane Pores at High Substrate Strains

The formation of membrane pores upon extreme distortion does not yield a homogeneous spatial distribution of membrane pores. The pores seem to open preferentially in certain regions of the patch. This observation is difficult to rationalise but is perhaps related to the GUV rupture process. In section 4.1 the pathway for successful supported bilayer formation *via* spontaneous vesicle fusion is seen to require first that vesicles approach the surface, then adhere and finally rupture and spread. This procedure is mirrored by rupturing GUVs according to the results of sections 4.2.3 and 4.2.4. GUVs approach the surface, bind, deform and subsequently rupture. For the case of partially hydrophilic supports, the incoming GUV is squashed into the surface by the adhesive forces acting between the vesicle and the substrate. Indeed, if the substrate is too hydrophobic then the GUV may not rupture but instead form adhesion zones in contact with the substrate (figure 4.4). In figure 5.6b, the pores within the membrane are located preferentially at the periphery of the patch. Is it not too much to argue that the regions of intact membrane are commensurate with the regions of initial contact between the vesicle and the surface, in other words the adhesion zones of figure 4.4?

The remainder of the membrane patch is formed from the spreading of lipid over the surface. A membrane propagating over a support of low surface energy proceeds *via* a different spreading mechanism compared to completely hydrophilic supports (section 2.3.1). In particular, the dominant mode of dissipation for spreading on partially hydrophilic supports, comes from inter-leaflet shear, as the proximal leaflet is pinned to the substrate [49, 56]. The distribution of pores therefore alludes to the existence of two distinct subpopulations of supported lipid within the same continuous membrane, a possibility that has recently been confirmed by MD simulations [115].

Despite the formation of pores in the membrane at high substrate strain, membrane patches do recover their fluorescence intensity after photobleaching in both

the stressed, $\epsilon_{sub} = 12.5\%$, and the unstressed state, $\epsilon_{sub} = 0$. The presence of the holes or defects in the membrane must then obstruct as opposed to inhibit lipid flow.

5.3.5 The Preferred Protrusion Shape

Next I want to present an argument based on energetics to rationalise the most stable conformation of the membrane protrusions. On partially hydrophilic supports the patches always have some protruding membrane in the form of spherical caps, prior to substrate deformation. Most of these structures have a visible membrane neck but not always. In the absence of a neck, the fusion of the cap to the planar membrane would require the fusion of two adjacent membranes. The topological pathway to successful fusion of two adjacent membranes requires that both membranes form pores.

$$\Delta E_{pore} \approx \pi^3 \frac{\kappa_A^2}{\lambda H^2} \tag{5.2}$$

Specifically for a membrane fusion event, the energetic barrier is given by equation 5.2, where H is the distance between the two fusing membranes [116], λ is the line tension of a membrane pore, which is a function of membrane tension and κ_A is the membrane elasticity modulus. Making use of a typical value for membrane tension of 0.02 mNm^{-1} [9], together with a bending modulus of 20 $k_B T$ [117] and an inter-membrane separation similar to typical intracellular distances 30 nm gives an energy barrier to membrane fusion of 3×10^3 $k_B T$. This estimate is enormous and will not be crossed on any experimentally accessible timescale, according to the Boltzmann distribution, $P_{fusion} \sim \exp(\frac{-\Delta E_{pore}}{k_B T})$.

The formation of a spherical cap in the membrane, on the other hand, requires only that a stable membrane neck exists. Of course there is an energy penalty associated with the maintenance of a membrane neck due to its curvature. The theory of domain budding in compositionally heterogeneous vesicles tells us that a stable membrane neck requires a line tension at the rim [118]. For the case of a supported membrane, the friction between the membrane and the substrate may provide this line tension. It is unclear how exactly the hydrodynamic friction, in this experimental system, may replace domain line tension but insights may be obtained

from MD simulations, which provide estimates of the bending energy of membrane neck structures. Kozlovsky *et al.* found that this neck energy does not appreciably deviate from zero for a neck radius of greater than approximately 30 nm [119], well below the resolution of conventional microscopes. As a consequence, the energy penalty associated with maintaining a membrane neck is substantially less than the energy barrier to the fusion of two adjacent membranes. The spherical caps present on the patch prior to deformation are most likely to form a junction, in the form of a membrane neck, with the planar portion of the bilayer, as opposed to separate compartmentalised vesicles that fuse to the membrane during substrate expansion.

a.)

b.)
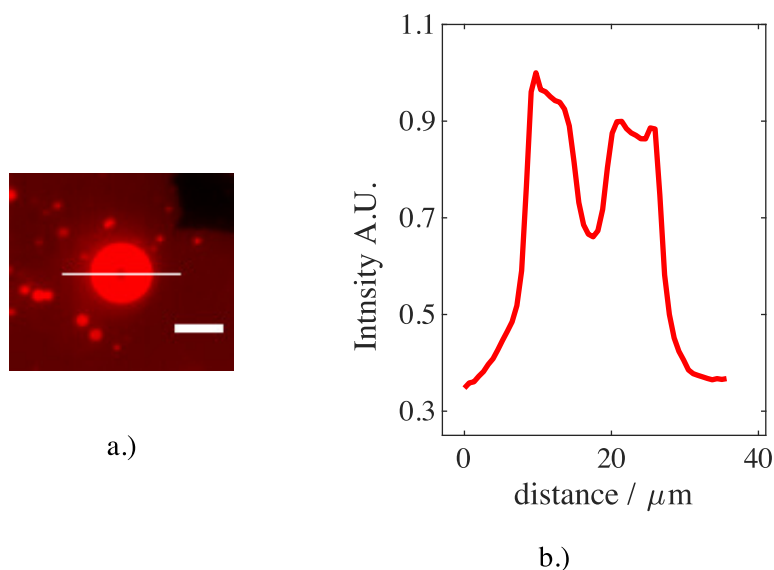
Figure 5.8: a.) Fluorescence micrograph of the spherical cap in figure 5.2. White line indicates the origin of the fluorescence intensity values adjacent. Scale bar = 15 μm. b.) Normalised fluorescence intensity values extracted from a.).

The hypothesis of the spherical caps forming a neck at the junction between the protrusion and the substrate supported lipid also agrees with the fluorescence intensity values in figure 5.2. The fluorescence intensity in the bright region surrounding the protrusion neck is approximately three times the value of the supported lipid membrane outside the protrusion volume, indicating that three fluorescent bilayers all stack laterally when viewed from the microscope perspective in this region; this can be seen clearly in figure 5.8.

The initially spherical additional membrane material on top of the patch cannot be recovered through repeated substrate stress cycles. The shape transformation

from spherical protrusion to membrane tube therefore warrants further discussion. A previous study presents a unified picture of the possible shape transformations of lipid projections [54, 112] in which a full mathematical description of the departure from the planar state of the membrane is derived. The key components of the model are the interplay between the thickness of the interstitial water layer between the bilayer and the substrate, the coupling of the density of lipid in each leaflet to the bending and stretching modes of deformation, and the bilayer-substrate interaction potential. An understanding emerges in which the supported bilayer is able to relieve the accumulated tension and mechanical pressure difference across the membrane by projecting curved lipid structures [120]. At comparative compressive strain, the system adopts different protrusion configurations according to the volume of the water layer trapped between the bilayer and the substrate. As the thickness of the water layer increases the most energetically favourable protrusion mode transitions from thin tubes, to shallow membrane buds through to spherical caps. This transformation from thin tube to spherical cap, with increasing trapped volume, is due to the spherical projection holding more volume than the tube for a given surface area of membrane that must unbind from the substrate.

The thickness of the interstitial water layer in the continuous lipid system can be adjusted by an imbalance in the concentration of membrane impermeable solutes above and below the bilayer. If the concentration of solutes above the bilayer is less than that below then water is osmotically driven into the interstitial hydration layer, increasing the water layer thickness. As a consequence, the membrane shape transformations can be reconstructed extremely well by controlled experimental modulation of the concentration of osmolytes above the bilayer [54]. However, the supported lipid patch system under study here is subtly different to the continuous lipid film. This is because of the existence of the edge at the perimeter of the membrane patch. This edge presumably allows the interstitial water volume to relax. The protrusions for the lipid patch system are hence trapped in the low interstitial volume regime; in other words, membrane tubes.

Tubes are also the preferred protrusion geometry for membranes with non-zero spontaneous curvature. According to Lipowsky [114] it is possible to draw an analogy between substrate induced membrane mechanical tension and macromolecule

induced membrane spontaneous curvature. Exposure to curved macromolecules, such as BAR proteins, forces membranes to adopt curved configurations. Differing concentrations of such molecules on either side of the membrane creates a system free energy that is minimised by a structure with intrinsic curvature. This spontaneous curvature is identical to a spontaneous tension. A membrane adhered to a planar support in the presence of non-zero membrane tension can therefore reduce free energy by uncoupling from the support and buckling. The membrane must adopt a protruded shape that matches the induced spontaneous curvature. This leads naturally to two possible protrusion modes: spherical caps and membrane tubes. Numerically evaluating the energies of the protruded states, tubes or buds, with respect to the planar state reveals that the budded membrane state, in the absence of a conserved volume condition, is energetically unfavourable. In other words, the adoption of the spherical curvature structure does not sufficiently relieve membrane tension to justify the loss in free energy due to the unbinding from the substrate. The membrane tube on the other hand, if one neglects the small energetic penalty associated with the membrane curvature at the end of the tube, represents a downward pathway in system free energy.

Two complimentary arguments exist, therefore, for the supported patch system preferring the membrane tube as the most stable protrusion mode.

5.4   Conclusions

In this chapter it has been shown that if the PDMS device is partially hydrophilic then supported lipid patches can alleviate the stress imposed by substrate expansion and compression by absorbing and projecting lipid from the plane of the support. The shape of the protrusions undergoes a complex morphological transition from spherical caps to tubes during the first cycle of substrate stress.

The patch area, parallel to the support, is strongly coupled to the substrate area. For every unit of substrate expansion the patch area increases by one unit. It is this change in area of the patch that drives the membrane through the observed shape changes.

Once formed, the tubular lipid protrusions are stable if the substrate area is held

fixed at $\epsilon_{sub} = 0$ for lengths of time comparable to a typical substrate deformation.

Finally, if the substrate deformation is increased such that the patch exhausts the supply of additional lipid for adsorption, the patch is forced to open small membrane defects or pores to accommodate the substrate area decrease. This is consistent with previous reports of free membranes being incapable of withstanding absolute area dilations much in excess of 2%.

This discussion of the results suggests that the partially hydrophilic substrate is a surface that has locally varying adhesion energy. The local variation in membrane-substrate adhesive strength seems capable of orchestrating the mechanical remodelling of soft lipid membranes. The shapes adopted by the membrane provide a passive means of area regulation for the patch, completely devoid of any metabolic input. Considering the enormous complexity and magnitude of membrane distortions in life processes such as cell division [121], or the constriction of red-blood cells in microcirculation [4], it is important that cells have readily and rapidly available stores of membrane to buffer sudden membrane area changes [9]. The results here show that if the interaction between the membrane and the support is appropriately heterogeneous, a curved membrane structure may be adopted and maintained without the input of external work. Indeed, the projection of membrane tubes has been realised experimentally in live cells when single cells are adhered to an elastic substrate [122], indicating that cells may utilise the specific nature of the interaction of the plasma membrane with the cytoskeletal or extracellular support to great effect.

In addition, the results reconcile well with accepted models of the modes of bilayer propagation over supports of different surface energy. Bilayer coverage is an important area of research in the development of new lipid based antifouling coatings [21, 123] and stimuli responsive encapsulation [124]. Knowledge derived from these experiments may assist in future designs for these kinds of technologies. It is clear that the substrate properties have significant impact on the membrane behaviour and its response to substrate area change.

Chapter 6

Membrane Sliding on Hydrophilic Supports

6.1   Overview and Description of the Behaviour

Motivated by the complexity of the supported membrane remodelling on partially hydrophilic supports, it is a natural question to ask how the membrane will behave when the substrate hydrophilicity is increased. To address this question, and to better understand the importance of substrate properties in the behaviour of supported lipid membranes, the oxidation time is now increased to 30 s, making the surface fully hydrophilic. In this regime the contact angle of a water droplet on the PDMS surface is close to zero (section 3.3.2).

The membrane response on hydrophilic supports turns out to be very different. Instead of recruiting lipid from protrusions the membrane accommodates substrate stress by decoupling from the substrate and slipping over the PDMS surface; this motion of the membrane relative to the substrate will be referred to as membrane sliding. When sliding, the membrane preserves its area and integrity by simply allowing the substrate to expand underneath it, creating relative motion between the bilayer and the surface.

For nominal strain rates of between $0.010 - 0.030 \ \%\mathrm{s}^{-1}$ the membrane first undergoes a modest expansion in tandem with the support. These types of experiments and strain rates can be performed over periods ranging from five minutes to half an hour. As the substrate strain is increased further the sliding motion begins and

(a)   (b)
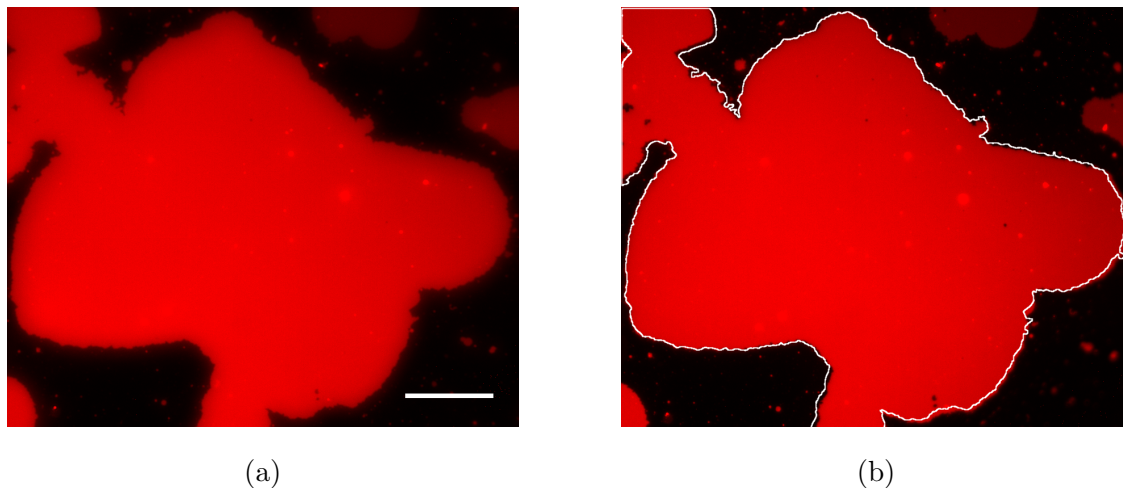
Figure 6.1: Fluorescence micrographs of the membrane patch at i.) $\epsilon_{sub} = 0$ (a) and ii.) $\epsilon_{sub} = 7.5\%$ (b). The white contour in (b) indicates the original membrane perimeter in (a). Scale bar 50 μm.

the substrate expands independently without driving further expansion of the membrane. As a consequence of the increasing substrate area, the space between patches on the substrate surface increases whilst the patches themselves try to maintain the same area. Upon compression, this behaviour is reversed and the lipid patches are initially compressed by the shrinking substrate up to a critical compressive strain, beyond which further membrane area change is resisted and substrate continues to deform without stressing the bilayer. An example lipid patch, exhibiting the sliding behaviour, is shown at $\epsilon_{sub} = 0$ and $\epsilon_{sub} = 7.5\%$ in figures 6.1a and 6.1b respectively. The white contour in 6.1b is provided to assist comparing the initial and final areas of the patch after the deformation. It is clear that the membrane has largely remained intact despite the substrate deformation.

As well as preserving area by slipping relative to the expanding support, the patch is able to recruit lipid from the periphery in order to relax the stress accumulated within the interior. This behaviour results in a change in the perimeter of the patch and the flow of membrane from one region to another is well illustrated by the micrographs of figure 6.2. Comparing the patch perimeter at $\epsilon_{sub} = 0$ (figure 6.2a) and $\epsilon_{sub} = 9.54\%$ (figure 6.2b) in a 'spot the difference' type of exercise reveals that the membrane perimeter has changed substantially. It is also clear that the retracted lipid originates predominantly from the parts of the patch that have a large amount

(a)   (b)

(c)
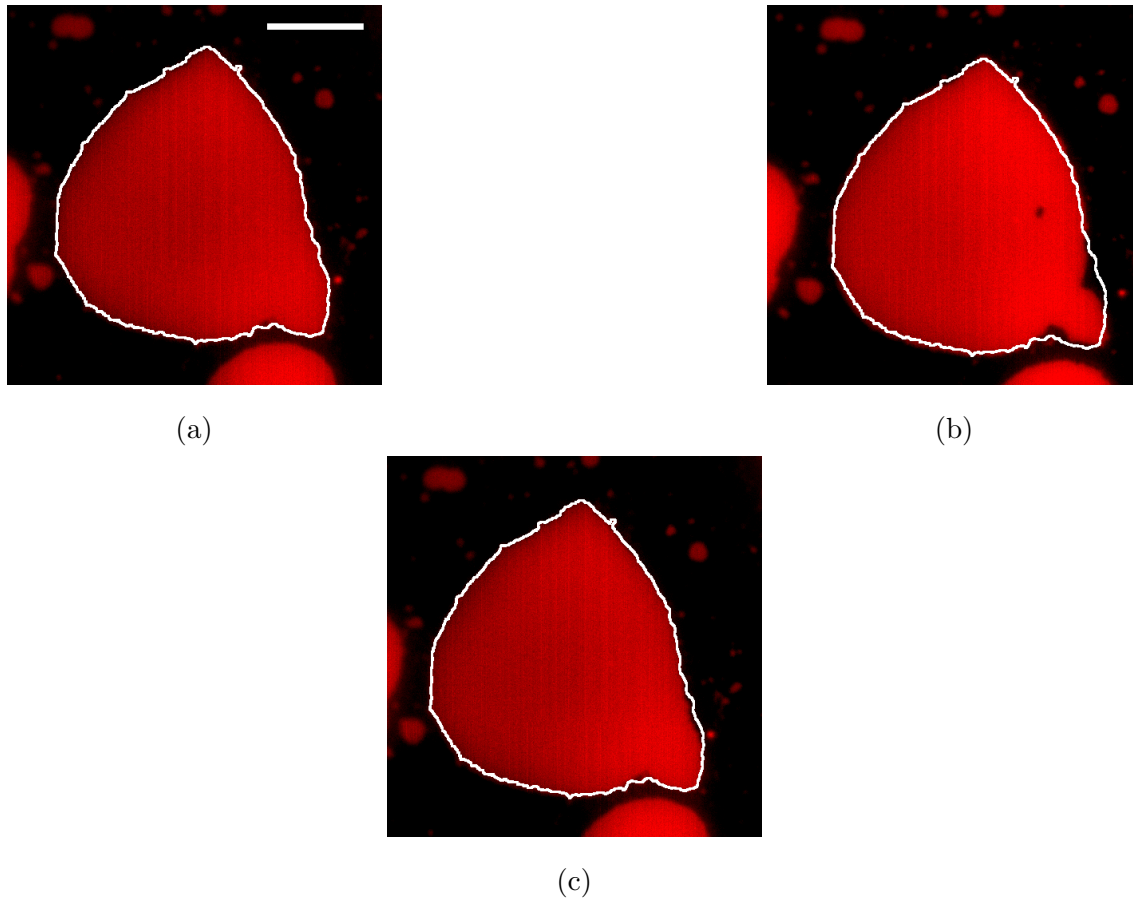
Figure 6.2: The perimeter of the membrane patch changes during substrate strain cycles. Fluorescence micrographs of a patch (a) $\epsilon_{sub} = 0$, (b) $\epsilon_{sub} = 9.54\%$ and (c) $\epsilon_{sub} = 0$ after substrate compression. In (b) and (c) the initial membrane perimeter, from (a), is marked with a white contour to identify the perimeter change. Scale bar = 20 μm.

.

of perimeter compared to internal area. Upon compression, the original membrane perimeter is restored (figure 6.2c).

The observation of a lipid patch sliding over a hydrophilic support is novel. In what follows it will be seen that the exact relation between the membrane and substrate area during sliding is dependent on the substrate strain rate, the history of the deformation and the membrane patch size. Changing the substrate strain rate has profound consequences for the sliding behaviour. Under rapid substrate compression it is found that the membrane accumulates compressive tension that is then relaxed by a slower exponential like growth of the membrane area over the support. The use of membrane patches instead of continuous lipid bilayers, whose

lateral dimensions can span several millimetres, affords this class of experiment unique perspectives on the dynamic nature of the coupling of membranes to the support because the total membrane area can be tracked.

Experiments in which the substrate strain is large tell us that the membrane sliding, cannot indefinitely buffer substrate stress. In all experiments achieving sufficient substrate strain magnitude, pores are observed to form in the membrane. This indicates that the stress that is being transmitted to the bilayer is sufficient enough to overcome the membrane yield strength. In what follows, each of these observations will be quantified in more detail.

6.2   Results and Analysis

6.2.1   Framework for Analysis

To quantify the sliding behaviour one again needs to measure the membrane area in the plane of the support. On partially hydrophilic supports a distinction between planar membrane and lipid protrusion was necessary. This distinction is not necessary for the fully hydrophilic support because the redistribution of lipid is parallel to the surface when sliding. As such one can adjust the meaning of equation 5.1 from the previous chapter. All of the membrane undergoing deformation is contained in the planar portion of the bilayer so A_{patch} becomes $A_{membrane}$, conveniently shortened to A_{mem}. Thus equation 5.1 now becomes equation 6.1.

$$\epsilon_{mem}(t) = \frac{A_{mem}(t) - A_{mem}(0)}{A_{mem}(0)} \tag{6.1}$$

During sliding it is frequently observed that the patch may detach from adjacent lipid patches. Depending on the size of the patches formed, the area may or may not be large enough to be filtered from the background of small lipid patches present in the images. As a consequence the detached lipid may not be picked up by the analysis protocol for frames after the detachment event. This results in a decrease in the measured membrane area as the membrane slides. Figure 6.3b highlights with a red circle a point at which the main lipid patch has detached from an area of lipid that is no longer counted in the analysis. The reverse situation is encountered when the substrate area is decreased. Adjacent lipid islands reconnect with the

(a) (b) (c)
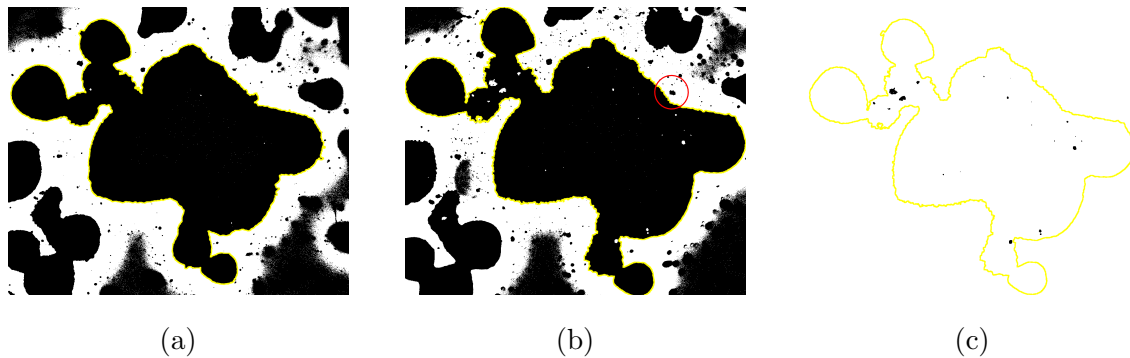
Figure 6.3: Binary version of a lipid patch at a.) $\epsilon_{sub} = 0$, and b.) $\epsilon_{sub} = 7.5\%$, with the measured membrane area outlined in yellow. Red circle highlight a prominent lipid island that becomes separated from the main patch during substrate expansion. c.) Binary image, derived from b.), from which the pore area is estimated.

original patch, resulting in an increase in the total membrane area measured using the analysis protocol.

Additional complications arise from the development of pores in the membrane as the magnitude of the substrate deformation is increased. To account for these pores, the binary stack of images used to measure A_{patch}, is deleted beyond the contour that defines the original patch. In other words, all pixels outside of A_{patch} are set equal to zero in the analysis. The remaining feature area is then assessed again. This gives an estimate of the area of pores within the confines of the patch; an illustration of this procedure is provided in figure 6.3c. In what follows, the membrane area is always defined as the area of the planar portion of the patch with the pore area subtracted, as in equation 6.2 .

$$A_{mem} = A_{patch} - A_{pores} \tag{6.2}$$

6.2.2 Membrane Sliding

Plotting the normalised membrane deformation, ϵ_{mem}, versus the substrate deformation, ϵ_{sub}, yielded information about the membrane substrate coupling in the chapter 5. For this reason the same curve is analysed for the sliding behaviour.

Numerically the membrane versus substrate area curve is complex and requires some explanation (figure 6.4). At modest strain rates, as substrate expansion be-
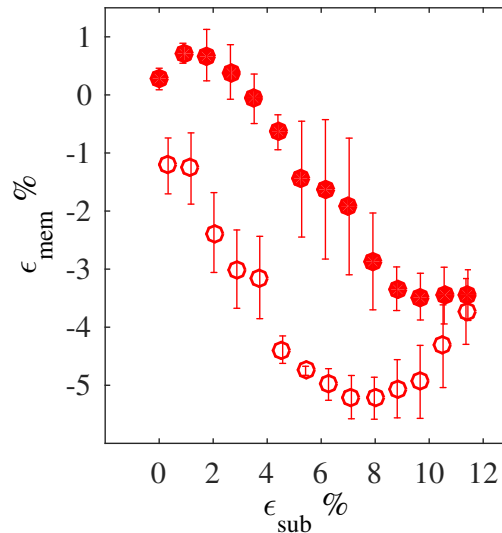
Figure 6.4: Membrane versus substrate strain for a typical patch demonstrating the sliding behaviour. Substrate expansion from $0 - 12\%$ is indicated by the filled red circles and compression from $12 - 0\%$ by the open red circles. Error bars report the range of areas across 3 repeat stresses.

gins, there is a short period during which the membrane area follows the substrate area and expands in unison, illustrated by a positive ϵ_{mem} in figure 6.4. ϵ_{mem} then plateaus up to about $3 - 4\%$ ϵ_{sub}. Further substrate expansion then results in a decrease in membrane area, illustrated by a negative ϵ_{mem} in figure 6.4. This can be partially explained by the detachment of the patch under observation from smaller lipid patches that cannot be detected using the analysis protocol, as described in the section 6.2.1. Notice that in figure 6.4 the magnitude of the change in membrane area is less than 6% whereas the substrate area changes by at least twice this amount. After the decrease in membrane area, the value of ϵ_{sub} flattens again before the cycle of substrate compression begins. The behaviour is now reversed; at first the membrane area decreases with the substrate, causing a negative change in ϵ_{mem} for ϵ_{sub} between $7 - 12\%$. Further substrate compression forces the patch to reconnect with the lipid islands that separate during expansion, driving an increase in ϵ_{mem}. When viewed holistically the curve in figure 6.4 looks like a reoriented elasticity hysteresis loop; the membrane area is larger when the substrate is expanding compared to the same ϵ_{sub} value during compression. This immediately tells us that some form of dissipation is prevalent in the system.

6.2.3   The Total Membrane Area Dilemma

Conservation of lipid during sliding presents a problem. The detachment of the main lipid patch under observation from smaller patches has already been described and contributes to the negative change in ϵ_{mem} observed during substrate expansion. However, when the total area of the patch before and after the complete deformation is compared, i.e. at $\epsilon_{sub} = 0$ after substrate compression, there is a loss in membrane area.

Table 6.1 quantifies the membrane area change, ΔA_{mem}, measured for a sample of patches deformed at a nominal strain rate, over two substrate deformation cycles. Also provided in table 6.1 is the maximum substrate strain value ϵ_{sub}^{max} achieved during the deformation cycle. To reiterate, the quantity ΔA_{mem} is the measured difference in membrane area before and after the substrate deformation cycle, at $\epsilon_{sub} = 0$ in both cases. ϵ_{sub}^{max}, on the other hand, is the maximum value of substrate strain achieved during the deformation and is included to check for correlation of the membrane area loss with the magnitude of the substrate deformation.

Some general remarks concerning the data in table 6.1 can be made. The first is that during the first substrate deformation, there is a significant negative difference between the patch area at the beginning and end of the experiment, despite the substrate returning to its initial area. Across the independent samples a mean membrane area change of -6±1% is observed. Comparing the data of the first and second cycles of substrate stress reveals some subtle differences. The mean loss of patch area decreases to -1.2±0.6% and many of the measured patch area changes, for the second cycle of substrate stress are close to zero. The measured patch area changes provide evidence that some of the lipid is redistributed during the first cycle of substrate deformation, whilst the area is mostly conserved during subsequent deformations. This dependence on deformation history is intriguing and is further evidence of the existence of some viscous dissipation in the system.

6.2.4   Pores in Sliding Patches at Large Substrate Strains

During sliding, the patch is able to preserve area by slipping relative to the substrate and redistributing lipid in order to relax the accumulated stress. A natural question that arises is whether this sliding mechanism allows for the membrane to

1st cycle			2nd cycle		
A_{patch} μm²	$\Delta A_{mem}\%$	$\varepsilon_{mem}^{max}\%$	A_{patch} μm²	$\Delta A_{mem}\%$	$\varepsilon_{mem}^{max}\%$
1207	-2.43	28.1	2450	-0.41	9.5
916*	-10.42	17.7	1260	-0.30	4.2
705*	-4.52	18.3	1160	-1.39	27.2
640	-8.25	19.6	530	-0.75	15.5
590	-7.12	17.0	400	-3.31	18.0
430	-3.70	20.4			
190	-3.41	12.0			

Table 6.1: Table of the patch area change ΔA_{patch} at the beginning and end of first and second substrate strain cycles. All data are reported as percentages. Data points marked with * are obtained from a device that has been taken through an expansion and compression prior to lipid deposition, to exclude substrate artefacts.

mitigate the effects of substrate deformation indefinitely.

Increasing the magnitude of the substrate strain reveals that all sliding patches eventually rupture and form small pores. An example patch demonstrating this behaviour is given by figure 6.5c and a plot of the normalised pore area versus substrate strain is provided by figure 6.5a. Pores do not form upon substrate expansion in figure 6.5a until a strain amplitude of approximately 6% is reached. Beyond this, the gradient of the pore area versus substrate area is shallow, approximately 0.007. Once 14 % substrate area change is achieved the gradient of the curve increases by an order of magnitude, 0.078, and the area of the patch plus the area of the pores begins to increase rapidly with the substrate area. After this point the dominant response becomes additional pore expansion as oppose to sliding; further sliding is inhibited by the expansion of the pores and additional substrate area results only in increasing the sizes and number of pores within the patch.
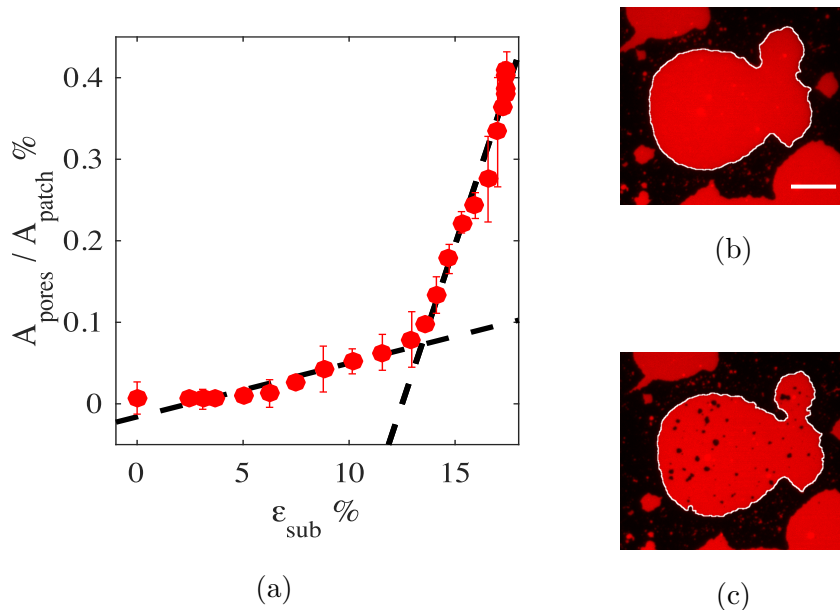
Figure 6.5: Sliding patches eventually form pores at large values of ϵ_{sub}. (a) Pore area, normalised by patch area, versus ϵ_{sub}. (b) & (c) Fluorescence micrographs of the patch prior to and after the onset of visible pore formation respectively. Scale bar = 15 μm.

6.2.5 Rapid Substrate Compressions

The complex stress-strain relation and the dependence of the sliding behaviour on the sample history suggest that there is some dissipation in the system. It is logical to suggest that the behaviour might also be sensitive to substrate strain rate. To test this hypothesis of a rate dependent response to substrate strain, it is possible to subject lipid patches to a very quick substrate compression. The experimental protocol is illustrated in figure 6.6a. The substrate is held at maximum substrate area briefly before the pump pressure is released. This leads to an instantaneous large negative change in the PDMS substrate area. Consequently the membrane is compressed and tension is developed in the membrane. The tension is equilibrated through a characteristic membrane area increase over time at fixed $\epsilon_{sub} = 0$. The growth of the membrane area can be approximated by a single exponential, equation 6.3, and is recorded only after the substrate stops moving such that the measured area change is independent of substrate motion. Figure 6.6b shows a typical membrane area increase with the fit to equation 6.3 superimposed as the solid black line.

$$\Delta A(t) = C * (1 - \exp(-t/\tau)) \tag{6.3}$$

The example shown in figure 6.6b has a relaxation time constant of 64 s. It is, of course, possible to perform the experiment in reverse. One can measure an exponential decrease in the area of the membrane after a rapid substrate expansion. However, this is challenging to reproduce due to instabilities associated with the PDMS surface at maximum ϵ_{sub}, difficulties in achieving good optical focussing, and the formation or pores in the membrane. In general, the model, equation 6.3 is not a good fit to the experimental data, but the model does at least capture the relevant time scale of the observation.
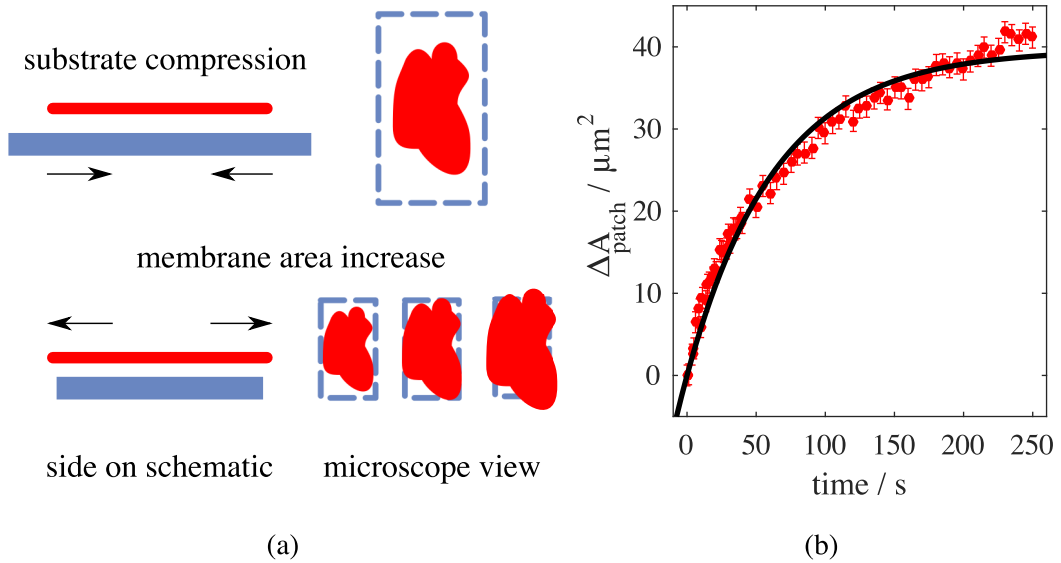
Figure 6.6: Rapid substrate compression generates exponential patch area growth. a.) Illustration of the experimental set-up. Left: the device is held at maximum substrate area before the pump pressure is released. The substrate area then rapidly decreases, during which time the membrane compresses. Right: the microscope camera images the expansion of the membrane across the substrate after cessation of the substrate motion. b.) $\Delta A_{patch} = A_{patch}(t) - A_{patch}(0)$ versus time t. Solid black line indicates the weighted best fit of the data to the function 6.3.

Substrate		Fitting			
$\Delta\varepsilon_{sub}$ %	rate % / s^{-1}	A_{patch} / μm^2	ΔA_{patch} / μm^2	τ/s	χ^2
11.4	0.6	13500	653	63	6.1
11.2	0.6	3970	17	56	0.8
15.1	0.8	3460	58	67	0.6
11.6	0.4	1790	17	71	0.7
19.7	1.1	1170	40	64*	1.74

Table 6.2: Measurements of membrane area relaxation from 5 independent isolated patches. From left to right the columns are respectively the amplitude of the substrate area change, the substrate compression rate, the initial area of the patch, the change in area of the patch, and the measured relaxation constant for the fitting of the data to the model, equation 6.3. Data marked with a * are plotted in figure 6.6b.

6.3   Discussion

6.3.1   Comparing the Sliding Behaviour to the Membrane Protrusion Behaviour

Changing the hydrophilicity of the PDMS is an easy experimental modification that has profound consequences for the response of the bilayer to substrate deformation.

In chapter 5, it was found that the membrane area was strongly coupled to that of the substrate, a behaviour that was demonstrated by the constant ratio of ϵ_{mem} to ϵ_{sub} (figure 5.5a). The increase in surface energy of the PDMS completely changes the behaviour of the bilayer, therefore placing greater significance on the properties of the substrate and how these properties can affect the supported bilayer system [69]. Indeed the support propeties have already been shown to have an influence on membrane fluidity [26], and phase [125]. Here it is found that the support properties also influence the remodelling of membranes in a dynamic supported lipid bilayer system.

On the partially hydrophilic support, a membrane patch can adsorb lipid from spherical protrusions to accommodate increasing substrate area. In comparison, on the fully hydrophilic support, the probability of a membrane patch absorbing extra lipid from surface adhered vesicles is almost zero. In what follows I wish to explain why I believe this is the case.

On hydrophilic PDMS the adhesive interactions between the membrane and the support, W_{ad}, are large and the membrane wants to come into as much contact with the surface as possible. This would destabilise any membrane neck structures (figure 5.2) as the patch can minimise the system free energy by adopting a planar configuration, maximising the area of membrane in contact with the support. As a consequence, any spherical protrusions should be adsorbed into the planar portion of the membrane as the membrane spreads over the substrate surface. Vesicles present on top of the patch must therefore be separate, compartmentalised vesicles. For reasons already discussed, the energy barrier preventing the fusion of a separate lipid vesicle into a supported lipid bilayer is extremely large. This explains why the mechanical remodelling response of the membrane is completely independent of the sliding and pore regime. The out of plane remodelling response is never seen in parallel with the membrane sliding behaviour reported in this chapter because there is no coupled reservoir of additional lipid for absorption.

In addition, the strong coupling of the patch area to substrate area is noticeably absent in the sliding behaviour. The increase in PDMS surface energy has permitted flow of the entire membrane patch, rather than just localised lipid flow towards or away from the point of protrusion nucleation or absorption. To rationalise the change in behaviour one needs to consider the possible effects of the increase in PDMS surface energy on the bilayer support coupling. An increased surface energy of one of a pair of interacting surfaces increases the Hamaker constant, therefore strengthening adhesive interactions [44]. Van der Waals forces are therefore likely to increase. At the same time, a fully hydrophilic surface is better hydrated with a layered water structure that must be displaced [94, 126] upon close approach of the two surfaces.

The equilibrium distance between the bilayer and the substrate represents a trade off between adhesive and repulsive interactions. In this system it is hard

to determine whether or not the increased PDMS surface energy will result in an increase or a decrease in bilayer-substrate separation, or hydration film thickness. This argument has also neglected the importance of electrostatic interactions. Although this could perhaps be dismissed for the partially hydrophilic substrate, the longer duration of plasma treatment for the hydrophilic support will render the surface negatively charged. For hydrophilic silica, which is in many ways analogous to PDMS , electrostatic forces have been identified as important for the adsorption, rupture and spreading of neutral zwitterionic vesicles [89]. Additionally, water molecules have been shown, through experiment [127] and simulation [128, 129, 130] to order differently around hydrophilic and partially hydrophilic surfaces. A change in water structure in the hydration layer and/or a change in water layer thickness will naturally affect the transmission of stress from the substrate to the membrane and could explain the differences in membrane behaviour observed on the partially hydrophilic and hydrophilic supports.

6.3.2   The Static Friction

The transmission of stress from the substrate to the membrane is captured by the plot of ϵ_{sub} versus ϵ_{mem} (figure 6.4) and is intriguing from a rheological point of view. The bilayer strongly resists areal dilation in the plane and resists decoupling from the support through the membrane-substrate adhesion energy W_{ad}. A slipping motion between the membrane and the substrate can only occur *via* shear of the interstitual water layer for membranes on hydrophilic supports [49, 56, 131]. The plot of ϵ_{sub} versus ϵ_{mem}, (figure 6.4), therefore informs on the rheology of the interstitial water film.

The initial expansion of the patch prior to the onset of sliding suggests that the interstitial water layer is behaving much like a Bingham plastic in response to deformation [55]. At first the water refuses to flow, leading to patch expansion, before yielding and allowing the membrane to slip. Static friction must exist between the bilayer and the substrate such that bilayer may be stretched. The friction force, for a substrate-coupled membrane has only contributions from the adhesive energy of the patch. In other words, the friction is adhesion dominated, the second term in equation 2.13, and has no contribution from an external loading pressure. The

friction force should be proportional to the area of the patch if the adhesive energy per unit area is uniform.

Figure 6.7 plots the value of ϵ_{sub} at the onset of the slip of the membrane relative to the substrate as a function of patch area. The data possess significant scatter and there is no obvious linear dependency. It is then either that the range of A_{patch} values studied is too small for the dependence on A_{patch} to develop or that there is complex, and perhaps sample specific, static friction between the membrane and the substrate.
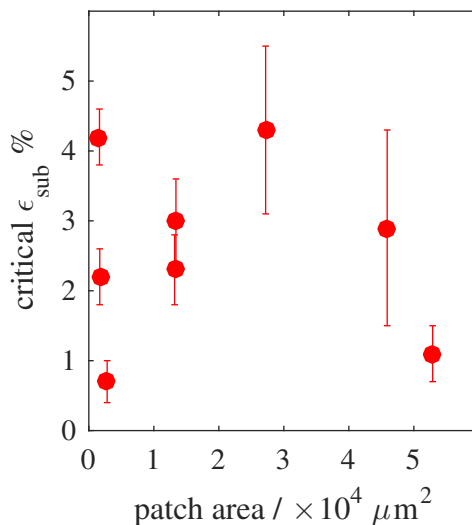
Figure 6.7: Value of ϵ_{sub} at which membrane sliding begins, as a function of patch area A_{patch}, for independent isolated patches deformed at a fixed strain rate of $0.07\ \%\mathrm{s}^{-1}$

.

The existence of static friction also explains the non-circular appearance of the patches, first discussed in chapter 3. One would expect a well lubricated bilayer substrate system to minimise its free energy by relaxing to a circular patch of lipid, to minimise the length of the edge [10, 132]. This is not experimentally realised. It is therefore concluded that the membrane is unable to relax to a circular shape due to the static friction between the bilayer and the substrate.

6.3.3   The Kinetic Friction

There must also be some kinetic or viscous friction that arises once the sliding begins on the basis of the following three remarks. Firstly, from the hysteresis curve

of the ϵ_{mem} versus ϵ_{sub} plot (figure 6.4) some dissipation is inferred. To initiate the sliding of the membrane relative to the substrate, a modest compression or extension of the membrane is necessary. Secondly, the formation of pores in the membrane at high substrate deformations (figure 6.5) can only be explained if some tension is developed in the membrane during sliding. Thirdly, the experiments performed at high substrate strain rates produce an exponential like growth of the membrane area.

These experiments motivate a viscoelastic description of the rheology of the hydration layer separating the bilayer from the substrate. The partial expansion of the patch, illustrated by positive ϵ_{mem} in figure 6.4 up to about $\epsilon_{sub} = 2\%$, is consistent with the notion of a critical yield stress that must be overcome before the relative motion, and hence dissipation, between the bilayer and the surface can occur. If the interstitial water film that lubricates the sliding between the patch and the substrate demonstrates both elastic and viscous behaviour then a dependence on strain rate could be anticipated. Viscoelastic materials possess a characteristic time τ, if stress is applied rapidly in a time less than τ, the system responds like an elastic solid. Conversely, if the stress is applied slowly then the viscoelastic material flows like a liquid [55, 27] (section 2.3).

If this is the case then during rapid substrate deformations the membrane area should be coupled to that of the substrate because the lubricating film is behaving like a rigid solid. The tension accumulated in the membrane should subsequently drive a monotonic increase in membrane area with time until equilibrium is reached. This is backed up by the loosely exponential behaviour of the membrane area versus time, which is consistent with a driving force that is diminishing as the membrane area increases, i.e. the membrane tension.

As the substrate is rapidly compressed, the interstitial film does not yield and the bilayer is compressed, forcing the membrane to store some elastic energy, proportional to the membrane elasticity modulus, κ_A. As the membrane area increases and slides over the PDMS, the water layer is stressed slowly and therefore flows, dissipating the elastic energy stored in the membrane through the viscous friction opposing sliding. This dissipative energy is a function of the ratio of the water film viscosity η over the thickness of the water film between the membrane and the

substrate, h. Comparing the units of these three terms (equation 6.5) allows us to write down a time scale that is at least dimensionally consistent and characteristic of the membrane-substrate system (equation 6.4).

$$\tau \sim \frac{\eta A_{patch}}{h K_A} \tag{6.4}$$

Dimensional consistency check

$$[K_A] = MT^{-2}$$
$$\left[\frac{\eta}{h}\right] = ML^{-2}T^{-1}$$
$$[A_{patch}] = L^2 \tag{6.5}$$

$$\therefore \quad \left[\frac{\eta A_{patch}}{h K_A}\right] = T$$

Equation 6.4 tells about the rate at which a membrane can equilibrate stress when sliding over a thin lubricating film. This parameter should describe a crossover strain rate above which the membrane begins to accumulate elastic energy, or tension, and below which the shear of the interstitial water layer dominates energy dissipation; in other words, the characteristic relaxation time of the supported membrane system.

On the basis of this crossover time, τ one should find that patches are forced to open pores when the substrate stress is applied rapidly. At slow substrate strains the same patch should be able to mitigate the substrate stress by sliding.

This prediction is confirmed in figure 6.8 in which the same large patch is stressed at two different strain rates. When the stress is applied slowly the membrane is able to resist failure (figure 6.8a). In comparison, when the same amplitude deformation is applied rapidly the patch opens large pores (figure 6.8b). This same rate dependence is not reproduced using smaller isolated patches. This is perhaps because the larger patches, for which the total membrane area cannot be imaged, have smaller τ values, by equation 6.4, making the cross-over value inaccessible to the strain rate range of the device.

(a)   (b)

.
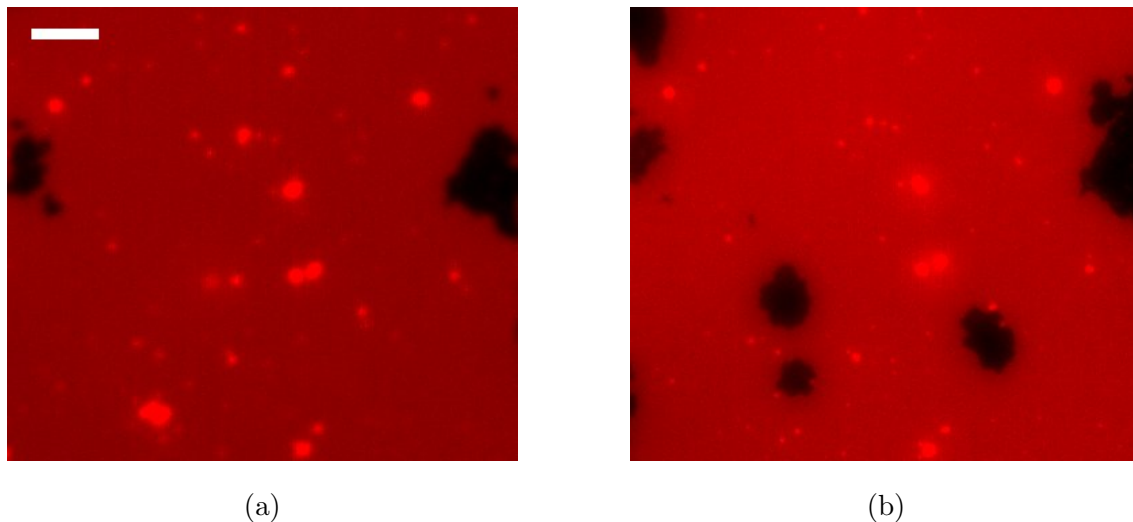
Figure 6.8: Fluorescence micrograph of a large patch stressed slowly at a rate of 0.01 %s^{-1} (a), and rapidly 0.11 %s^{-1}, (b) up to an amplitude of 10 %. Scale bar $50 \text{ } \mu\text{m}$

6.3.4 Distortions to the Membrane Patch during Sliding

The change in perimeter observed during sliding (figure 6.2) is interesting and challenging to explain. The increased oxidation time should have the effect of uniformly decorating the PDMS surface with ionisable silanol groups [133] (see chapter 3 for discussion). The bilayer substrate adhesion energy, W_{ad} should therefore be spatially homogeneous [134]. If this were indeed the case one might expect the lipid patches to slide radially in response to biaxial deformation. This is not observed; instead the patch seems able to recruit lipid from certain regions with relative ease compared to others. This is not easy to explain, but it could be that the regions where the membrane flows most easily are a consequence of the high ratio of membrane edge to internal area in these regions; the large amount of membrane edge generates an instability that makes it easier for these parts of the patch to slide (figure 6.2).

6.3.5 Membrane Area Losses during Membrane Sliding

Finally, before concluding this chapter the membrane area losses during the first cycle of substrate deformation should be remarked upon. Whilst it is impossible to

know what is going on at the nanoscale, an explanation might be drawn from the topography of the PDMS.

PDMS is a polymer, and is likely to exhibit some nanoscale roughness [68] when used as a surface for lipid membranes. It is unclear how the membrane should conform to this topography. The gain in free-energy from closely mapping the topography of the substrate is offset by the energy penalty due to curvature [48, 134]. It is possible that after the yield of the interstitial water layer during sliding, the conformation of the bilayer to the PDMS surface may be different, as both the trapped water and the membrane have been allowed to relax. A bilayer that more closely mimics the topography of the substrate would have a smaller projected area than a membrane patch that spans over the substrate roughness. This situation is exaggerated and conceptually illustrated in the cartoon in figure 6.9.

prior to
deformation

after
deformation
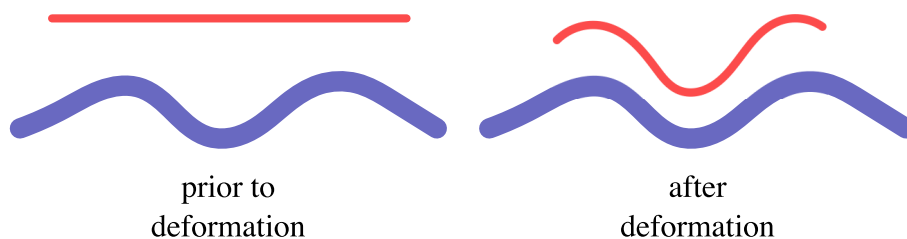
Figure 6.9: Illustrative explanations for the loss of membrane area observed during the sliding behaviour.

The concept of a pre-stretched patch was introduced in chapter 4 and was explained on the basis of the process of vesicle rupture on hydrophilic PDMS. The rupture of vesicles on hydrophilic PDMS is both rapid and violent, indicating a high spreading energy driven by the adhesive interactions between the membrane and the substrate. This could cause the patch to spread to an area that is greater than the optimal area per lipid head group, i.e. creating an elastic tension in the patch. Due to the static friction previously described, this pre-stretched membrane is stabilised. However, during the first cycle of substrate deformation, the sliding motion allows this pre-tension to relax and the lipids obtain a new equilibrium area. This explains the decrease in membrane area observed during the first application of substrate strain but not the second (table 6.1).

Alternatively, the possibility that some lipid is lost to either the solution or the hydrophobic PDMS that lies beneath the oxidised PDMS, during the deformation,

cannot be excluded. However, given that the oxidised PDMS surface is hydrophilic and the entropic penalty for free-lipids in solution is large, this seems unlikely.

6.4 Conclusions

Increasing the surface energy of the PDMS support has dramatic consequences for the method of substrate stress relaxation adopted by the membrane. In this chapter it has been shown that the membrane is able to relax the substrate imposed area dilation by decoupling from the support; the membrane preserves its area by slipping relative to the substrate.

At large substrate strains the sliding motion of the patch eventually becomes insufficient to accommodate the changing substrate area and the membrane is forced to open small pores. These pores become the dominant mode of tension relaxation at high ϵ_{sub} values.

On the hydrophilic substrate the supported membrane system also exhibits strain rate dependent phenomena where rapid substrate compression generates a compressive tension in the membrane that is equilibrated through an exponential like growth of membrane area over the substrate at $\epsilon_{sub} = 0$.

Larger patches exhibit a rate dependent pore size. Slow loading rates allow the membrane to relax tension by sliding, whilst fast loading rates to the same substrate strain magnitude produce pores in the membrane.

The sliding behaviour has been rationalised through careful consideration of the properties of an elastic membrane sliding on a hydration layer separating the bilayer from the substrate. The membrane behaviour might be explained if the system exhibits complex flow properties, including viscoelasticity and flow behaviour analogous to that of Bingham plastic.

Comparing the membrane sliding behaviour presented in this chapter to that of the previous chapter, shows that membranes possess extraordinary capacity to accommodate area changes. Light is also shed on the importance of the interaction of a lipid membrane with supports in determining the dynamic properties of the membrane-substrate system. The sliding of lipid bilayers over hydrophilic surfaces has been studied extensively from the perspectives of bilayer formation [95] and from spontaneous wetting from a lipid reservoir [56] but not, until now, from the point of view of a dynamic substrate. Here, it has been shown that the supported bilayer system presents rich physics including rate dependent dissipation and non-linear rheology.

The lubricating properties of water under extreme confinement [135, 136] and the extraordinary capacity of phospholipid membranes as boundary lubricants [137, 138], area areas of research that have garnered much attention in recent years. The experiments reported here show new aspects to the behaviour of confined water, under the adhesive confinement of a hydrated membrane. The experiments could offer insight into the mechanism of slip and lubrication in articular cartilage [139] where membranes act as boundary lubricants between polymeric networks that must rub past one another. Similarly, the observation of large scale reorganisation of lipid to accommodate changing substrate area could help explain how cells sense their environment [140, 141] and help direct future research efforts in the design of responsive bio-coatings [142].

In the future, better understanding of the system could be obtained through a coherent picture of the reorganisation events at the nanoscale, through MD simulations, scattering to determine film thickness and delicate AFM studies to probe the rheology of the interstitial film.

Finally, the existence two independent pathways to tension relaxation in the supported lipid bilayer system begs the question: what other modes of tension relaxation exist for the bilayer stressed by the elastic support? This will be the subject of the next chapter.

Chapter 7

Membrane Pores on Hydrophilic Supports

7.1 Overview

(a)   (b)
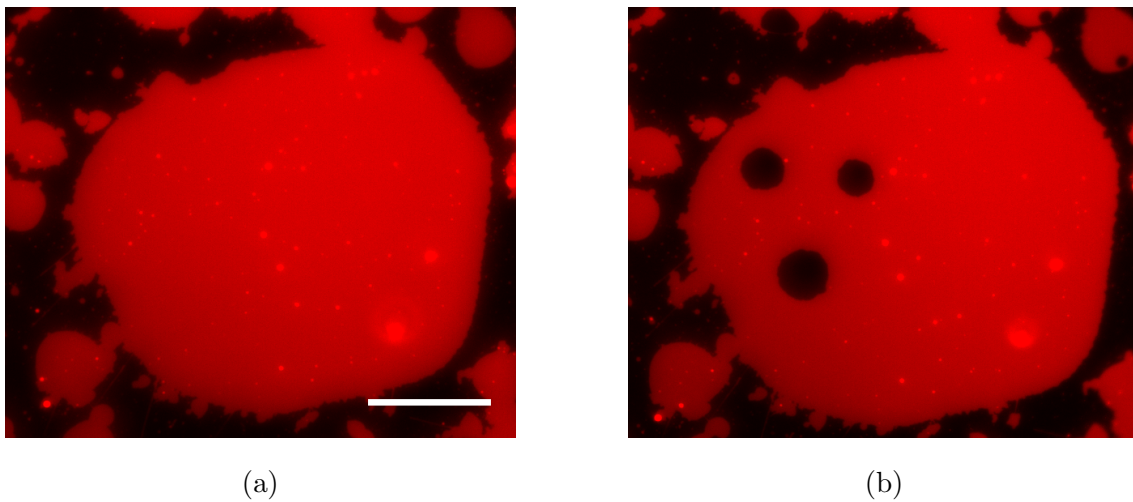
Figure 7.1: A membrane patch (a) in buffer at $\epsilon_{sub} = 0$ and (b) $\epsilon_{sub} = 4.5\%$ showing large hydrophilic pores in response to increasing ϵ_{sub}. Scale bar 50 μm.

Chapter 4 showed that the probability of GUV rupture on partially hydrophilic supports can be controlled with the pH of the buffer. It seems logical to suppose that the pH may effect the interaction between the membrane and the support on the hydrophilic substrate.

This motivates an investigation into the effect of pH on the response of the bilayer to substrate stress. By adjusting the pH to a value ≤ 6 a different response of the

bilayer to substrate stress is uncovered. The result is visually dramatic. When the buffer is adjusted to pH≤ 6, sliding becomes inhibited and the patch area becomes strongly coupled to the substrate area, analogous to the membrane response on partially hydrophilic supports. However, instead of absorbing and projecting material out of the plane, the membrane is instead forced to open large hydrophilic pores to mitigate the effect of increasing substrate strain (figure 7.1). The pore area within the membrane is a function of the substrate deformation and the pores remain stable for the time that the substrate is held stretched. Upon substrate compression the area of the pores decreases until eventually the pores reseal. Repeated application of substrate stretch and de-stretch again forces the membrane to open and close pores; in other words, there is no change in the response of the membrane.

The pores are visually distinct from the membrane pores reported in the previous two chapters, which described the mechanical remodelling of membrane patches on partially hydrophilic PDMS and the membrane sliding behaviour on hydrophilic PDMS. Both of these behaviours led to the formation of pores in the membrane at high values of ϵ_{sub}. These pores were either a consequence of the exhaustion of the lipid reservoir on top of the patches, in the hydrophilic substrate case, or the tension that accumulates in the membrane as the patch slides over and shears the interstitial water layer. The pores described in this chapter open at much lower substrate strain values, typically around $\epsilon_{sub} = 2\%$ and obtain much larger areas. The prospect of controlled membrane mechanoporation has many possible avenues of further research as well as implications for understanding processes such as apoptosis and autophagy in disease and cell physiology.

7.2   Results and Analysis

7.2.1   Framework for Analysis

The framework for analysis is similar to the protocol outlined in chapter 6.4 with the exception that the membrane pores are now measured independently of the patch area. The distinction between lipid in the plane of the support and extra lipid above the patch is again not necessary. As with the sliding behaviour, absorption of additional lipid material is a rare event.

(a)   (b)   (c)
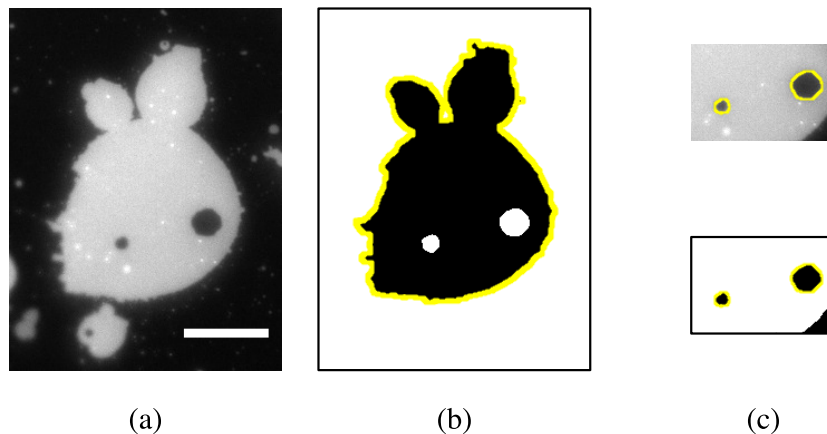
Figure 7.2: a.) Fluorescence image of a supported DOPC lipid patch with visible circular pores. Scale bar 25 μm. b.) Binary version of a.) used to determine the patch area, A_{patch}; the measured area is outlined in yellow. c.) Pore area is estimated from a separate crop of the same image stack, again outlined in yellow.

A_{patch} is defined by the contour surrounding the fluorescent lipid and includes all of the pixels, including the pores within this region. Normalisation allows for the definition of a patch strain given by equation 7.1.

$$\epsilon_{patch} = \frac{A_{patch}(t)}{A_{patch}(0)} - 1 \tag{7.1}$$

The pore area is assessed independently from a separate crop from the original image. The reason for this is that the pores are well contrasted to the fluorescent lipid but not against the substrate. The accuracy of the thresholding is therefore improved if the image background is dominated by high intensity pixel values, corresponding to lipid. The total membrane area is then calculated using equation 7.2.

$$A_{mem} = A_{patch} - A_{pores} \tag{7.2}$$

It is possible to measure the membrane area directly from binary images, such as figure 7.2b, by asking ImageJ [80] to count only black pixels within the patch confines. This method is not favoured because it is reliant on an accurate choice of global threshold and is therefore prone to inaccuracy. The method does provide an alternative analysis protocol that can serve as an independent verification of results.
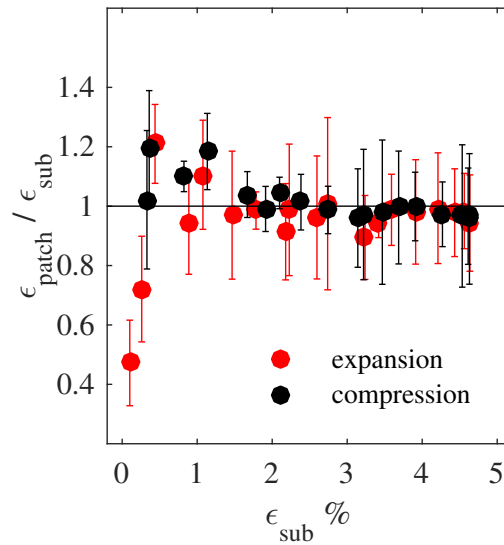
(a)
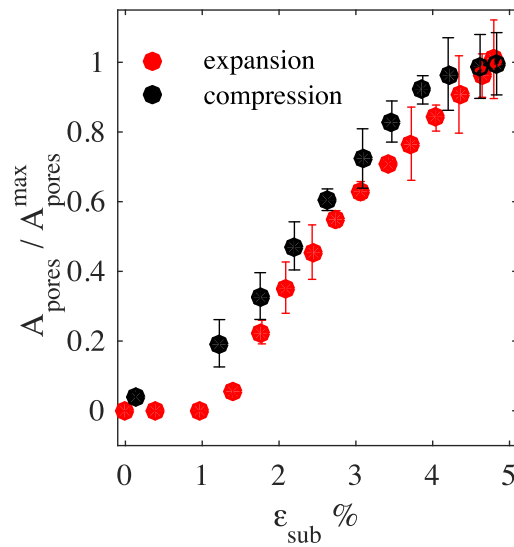
(b)

Figure 7.3: a.) Ratio of ϵ_{patch} to ϵ_{sub}, versus ϵ_{sub}. Data points are averaged over 5 independent samples and the error bars represent the spread of this data about this average. b.) Total pore area divided by patch area, versus substrate strain, for a typical experiment. Data is plotted at a reduced density to increase clarity.

7.2.2 The Dynamics of Membrane Pores

Close inspection of the pore area versus substrate strain curve reveals the interesting dynamics of membrane pore formation. The patch area is strongly coupled to the substrate area which results in a ratio of ϵ_{patch} to ϵ_{sub} of unity throughout the deformation (figure 7.3a) with a χ^2 value of 0.7. Therefore, when membrane patches open pores in response to substrate stress, for every unit of substrate area expansion the patch area also expands by one unit.

Plotting the total pore area, normalised by the maximum pore area (figure 7.3b), shows that the pore area increases during substrate expansion and decreases upon substrate compression. The pores also exhibit an area hysteresis; the pore area is larger when the substrate area is decreasing compared to when the substrate area is expanding for equal ϵ_{sub}.

Before the pores open the membrane undergoes a small expansion. This is evident from the combination of the unit value of the ratio of ϵ_{patch} to ϵ_{sub} and the pore area versus substrate strain curve (figures 7.3a and 7.3b). For $\epsilon_{sub} \approx 0 - 1.5\%$ the pore area is zero but it is known that, during this period, for every unit of substrate area increase the patch undergoes a similar increase in area. It must therefore be the case that the membrane is being stretched during the period of substrate expansion before the pores open. In the example of figure 7.3b, this small expansion is approximately $\epsilon_{sub} = 1.3\%$, which is consistent with literature values reported for the maximum stretch membranes can sustain before lysing [36, 143].

Additional insight can be gained from the analysis of the data taken from isolated patches, for which A_{patch} may be defined. This allows us to compare the rate at which the pore area is changing to the rate at which the total membrane area is changing. The rate of change of pore area with respect to the change in patch area peaks at the pore nucleation stage and relaxes to unity at higher substrate strains (figure 7.4a). This immediately tells us two things. The first is that as the pore opens, the rate at which it is expanding exceeds the rate at which the patch is being stretched by the substrate. Although figure 7.4a shows an example from a single experiment, the behaviour is general and reproducible. The second thing is that once the pore has opened, the unit value of the ratio $\Delta A_{pores}/\Delta A_{patch}$ must mean that the additional pore area is completely accounted for by the expanding substrate. Further expansion

then leads to dip in the ratio $\Delta A_{pores}/\Delta A_{patch}$ below the value of unity, suggesting that the patch is being stretched again. This would require that the tension increases within the membrane patch and is consistent with the stick-slip behaviour reported in chapter 6, where the membrane must accumulate some tension before lipid flow relative to the substrate may occur.

When the substrate area is compressed the behaviour is reversed. The area of the pores initially changes very little; in figure 7.4b $\epsilon_{sub} = 4 - 5\%$, the black data points are close to zero, before the compressing substrate begins to drive the pores to reseal. Once the pore starts to close the ratio $\Delta A_{pores}/\Delta A_{patch}$ is unity for the majority of the compression with a less pronounced peak as the pores reseal. This pattern suggests that the resealing of pores is at first substrate driven, before an assisting resealing force begins to act; the origins of which could be the line tension of a membrane pore [144].

The existence of an additional force that drives the pores to close leads us naturally to the belief that the pores would spontaneously reseal if the substrate area is held fixed. However, this is not the case and instead the pore area is stable over a typical experiment time (figure 7.4b). This behaviour is interesting and suggests that the pore area is stabilised by a friction force acting between the membrane and the PDMS surface.

7.2.3   Membrane Pores at High Substrate Strain

So far only modest deformations of the membrane have been analysed in the membrane pore forming regime. In the previous 2 chapters it was found that deforming the substrate to higher values of ϵ_{sub} provided additional information about the bilayer-substrate coupling as well as mechanistic insights. For this reason the amplitude of the substrate deformation is now increased.

Pore Area shape descriptors

Increasing the amplitude of the substrate strain has consequences for the perimeter of the pores. The shape of the perimeter may be characterised with the circularity parameter, equation 7.3, a universal definition of how circular an image feature is [145].

(a)   (b)
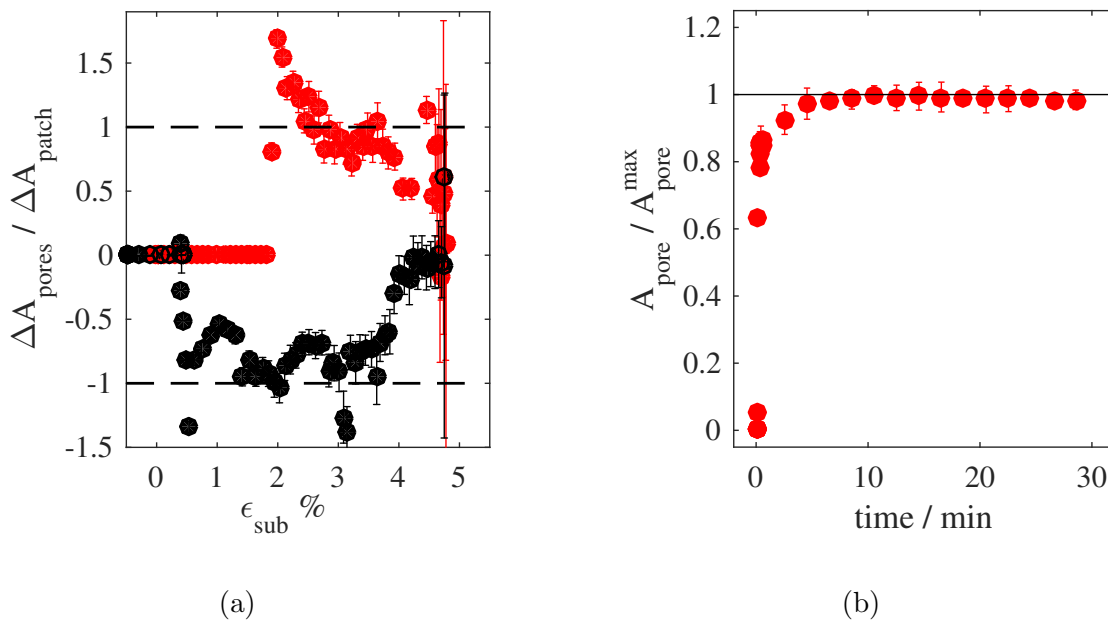
Figure 7.4: (a) Rate of change of pore area with respect to patch area for an isolated patch, for which A_{patch} is easily measured; substrate expansion is shown in red and compression is shown in black. For clarity the compression data has been multiplied by -1 such that the data does not overlap. (b) The normalised pore area remains at unity for at least 30 minutes if the substrate area is fixed.

$$\text{Circularity} = 4\pi \frac{\text{Area}}{\text{Perimeter}^2} \qquad (7.3)$$

At low to modest substrate strains the pores are almost perfect circles. Immediately after pore nucleation there is a slight increase in the mean circularity relative to the first frame in which the pores become visible (figure 7.5). Then, as the value of ϵ_{sub} increases further, there is a decrease in circularity of the pore perimeter (figures 7.5a and 7.5b). Upon compression the circularity of the pores is restored before the pores reseal. The data for substrate compression is not shown in figure 7.5a to avoid the overlap of the datasets.

Spontaneous Resealing of the Pores

When the magnitude of the maximum substrate strain is increased to large values, the pore area hysteresis can become very large and pores can still be present in the membrane patch even after the substrate strain has returned to zero (figure 7.6b). Instead of resealing with the substrate the pore area plateaus on compression and

(a)

increasing ε$_{sub}$, decreasing Circularity
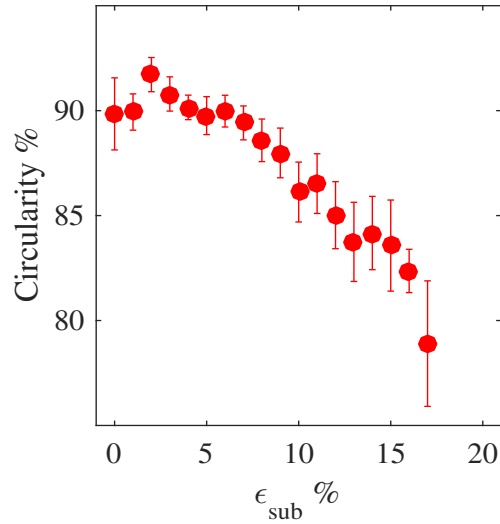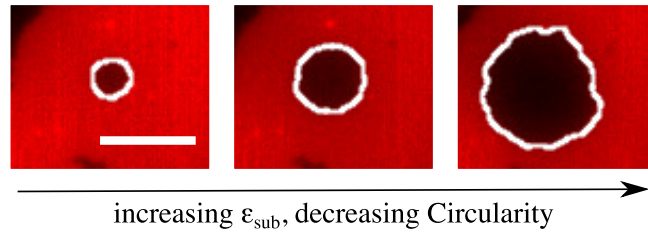
(b)

Figure 7.5: a.) Mean circularity as a function of substrate strain across 24 independent measurements; errorbars are standard error. b.) Fluorescence micrographs of an example pore, included in the data in (a) and (b) at increasing values of substrate strain. White contour indicates the thresholded pore area. Scale bar = 15 μm.

so the pores have non-zero size at $\epsilon_{sub} = 0$, figure 7.6b.

Following this, pores are observed to spontaneously reseal at $\epsilon_{sub} = 0$. To characterise this spontaneous resealing behaviour one can plot the pore area versus time after the substrate area has returned to its original area $\epsilon_{sub} = 0$. The decrease in pore area is approximated by an exponential decay, equation 7.4. The exponential model is selected purely on the basis of the results of the previous chapter, where the growth of the membrane towards equilibrium area was fitted to a similar function.

$$\frac{A_{pore}}{A_0} = \exp\left(\frac{-t}{\tau}\right) \tag{7.4}$$

In this analysis, time is defined only after the movement of the substrate ceases, to avoid convoluting the decrease in pore area with the substrate perturbation.

(a)

(b)

(c)
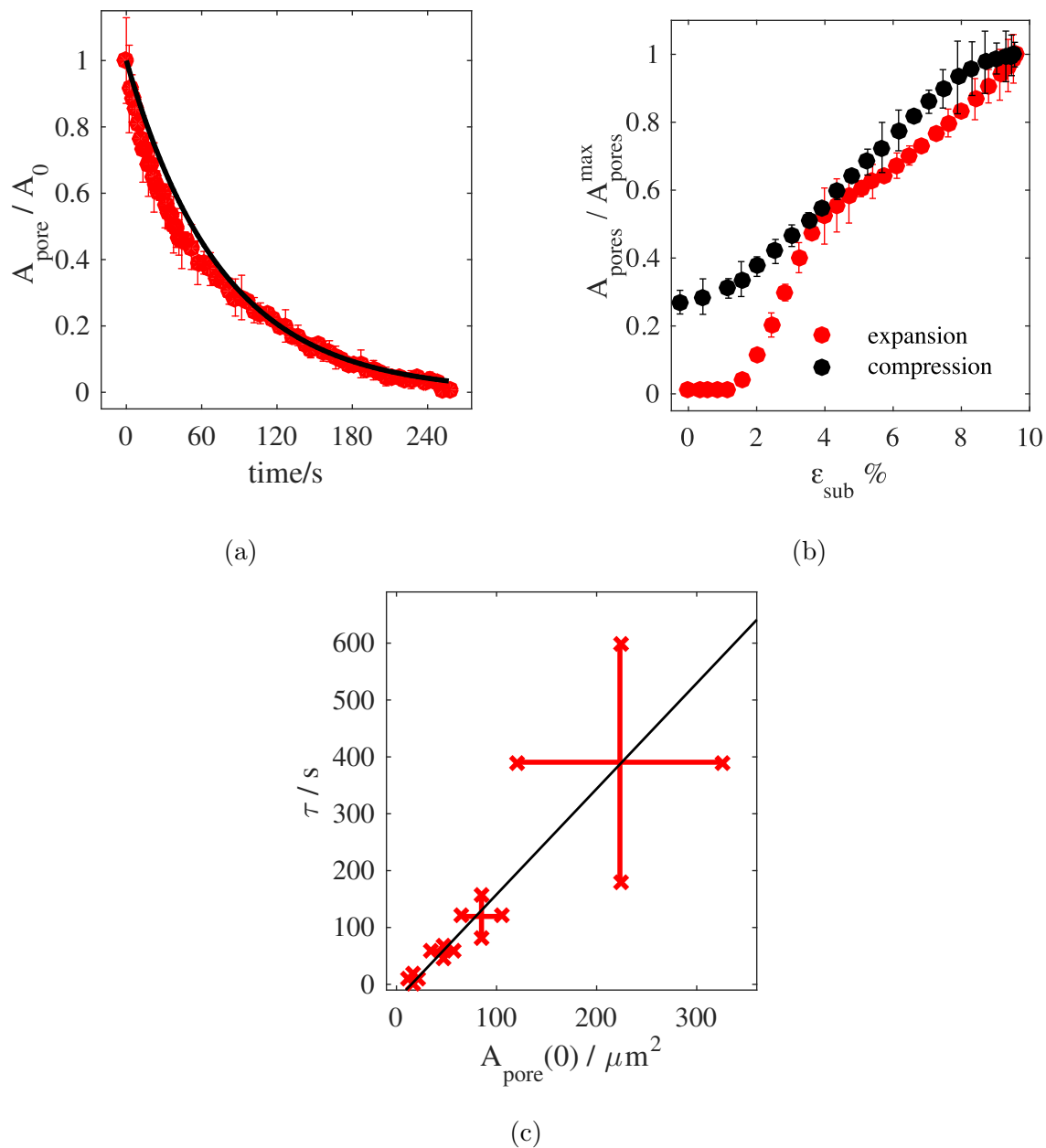
Figure 7.6: a.) Normalised pore area versus time for a single pore that spontaneously reseals at $\epsilon_{sub} = 0$. Data fitted to a single exponential, equation 7.4, which is marked by the solid black line. $\tau = 72s$ in this example. b.) Normalised pore area versus substrate strain for a representative membrane patch for which the pore area is non-zero as the substrate strain returns to zero upon compression. c.) The exponential scaling, τ in equation 7.4, describing the spontaneous pore area decrease, increases linearly with the initial pore area, A_0, for 4 independent samples. Error bars are the standard error across all pores measured on an individual sample.

There are many forces at play as a pore spontaneously reseals. A full analytical description of the behaviour would require a delicate balance of elastic energy stored in the patch, viscous dissipation as the membrane slides over the surface to close the pore and line tension that seeks to minimise the pore radius. The single exponential is a poor fit to the data but does at least capture the coarse grained behaviour and the relevant time scale.

When the data is examined heuristically and the characteristic times of the exponentials are compared between samples, it is also found that the measured time constant is a linear function of the initial pore area (figure 7.6c). This means that when ϵ_{sub} returns to zero, the rate at which pores spontaneously reseal, as characterised by the exponential in equation 7.4, is larger for pores with a larger initial area at $\epsilon_{sub} = 0$. In other words, larger pores reseal more slowly. The linear relationship between the characteristic pore resealing time τ of figure 7.6c suggests that the resealing of the membrane pores is diffusion driven since the dimensions of the inverse of the gradient of figure 7.6c have the units of a diffusion constant, $\mu m^2 s^{-1}$.

7.2.4   Pore Nucleation is Sensitive to the Rate of Substrate Strain

(a)	(b)
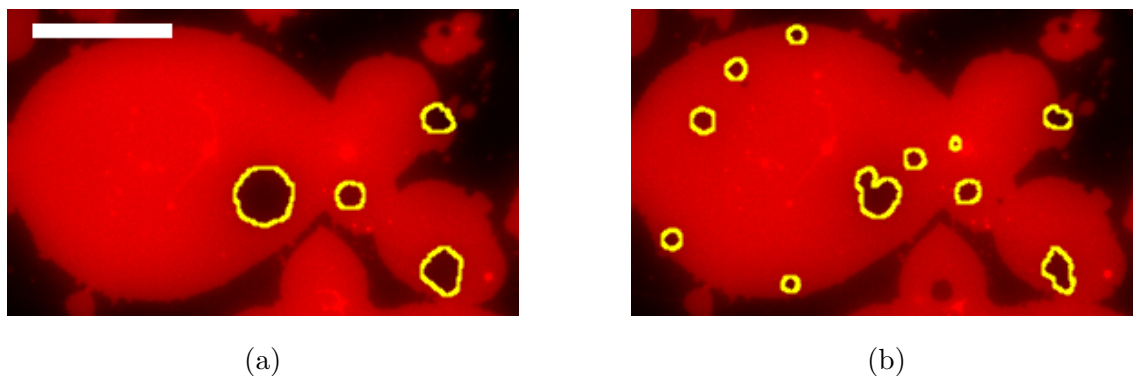
Figure 7.7: The same patch of DOPC lipid stretched to $6.6 \pm 0.3\%$ strain at a.) a *slow* rate of $0.05\%s^{-1}$ and b.) a *fast* rate of $0.43\%s^{-1}$. Measured pore areas are outlined in yellow and the scale bar is 50 μm.

The sliding behaviour reported in the previous chapter demonstrated a dependence on the rate at which the substrate deformation was applied. Motivated by

this result, it seems logical to test for changes in the pore behaviour as the strain rate is varied. Figure 7.7 shows a DOPC lipid patch at almost 7% substrate strain for which the substrate strain has been applied at two strain rates differing by an order of magnitude.

When the strain rate is slow the membrane patch expresses a preference to open fewer but larger pores (figure 7.7a), thus accommodating the additional substrate area into fewer membrane defects. On the other hand, at rapid loading rate (figure 7.7b) the patch expresses a tendency to open smaller pores, but more of them. Comparing the total pore areas, which are highlighted in yellow in figure 7.7 gives a value of $651 \pm 9 \ \mu m^2$ for the slow substrate expansion (figure 7.7a) and an area of $614 \pm 24 \ \mu m^2$ for the fast substrate expansion (figure 7.7a). A comparison between these two values however offers limited insight. This is because the subject patch in figure 7.7 is not isolated and connects to additional membrane that does not remain in focus during the experiment. Pores opening in the out of focus membrane may effect the total pore area in the portion of membrane observed.

However, comparison of the mean pore area at the two loading rates is fruitful. At a slow substrate loading rate (figure 7.7a), the mean pore area for the 4 pores highlighted in yellow is $163 \ \mu m^2$, whereas at a fast substrate strain rate (figure 7.7b), the mean pore area is much less, $56 \ \mu m^2$ for the 11 pores measured. This confirms that at slow loading rates the membrane prefers a pore area distribution with fewer pores per unit area that are on average larger in size, at slow loading rates. In comparison, at fast loading rates there are more pores per unit area but each of the pores are on average smaller in size.

7.3   Discussion

The discussion here will be confined to the subject of membrane pore formation and the understanding that develops from the analysis of the dynamics of the pore behaviour. A comparison between the sliding behaviour at higher pH values and the membrane pores at lower pH on the hydrophilic PDMS substrate will be left as the subject of the next chapter, alongside possible mechanisms that might explain the transition between these two behaviours.

7.3.1   Tension Driven Lipid Flow

Recall that the ratio of patch strain to substrate strain (figure 7.3a) is close to unity throughout substrate expansion and compression. In addition, the pores do not open immediately as the substrate begins to expand (figure 7.3b). As a consequence, tension is developed during the brief period of substrate expansion prior to pore formation because the membrane is being stretched. This tension increases the probability that the supported membrane can open a pore by decreasing the energetic hurdle that the membrane must cross in order to rupture. As self-assembled structures, membranes are always opening nanoscopic pores due to interactions with the surrounding heat bath. In a tension free environment, the majority of these attempted pores reseal automatically due to the strong cohesive interactions within the bilayer [41, 146, 147]. From the classical theory of membrane cavitation (section 2.2.2), it is known that the threshold energy barrier to membrane pore formation decreases with membrane tension [40]. This explains why it is that pores are only seen to open after an initial stretch of the patch (figure 7.3b). In other words, pores do not open in the absence of a membrane tension because the substrate perturbation is necessary to decrease the energy barrier.

The classical theory of membrane cavitation also tells us that membrane pore formation is a stochastic process [10], unlike the failure of typical condensed solids, which occurs at a defined ultimate tensile stress. Pore formation is an activated process and therefore its kinetics are governed by the rate at which the membrane attempts to form a pore. In keeping with this a fixed value of ϵ_{sub} at which the membrane first nucleates a microscopically resolvable pore is not found. Instead the

values of ϵ_{sub} at which the pores first become visible vary from $0.6 - 5\%$ (figure 7.8), in agreement with studies based on the micropipette aspiration of GUV membranes under constant tension ramp rate [39].
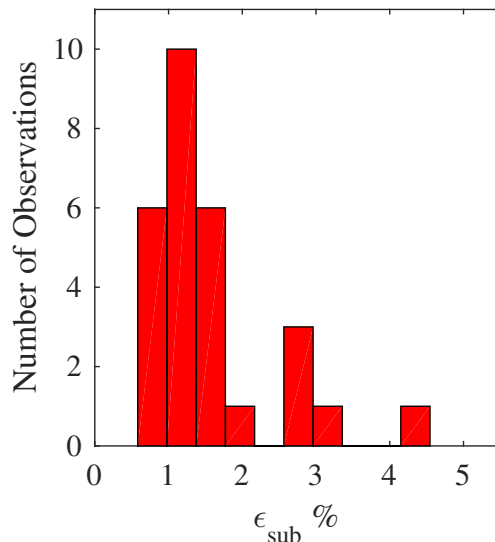
Figure 7.8: Histogram of substrate strains ϵ_{sub} at which pores first become visible in supported membrane patches for strain rates of less than 0.075% s^{-1}.

The peak in the ratio of the change in pore area to the change in patch area tells us that the rate of pore area growth is largest at the onset of pore nucleation (figure 7.4b). There must hence be a rapid redistribution of lipid as the pore opens to relax the tension accumulated in the period before the pore opens. The ratio of the change in pore area to the change in patch area relaxes to unity after the pore nucleation stage (figure 7.4a). This tells us that the supported patch is in a tensionless state after pore formation because the patch area change is equal to the pore area change. The additional substrate area is therefore being incorporated into the increasing pore area. In this way, a picture is emerging of the opening of a membrane pore as a sudden event that quickly and efficiently relaxes the elastic energy stored in a stretched lipid patch. Clearly the membrane cannot sustain the tension gradient that must exist as a pore nucleates because a quasistatic equilibrium, where additional support area is converted into additional pore area, is quickly achieved.

A small amount of substrate compression is necessary to initiate the resealing of the pores. It is interesting that the pore area does not decrease immediately with decreasing substrate area (figure 7.3b). From the unit value of the ratio of ϵ_{patch} to

ϵ_{sub} (figure 7.3a) it is understood that during this period the patch area is decreasing and therefore the membrane must be being compressed. This compression will store elastic energy in the membrane [30]. The fact that this compression is necessary to initiate the flow of lipid over the substrate, required to decrease the pore area, is consistent with the results of the previous chapter where the membrane had to overcome a yield stress before relative motion between the membrane and the substrate could begin. This tells us immediately that some viscous friction between the membrane and the substrate resists the propagation of the membrane.

7.3.2   Dissipation and Friction in Membrane Pore Regime

This flow of lipid across the substrate represents a dichotomy. On the one hand, the membrane substrate adhesion couples the patch to the PDMS area with sufficient frictional drag to stretch the membrane (figure 7.3a) Collective motion of the entire lipid patch relative to the substrate is therefore resisted. The stretch of the membrane is in fact so large that the membrane is able to lyse, yet the convective flow of lipid away from the site of pore formation is not inhibited.

The viscous friction on the hydrophilic PDMS is apparent in the pore area hysteresis. The fact that the pores are larger on compression when comparing equivalent ϵ_{sub} values immediately tells us that there is some dissipation. Elastic energy stored in the membrane must be lost as lipid flows over the substrate away from the site of pore nucleation. As a consequence additional energy must be put into the system in order to close the pores. This energy comes from the small compression of the membrane mentioned in the previous section.

The spatial distribution of pores varies with substrate strain rate (figure 7.7). This result provides more evidence of friction between the membrane and the substrate in the membrane pore forming regime. The membrane patch prefers to open a greater number of smaller pores at fast substrate loading rates and fewer but on average larger pores at fast rates of substrate deformation. This tells us that the strain rate sets the length scale over which the rapid lipid flow can be felt by the remainder of the patch. The rate of lipid flow across the substrate, which is inhibited by the viscosity of the hydration film, becomes insufficient to equilibrate tension across the entirety of the patch at high load rates. As a consequence, more nascent

pores are given the chance to cross over the energy barrier to pore formation because more membrane area remains in a tense state; this tension is necessary to lower the barrier to membrane pore formation. In keeping with this, small isolated patches do not reproduce this strain rate dependence. This observation is easily rationalised by the length scale of tension relaxation, by lipid flow, being larger than the dimensions of the small lipid patches.

The increase in the number and the decrease in mean size of pores when a patch is stressed rapidly (figure 7.7) may be rationalised using the arguments already set-up in the previous chapter that dealt with the membrane sliding behaviour. Equation 6.4 gives the characteristic time scale for the supported membrane system; this value arises by considering the ratio of elastic energies to the viscous dissipation as the relative motion of the membrane and the substrate shears the interstitial water film. At high substrate strain rates the tension relaxation effects of a single pore opening must be felt over a smaller area of the patch because many more pores are seen to open (figures 7.7b). In this way, the interstitial water film is behaving like a solid and transmitting the substrate stress to the bilayer at high loading rate. On the other hand, the water film yields when the stress is applied slowly, like a liquid, and allows the flow of lipid that surrounds a smaller number of opening pores to relax tension over larger distances. The strain rate sensitivity displayed by the spatial distribution of membrane pores is then arguably a demonstration of a viscoelastic nature of the interstitial water film that separates the bilayer from the PDMS.

When the pores reseal spontaneously at $\epsilon_{sub} = 0$, the pore area as a function of time has, at least approximately, an exponential behaviour. This behaviour is not difficult to rationalise because immediately after the value of ϵ_{sub} returns to zero, the pore area is largest. From the linear coupling of the membrane area to the substrate area (figure 7.3a), the tension in the membrane, for the time after $\epsilon_{sub} = 0$, must also be at maximum and must decrease monotonically as the pore area diminishes. The elastic energy stored in the membrane, together with the line tension around the perimeter of the pore, provide the main impetus for the pores to reseal spontaneously [41, 116]; both of these energies diminish with pore radius. As a consequence one would expect pores to reseal at first rapidly before slowing down

as the pore area approaches zero.

On the other hand, the rates at which individual pores spontaneously close are compared, then it is found that larger pores reseal at a rate that is slower than smaller pores (figure 7.6c). In fact the linearity of this relationship is consistent with diffusion limited kinetics describing the pore resealing behaviour. This is because the dimensions of the inverse gradient of the plot of τ versus the initial pore area A_0 are that of a diffusion coefficient. Extracting the numerical value of the slope of figure 7.6c and taking the inverse, yields a value of 0.54 $\mu\mathrm{m}^2\mathrm{s}^{-1}$. In many respects the spontaneous flow of lipid into the pore region resembles the recovery of fluorescence observed when a membrane is photobleached yet this value is larger than all of the FRAP mobilities given in table by roughly a factor of two. This could be evidence of additional line tension forces and/or tension in the membrane directing the diffusive motion of lipid in order to reseal the pore. Line tension forces are strong in GUV membranes and have significant impact on membrane phase behaviour [148] and structure [118]. Amphiphilic membranes also have large elastic area moduli [36, 143]. A higher membrane tension and large line tensions associated with larger pores should both act to close larger pores at a more rapid rate. The results reported here may show that, in the supported patch system, the spontaneous resealing behaviour of the membrane pores may be driven by lipid diffusion.

Indeed, the pores are not seen to close spontaneously if the substrate area is held fixed at the maximum value $\epsilon_{sub} \neq 0$; instead the pores are stable at maximum substrate strain (figure 7.4b). The friction at the membrane substrate interface clearly exerts a strong slowing down and stabilising effect on the membrane pore dynamics. Here one may draw an analogy with the result of stressing GUV membranes to form pores in viscous solvents [144, 149]. Transient membrane pores have been imaged in this way and the dynamics are slowed down significantly by the slow leak of the viscous solvent contained in the GUV. The GUV pores expand rapidly before reaching a maximum radius and finally resealing again. What has been witnessed here, in the supported membrane system, suggests that another way of stabilising macroscopic membrane pores is through the interaction with the support; indeed this system may actually be advantageous because the pores are stable for longer durations (figure 7.4b).

7.3.3   The Action of Forces Arising from the Pore Line Tension

Increasing the substrate strain amplitude, ϵ_{sub} first causes a slight increase followed by a dramatic decrease in the circularity of the pores. The initial increase in circularity is, perhaps, consistent with the peak in the ratio of ΔA_{pores} to ΔA_{patch} of figure 7.4a. At the point of pore nucleation there is a rapid flow of lipid. This rapid redistribution of lipid is most likely to be non-equilibrium; transient instabilities could therefore permit an initially non-circular pore shape. As soon as the rate of lipid flow relaxes to a rate that is comparable to the substrate expansion, in other words when the ratio of ΔA_{pores} to ΔA_{patch} is unity, a quasi-static equilibrium is established where the additional substrate area is matched by the increase in pore area. At this point the effects of pore line tension can drive the pore to adopt a circular shape.

The circular shape minimises the perimeter of the membrane pore for a given area and is consistent with the notion of a strong line tension associated with the pore, which arises from the curvature of structure adopted by the lipids at the pore perimeter [116, 150]. The departure from high circularity at high substrate strain suggests the introduction of some destabilising force, comparable to the pore line tension that disrupts the shape of the pore. In direct analogy to the roughening of spreading membrane fronts observed on silica [151], a drag force arises from the shear of the interstitial water film around the expanding pore. Subtle variations in the shear resistance of the interstitial film could then explain the observed roughening of the pore perimeter at high substrate strains.

7.3.4   Applications of Membrane Mechanoporation

The potential applications of supported membranes that exhibit reversible and controllable mechanoporation are extensive.

Lipid membranes provide the fundamental motif for encapsulation in life [152] and membrane integrity is key to the survival of all organisms. However, many biological processes, for instance cell division and membrane trafficking, require that the membrane be strategically perforated. For this reason there is a large class

of biomolecules dedicated to the task of puncturing the membrane [153], including proteins and peptides [87]. Improved understanding of how pores can be opened in a simple supported lipid system, completely devoid of these functional molecules, will undoubtedly help elucidate the mechanisms of these functional molecules in more complicated systems. Indeed, the reconstitution of proteins in tense membranes as a biophyscial platform for understanding how protein function depends on the state of the membrane has been a goal for researchers for many years [12]. Understanding the response of a simple membrane to substrate deformation should assist with these research efforts.

Intricately related to the formation of pores in a membrane is the concept of membrane mechanical tension [9]. Over the last two decades, increasing impetus has been placed on membrane mechanical tension as a signalling tool that cells use to communicate and sense their environment [154]. Despite the importance of mechanical tension as a parameter, the processes governing tension regulation are still debatable [155]. Membrane pores provide an obvious means of regulating membrane tension and the experiments reported here offer unique insights into the interplay between membrane tension and membrane pore formation without the regulatory capacity of cell metabolism.

The fact that the pores can be made to both open and close, as well as the spatial distribution's sensitivity to strain rate, means that the perforation of the membrane is controllable and repeatable. Controllable membrane pore formation has numerous applications in medicine and drug delivery. Controlled membrane lysis, and understanding the mechanisms in programmed cell death, are fundamental to our understanding of disease [156] and the development of new treatments [157]. Transport in and out of membrane organelles using light activated molecular motors has recently been proposed as a novel method of targeted drug delivery [158] and future designs based on membrane substrate systems could arise from the studies reported here.

Pore formation in supported lipid films also has many applications in technology. SLBs provide high electrical resistance [19], useful platforms for adaptive biosensors [159] as well as an obvious choice of coating to prevent biofouling. A controlled array of membrane pores therefore has exquisite potential in the optimisation of

such systems; indeed membrane based filtration systems have recently benefited from supported lipid bilayer based insights [160].

7.4 Conclusions

This chapter has shown that membrane patches on hydrophilic supports can be made to open large hydrophilic pores in response to substrate deformation that reseal when the substrate area is compressed. This represents an alternative mechanism of substrate stress relaxation to the sliding of lipid membranes over hydrophilic supports described in the previous chapter.

The dynamic between the pore area and the substrate area has revealed complex membrane flow patterns that are orchestrated by the tension in the membrane. A pore area hysteresis, where pores are larger upon substrate compression compared to substrate expansion at equivalent substrate areas, has been reported. This tells us that there is some viscous dissipation that the membrane must work against in order to flow over the substrate and open and close membrane pores. In addition, the spatial distribution and mean size of the pores in the membrane patches has been shown to depend on the rate at which substrate stress is applied.

The prospects of controlled mechanoporation for substrate-supported membranes have much potential in research and technology. Further insights into the mechanism of tension driven pore formation in membranes may be obtained from these results, which may further our understanding of important membrane perforating processes such as membrane fusion and fission. In addition, controlled exposure of a substrate in response to mechanical perturbation has much potential for the design and development of new classes of biosensor.

Chapter 8

The Transition Between
Membrane Pores and Membrane
Sliding

8.1 Overview

On hydrophilic PDMS so far two mechanisms by which the membrane can relax the stress imposed by a changing support area have been encountered. In chapter 6, a regime where the membrane, on fully hydrophilic PDMS, is able to slip relative to the substrate is described; the membrane preserves its area through this slip and allows the substrate area to change independently. In chapter 7, the pH was lowered and, whilst the substrate hydrophilicity remained the same, the membrane responds to substrate stress by opening and closing large pores.

It is experimentally possible to transition between these two regimes of membrane behaviour. The transition is apparently triggered by a simple adjustment of the pH of the buffer surrounding the membrane and is completely reversible. For pH values of 6 or less, membrane patches open pores; for pH values in excess of 7, the membrane patches slide. It is truly remarkable that these pathways for membrane stress relaxation can be controlled robustly by adjusting a single experimental parameter.

8.2   Results

8.2.1   pH Dependence of Membrane Response

Buffer Species	Bis-TRIS	MES	TRIS	HEPES
pH	6	5,6	7,7.5,8,9	8,9
Observed Behaviour	pores	pores	sliding	sliding

Table 8.1: Table of experimental conditions used to examine the stress response of DOPC membrane on hydrophilic PDMS supports.

Attributing the transition to the change in pH required the use of different buffers, since most buffer molecules have a buffering capacity that operates over a limited pH range. To examine the membrane behaviour, Bis-TRIS and MES were used at pH 5 and 6. To examine the membrane response at higher pH values of 7,8 and 9, TRIS and HEPES buffer were used. The patches open large hydrophilic pores in response to substrate deformation if the pH is less than or equal to 6 whereas the membrane patches slide if the pH is greater than or equal to 7, regardless of which buffer molecule is used at a given pH. The use of two independent buffer molecules, for each regime, confirms that the transition is pH dependent. The different buffer conditions used are summarised in table 8.1.

Performing the experiment in any of the buffers listed in table 8.1 will yield the response described; thus, the transition is controlled. Importantly, all buffers listed in table 8.1 are prepared at constant ionic strength by topping up the charge content of each solution using neutral NaCl salt (section 3.2.4). Therefore, the transition cannot be caused by the effects of ions on the membrane since these effects should be constant when comparing the action of a particular buffer.

8.2.2   The Transition is Reversible

A single patch can be observed to respond in both the pore and sliding regimes by washing with buffer of appropriate pH. Sufficient time must be left to allow the system to equilibrate between the washing steps. In the example given in figure 8.1, this delay is fixed at 30 minutes. The value of A_{pores}/A_{patch} at pH 7.5 stays very
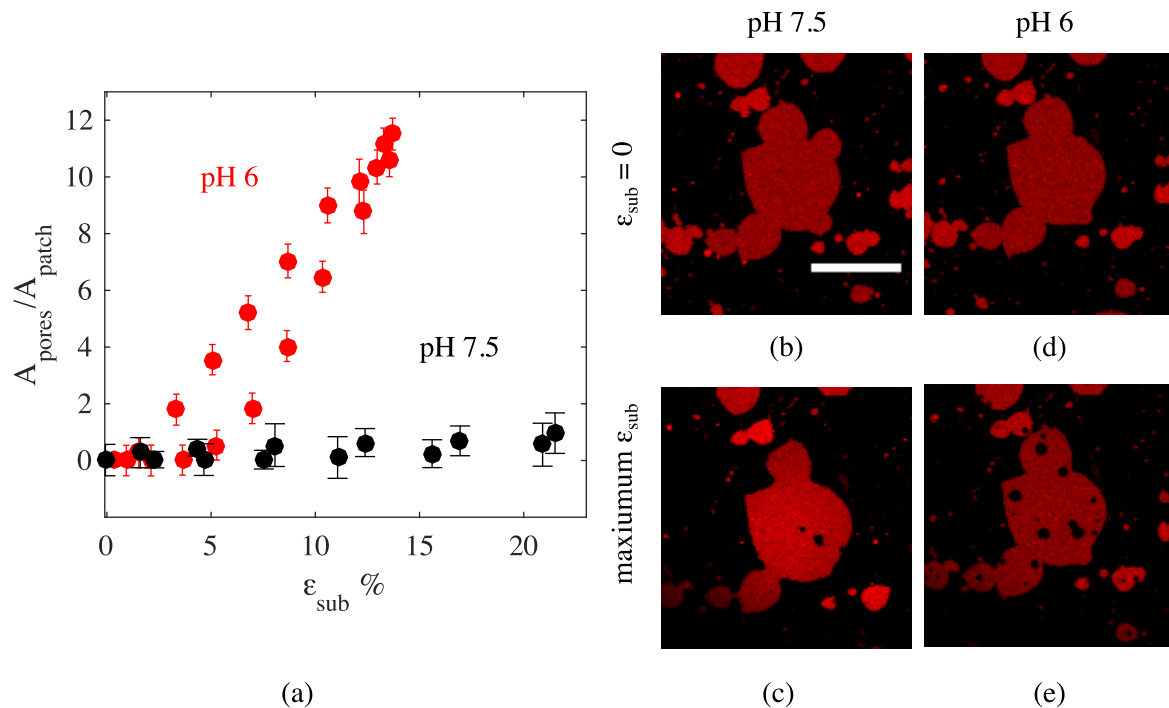
Figure 8.1: The transition between the pores and sliding behaviour is reversible. (a) Normalised pore area versus substrate strain for four sequential applications of substrate stress on a single patch of DOPC lipid. Substrate expansion and contraction were performed in buffers of the following order of pHs, 7.5, 6, 7.5 before finally 6 again and the data is averaged over the two experiments at the same pH. (b)-(e) Fluorescence micrographs of the membrane patch quantified in (a). (b) TRIS buffer at pH 7.5, $\epsilon_{sub} = 0$, scale bar 50 μm. (c) TRIS buffer at pH 7.5, $\epsilon_{sub} = 22\%$. (d) Bis-TRIS buffer at pH 6, $\epsilon_{sub} = 0$. (e) Bis-TRIS buffer at pH 6, $\epsilon_{sub} = 12.5\%$.

close to zero up to an ϵ_{sub} in excess of 20%. In comparison, A_{pores}/A_{patch} reaches 6% after a much smaller substrate deformation, $\epsilon_{sub} \leq 13\%$, at pH 6 (figure 8.1). This clear difference in pore area is repeatable; one can transition back and forth between the pores and sliding responses.

8.3 Continuous Lipid Bilayers

In the previous section it was shown that changing the pH can be used to transition a membrane patch's response to substrate stress between the sliding and pore forming regime, repeatedly, on hydrophilic PDMS . Motivated by this result one can test whether or not the pH has an effect on the response of continuous lipid bilay-

(a)

(b)

(c)   (d)   (e)
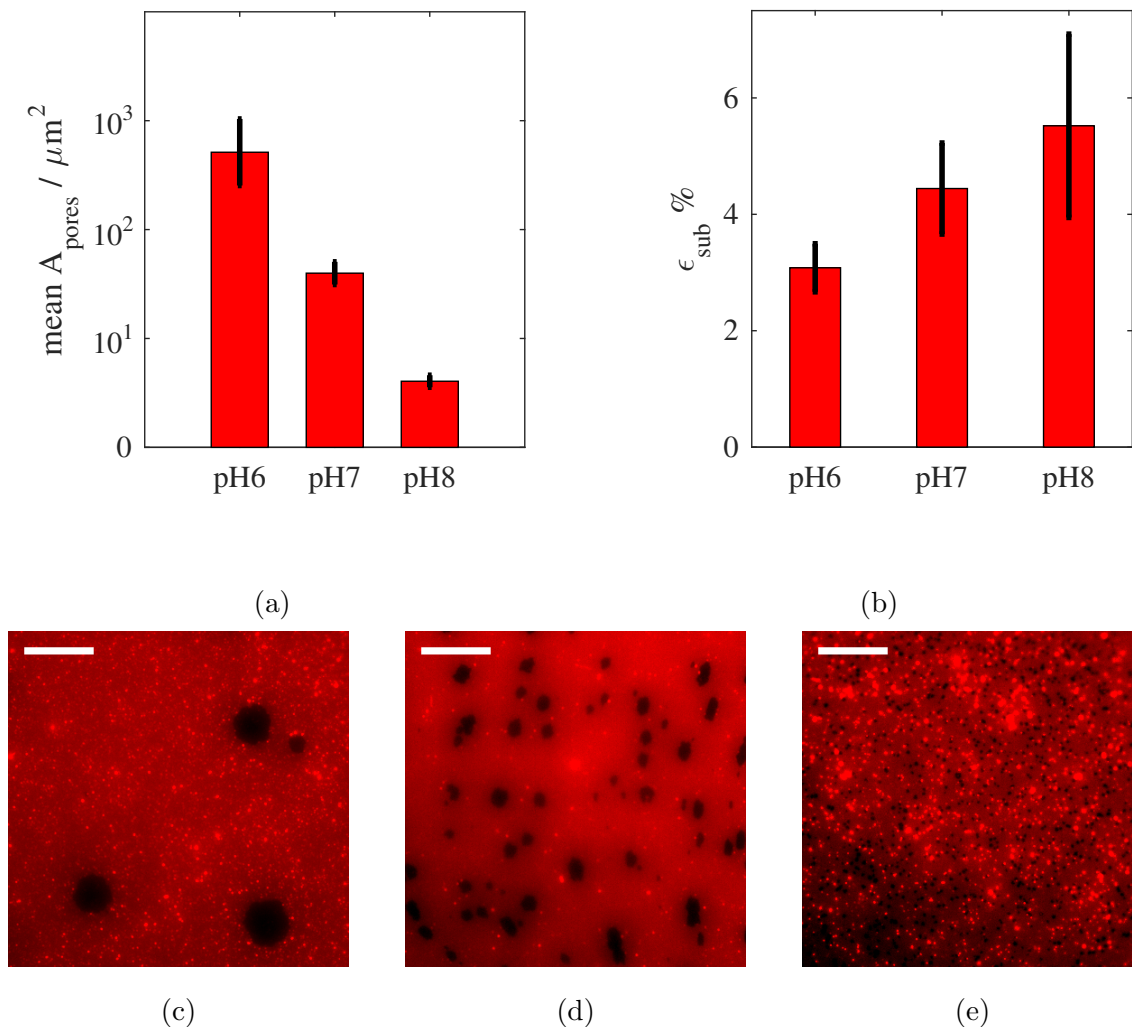
Figure 8.2: a.) Bar chart of mean pore area within a 100 μm^2 imaging area for SLBs at $\epsilon_{sub} = 7\%$ in buffers of 3 different pHs. b) Bar chart of the mean substrate strain, ϵ_{sub} at which pores first become visible in continuous lipid bilayers formed at different pHs. c,d & e.) Fluorescence images of SLBs at $\epsilon_{sub} = 7\%$ from SUVs formed at pH6, 7 and 8 respectively. Scale bars are all 50 μm.

ers, whose lateral dimensions are considerably greater than the size of a membrane patch.

It is possible to form SUVs at different pHs (chapter 3, section 3.2.2). Experimentally it is found that the lower the pH of the buffer, the larger the mean pore area in a 100 μm^2 area of continuous lipid (figure 8.2a), when these membranes are stretched by the device. This measurement refers to the average pore area and not the total pore area within the 100 μm^2 area of continuous lipid. From the images 8.2c, 8.2d and 8.2e it is clear that the lower the buffer pH the more the

membrane prefers to open larger membrane pores, but fewer of them, at fixed substrate strain. In addition the average substrate strain at which the membrane pores first become visible is an increasing function of substrate strain (figure 8.2b), with the continuous lipid membranes formed at pH 6 opening pores at lower substrate strains than pH 7 and pH 8.

The images and data presented in figure 8.2 are taken from experiments using SUVs formed in a given buffer with fixed ionic strength. The dried lipid film is rehydrated with a buffer, sonicated and then diluted with the same buffer before being deposited on the device. At no point during the preparation or experiment does the buffer composition or pH change.

This permits us to draw two important conclusions. The first is that continuous lipid membranes can be formed on hydrophilic PDMS across the pH range studied and the second is that the buffer pH can also be used to change the response of continuous lipids to substrate stress.

8.4 Discussion

8.4.1 Isolating the pH as the variable that triggers the transition between membrane responses

A change in the behaviour of the membrane in response to substrate stress on hydrophilic PDMS that is apparently due to a change in the pH of the buffer has been demonstrated. However, due to the limited pH range of the buffers used in this study, it is proved difficult to show both behaviours, that is the membrane sliding and the pore-forming regime, with a single buffer species. I wish to clarify my lines of reasoning as to why the transition from membrane sliding to pore formation is due to the pH and not another variable that changes when you exchange buffer solutions.

It is known that the change in response of the membrane patches to substrate deformation is not due to the presence of NaCl ions in the buffer because the ionic strength is adjusted to 150 mM in all buffers used (appendix C). The effects of the NaCl are therefore constant throughout the experiments therefore the transition cannot be attributed to ionic strength or the charge quantity in the solution.

Changing the pH from 6 to 8 represents a 100 fold decrease in the hydroxide ion concentration from 10^{-3} to 10^{-5} mM. Since the concentration of NaCl is 150 mM the hydroxide ions should intuitively be outcompeted by the NaCl excess. On the other hand, the hydroxide ion has the highest possible charge density of any monovalent ion and the lipids, DOPC, are zwitterionic and fluid. Because of the fluidity of the lipids the head group is permitted to orientate at an angle such that a dipole develops across the hydrophilic interface. This leads to the bilayer surface obtaining a modest negative potential [105]. Because of this orientation of the fluid lipid head groups, cations are able to preferentially adsorb to amphiphilic interfaces, a notion that is supported through theory [161] and experiment [78, 162]. Cation binding has similarly been shown to affect the membrane properties [64, 108]. Due to the hydroxide ion's high charge density it is not difficult to believe that the hydroxide ion could adsorb strongly to the membrane-substrate interface and thus have significant impact on the system.

The transition behaviour can be reported as reproducible for the buffers listed in table 8.1. Similarly the use of at least two independent buffer molecules for each of the behaviours, membrane pores and membrane sliding, is evidence that the behaviour is not an artefact of the buffer molecule used. For instance, if the patches are formed in pH 6 Bis-TRIS or MES then the membrane opens pores. Despite this, anomalous stiffening of supported lipids in the presence of certain buffer molecules cannot be excluded [109, 163] and both behaviours, sliding and pores, have yet to be reconstituted with a single buffer species.

8.4.2 Differences in the Membrane Flow Behaviour in the Pores and Sliding Regimes

Contrasting the two membrane responses, it is surprising that, in the pore forming regime, lipid flow is permitted only within the interior of the patch, whereas in the sliding case movement of the lipid relative to the substrate is allowed at the membrane edge. Something is therefore anchoring the perimeter of the patch relative to the substrate (figure 7.4b).

As the membrane pores open, membrane flow is permitted as the pores nucleate, with lipid flowing rapidly away from the site of pore formation, but the perimeter of

the patch remains fixed. Conversely, at higher pHs, in the sliding regime, the patch is not fixed and the lipids can remain stationary in the laboratory frame whilst the substrate motion has the effect of shearing the interstitial water film between the membrane and the support. For a whole membrane patch to slide a length scale over which relative flow between the lipid and the substrate can relax tension at least as large as the maximum lateral dimension of the patch is required. This length scale is determined by the friction and, by extension the adhesion, between the membrane and the substrate. If lipid is coupled strongly, by interstitial friction, to the substrate then the relaxation caused by lipid flow will only be felt a short distance away from the site of lipid flow, as is the case for the membrane pore forming regime. These results suggest that pH is affecting the length scale over which lipid flow can act to relax the accumulation of tension in the patch.

In both behaviours, tension is accumulated in the interior of the membrane patch. This is because the sliding patches always open pores at high substrate strain and, in the pore-forming regime, the pores are larger on substrate compression than expansion. The relative flow of the bilayer over the substrate is thus opposed by some viscous dissipation. In the pore-forming regime, why is lipid flow allowed when a pore nucleates but the overall sliding behaviour of the patch is not permitted?

To explain this one needs to look at the possible effects of pH could have on the system.

8.4.3 Rationalising the Transition between Pores and Sliding

The repeatable and reversible observation of two independent responses to substrate stress for the same lipid patch is truly fascinating; what effects could the pH be having on the system? One possible explanation is that the membrane properties are affected; at low pH the yield stress of the membrane, which is related to κ_A, is lower, leading to an increased probability of pore formation. Alternatively the way in which stress is transmitted to the bilayer from the substrate, *via* the frictional coupling, could be pH dependent. This frictional coupling is intuitively a function of the water layer's resistance to flow, that is the viscosity η, which might also be pH dependent.

In other words, two competing effects are in action during the experiments. The forces of lipid cohesion are acting to maintain the integrity of the membrane. These are strong and originate from the large entropic penalty associated with exposing lipid hydrocarbons to aqueous solvent [164]. The forces of lipid cohesion are working against the adhesion between the membrane and the substrate which governs the coupling of the substate stress to the lipid patch [44]. If the adhesion between the membrane and the substrate is high then the force of friction will also be high, favouring a lipid area change that follows the substrate area change, i.e. the pore forming regime. If the substrate adhesion is weakened, then the membrane area will not be as strongly coupled to the substrate area, and the membrane will slide over the hydrophilic surface.

In what follows the known effects of pH on similar experimental systems from the literature will be discussed.

pH Effects on Membrane Properties

The discussion begins with the possible effects of decreasing pH on the yield strength of the membrane. Any changes would provide a succinct explanation for the two behaviours.

The optimum area per lipid represents a trade off between lipid cohesion, VdW interactions between lipid hydrocarbon tails, and repulsion that exists between the polar head groups (section 2.2). Hydrated cations, including protons, are known to have high affinity for the phosphocholine head group [63]. Proton adsorption could perturb this structure, deceasing lipid cohesion and lowering the barrier to membrane pore formation. However, given that the interactions between the polar head groups of lipid molecules are repulsive [44] and the screening affects of neutral salt [45], it seems more likely that a lower pH would increase the cohesion of the membrane [165]. One notable micropipette aspiration study, using 1-stearoyl-2-oleoyl-phosphatidyl-choline (SOPC) lipid, reports an anomalous decrease in the elastic modulus of phospholipid vesicles at pH2, but no effect in the pH range 3-9 [61].

On the other hand, AFM provides a useful platform for studying the resistance of bilayers to both normal and lateral forces. The work of Garcia-Manyes describes

the changes in the force required to puncture the supported membrane with an AFM tip as a function of lipid saturation, chain length, solution composition and temperature [65]. Membranes are found to resist normal deformation with increasing tenacity as the degree of saturation, chain length and cholesterol composition increases. Mechanistically this higher strength arises from the increase in lipid cohesion. Saturated lipids can pack closer together and cholesterol also has a condensing effect on the membrane, whilst ion binding reduces repulsive forces at the lipid head group, again allowing the lipids to pack closer together.

AFM force rupture spectroscopy provides a well defined perturbation to the membrane but conclusions obtained in this way require careful consideration of the tip sample interaction. One method that does not require significant perturbation from the experimenter is the analysis of vesicle membrane fluctuations. Membranes are soft and as a consequence will fluctuate due to interactions with the surrounding heat bath. Analysis of the spectrum of these fluctuations can be used to assess the membrane resistance to bending and other mechanical properties [35]. Membrane composition and external solution composition have both been shown to affect the mechanical properties of vesicles. Clearly then, the experimental conditions do have tremendous potential to influence membrane physical properties.

It would appear then that the literature does not offer a consistent answer to the effects of pH on the rigidity of membranes. For this reason it is desirable to have a set of systematic micropipette aspiration experiments for DOPC lipids to measure any changes in bending moduli, κ_B and/or area compressibility moduli κ_A, of vesicle membranes as a function of pH [166]. Particularly because this might help explain the observed change in the response of the membrane to substrate stress as the pH is varied.

pH Effects on the Membrane-Substrate Interaction

Another possibility is that the variation in pH, alters the membrane-substrate interaction and changes the way in which stress is transmitted to the membrane. pH is reported in the literature to be a versatile tool for encouraging bilayer deposition *via* vesicle fusion [86, 93] on silica and analogous substrates. This is largely attributed to the modulation of the surface charge density with the buffer pH [88, 133]. Mech-

anistically, the change in charge density is proposed to increase the relative strength of attractive vesicle-substrate interactions over repulsive forces such as the EDL and steric or hydration repulsion. Indeed in section 4.2.3 pH was shown to be an effective tool for encouraging GUV rupture on partially hydrophilic PDMS. Lowering the pH might therefore increase the strength of adhesive interactions between the membrane and the substrate over repulsive interactions. The equilibrium water film thickness between the substrate and the bilayer represents a balance between repulsive and adhesive interactions between the membrane and the substrate [134]. The water layer thickness could therefore be impacted by the buffer pH.

Let us propose that the pH perturbs the structure or thickness of the water layer between the bilayer and the substrate. A shear stress is applied to the bilayer, through the interstitial film when the substrate area changes. If the film behaves like a Newtonian liquid, this shear stress can be described by equation 8.1, where $\frac{F_{\parallel}}{A_{patch}}$ is the shear stress, $v_{\parallel}$ is the relative velocity of the two surfaces, η is the water film viscosity and h is the water film thickness (section 2.3.1).

$$\frac{F_{\parallel}}{A_{patch}} = \frac{\eta v_{\parallel}}{h} \tag{8.1}$$

The resistance to lipid flow is inversely proportional to water layer thickness. If the pH tips the balance in favour of attractive interactions, then a decrease in film thickness could result, leading to an increase in the friction between the membrane and the substrate; possibly enough to transition from the sliding behaviour to the pore formation behaviour.

Alternatively, the shear viscosity η could vary with the solution pH. The behaviour of water under extreme confinement is a hotly debated topic in the literature. The paradigm of hydration lubrication attributes the effectiveness of water as a lubricant through the confinement of water promoting the fluid phase and not solidification like most organic liquids [139, 136]. In contrast, highly confined environments such as carbon nanotubes have recently been shown to preserve ice like properties of water at temperatures well above freezing [52, 167]. Given that phospholipids are one of the most hydrated molecules in biology it seems reasonable to suggest that the viscosity of the water layer confined between a membrane and a silica-like support could exhibit a pH dependent viscosity.

The surface of oxidised PDMS will become charged at high pH through the dissociation of hydroxide ions from surface silane groups [168]. Water molecules have been shown by MD simulations to order and relax differently at charged interfaces [128, 169], exhibiting different vibrational frequency spectra as a function of solution pH. If water molecules order differently next to charged or uncharged PDMS this might give rise to a pH dependent water viscosity that explains the transition between the observed membrane behaviours.

An informative class of experiments that might assist in detecting changes to the membrane substrate interaction are provided by the surface force apparatus [44, 170] in which two surfaces attached to very sensitive springs are brought into close contact. The forces acting between the surfaces are then calculated by careful monitoring of the displacement of the springs. The technique has recently been expanded to measure the lateral interaction between surfaces [171]. In this way the normal and lateral interaction between a membrane and PDMS or PDMS analogue could be determined as a function of pH.

8.4.4   Continuous Lipid Bilayers

For continuous bilayers a decrease in the mean pore area at equivalent substrate strains and an increase in the value of ϵ_{sub} at which pores first become visible with increasing pH (figure 8.2) is reported. These results show that the tension is relaxed in a different way for the SLBs prepared at the different pH (figure 8.2a). At low pH the membrane chooses to open large pores that are fewer in number. As the pH increases the membrane prefers to open a greater number of smaller pores and also at higher values of ϵ_{sub}. Taken together, these observations suggest that the pH change constitutes a continuous change in the system properties because the behaviour is not the same at any of the pH values studied. This was not apparent from the supported patch data, in which the behaviour at pH 7 is essentially indistinguishable from the behaviour at pH 8.

There are then some differences between the supported patch behaviour and the continuous lipid bilayer behaviour. This difference might then be attributed to the larger area of the membrane coupled to the support.

It should be remarked that sliding is difficult to detect when using the continuous

lipid membranes. In order to see membrane sliding, that is movement of the lipid relative to the substrate, a membrane edge is necessary. In this way, the pores opening in the continuous membranes at high pH is inevitable even if the membrane is sliding.

8.5   Conclusions

A reversible and controllable modulation of the response of lipid membranes patches to substrate deformation has been described.

It has been shown that the experimental trigger is simply the pH of the buffer, which is easy to control and alter *in situ*. At low pH, the membrane shows a pronounced preference to open and close pores; at higher values the membrane is able to slide to preserve its integrity.

Continuous supported membranes also show a pH dependence, exhibiting larger pores, at lower pHs and a continuous decrease in mean pore area as the pH is increased. Continuous membranes also open pores at higher values of substrate strain as the pH is increased.

Finally arguments have been proposed, based on the pH perturbing either the properties of the interstitial water layer between the membrane and the substrate or the mechanical parameters of the membrane, to help explain the transition between the two system behaviours.

The implications for these results are interesting. Membranes have multiple uses in the development of biosensors and responsive antifouling coatings [18, 20]. Tuneable membrane mechanoporation conceivably allows for the strategic use of the fouling properties of PDMS to filter biomolecules or the development of microfluidic based medical devices [160].

In addition, much of the sensation derived from food is a consequence of the texture changes of food under mechanical deformation [172]. Since membranes are biologically compatible, the behaviour reported here may help to develop new food types that respond to mechanical stimulation.

Finally, GUVs garner much attention in research as capsules for targeted drug delivery; the transition from pores to sliding reported here has obvious implications for how drugs and metabolites might be shuttled into target organs using giant vesicles [124].

Chapter 9

Efforts Towards Patterning the Deposition of the Bilayer

The response of the membrane to substrate area change on PDMS substrates on low surface energy supports is described in chapter 5. The membrane accommodates surface area changes by absorbing and projecting lipid out of the plane of the support.

The membrane response on high surface energy PDMS is described in chapters 6 and 7 where a pH dependent membrane behaviour is uncovered; the patches slide relative to the substrate at high pH and open large pores in response to substrate expansion at low pH.

A natural question therefore arises, how might the membrane respond on a surface that presents a gradient of surface energy? In other words, can the out of plane and in plane membrane responses be combined?

Using a TEM grid it is possible to cover the PDMS substrate with a recycled TEM sample holder (figure 9.1a). The TEM grid consists of a circular frame supporting a square copper grid. In the image (figure 9.1a), the black regions correspond to copper frame and the white squares are empty space. The image is extremely well contrasted due to the opacity of copper. Analysis of the binary image gives a mean length of the white squares 56 ± 0.5 μm.

A gradient in substrate hydrophilicity may be achieved by placing one of TEM grids over the top of the PDMS substrate during plasma oxidation. The presence of the copper shields the surface from the effects of the plasma cleaning procedure.

(a)

(b)

(c)
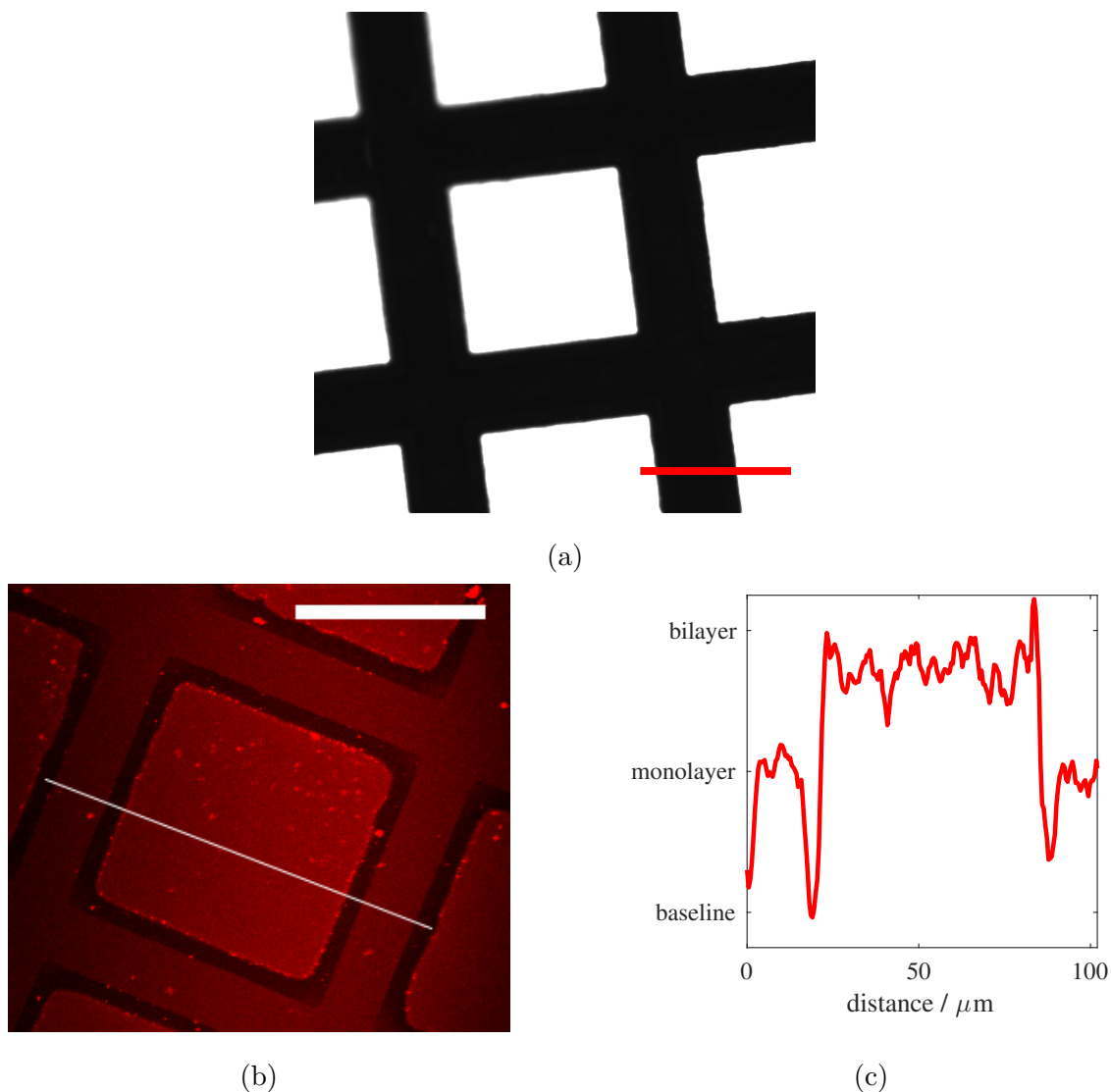
Figure 9.1: Upcycled Transmission Electron Microscopy (TEM) grids can be used to create a surface with a spatial gradient of surface energy, to which a membrane can be coupled. a.) Brightfield image of a TEM grid, scale bar 50 μm. b.) Patterned supported lipid bilayer achieved using the TEM grid (a) to selectively shield the substrate surface during plasma oxidation, scale bar 50 μm . c.) Fluorescence Intensity (FI) line scans taken across the image (b) reveal 3 distinct levels in fluorescence.

This method is completely analogous to the protocol described by Lenz *et al.* [103].

As a consequence of the shielding of the surface from plasma treatment, when the surface is exposed to a concentration of SUVs, bilayer formation occurs most easily on the regions of substrate that were not protected by the TEM grid. In contrast, the regions that are less hydrophilic (shielded by the copper frame) have insufficient surface energy to promote the fusion of lipid vesicles to the substrate

and the system is trapped in the supported vesicle configuration. Careful tuning of the plasma oxidation time results in the formation of distinct bilayer and monolayer regions. An example of a successful deposition is given in figure 9.1b.

At this stage, it should be stressed that this method is difficult to control and its effects are difficult to reliably reproduce. This is due to the complex interplay between the efficacy of the plasma oxidation treatment, which varies according to humidity and temperature, and the proximity of the TEM grid to the PDMS surface.

Line scans taken across the fluorescence images after normalisation and background subtraction show three distinct intensity levels (figure 9.1c). This suggests the presence of a monolayer region where the copper grid covered the PDMS during oxidation, no lipid in the intervening space, and a bilayer region in the centre of the TEM grid, where the surface was not protected.

The area of the TEM grid under brightfield illumination does not match the area of bilayer in figure 9.1b. This can be explained by a diffraction of the plasma treatment. The effect of the TEM grid is not to cause a perfect shadow on the surface but instead to produce a gradient from high to low surface energy, spanning outward from the centre of each square. It has been shown in chapter 4 that it is possible to form bilayers on partially hydrophilic PDMS and thus imperfect overlap between the TEM grid and the bilayer that forms is expected.

The patterned supported lipid bilayer responds to changing ϵ_{sub} in an analogous way to SLPs. The patterned bilayer slides in the central bilayer region after $\approx 25\%$ substrate dilation and does not open pores. In addition a dark rim can be seen around the bilayer, which is a consequence of the additional substrate area that has become visible due to substrate expansion underneath the bilayer. Upon substrate compression the sliding motion is reversed as in section 6.4, and the patterned bilayer returns to its original position. The dark rim around the bilayer disappears (figures 9.2a and 9.2b).

At pH6 the membrane area is strongly coupled to the substrate area. As a consequence, the membrane ruptures and forms pores in response to increasing substrate area as in chapter 7 (figures 9.2c and 9.2d). The pores are non-circular and appear to be distributed along a particular diagonal across the substrate. This may be rationalised on the basis of nanoscale deposits on the substrate from the TEM
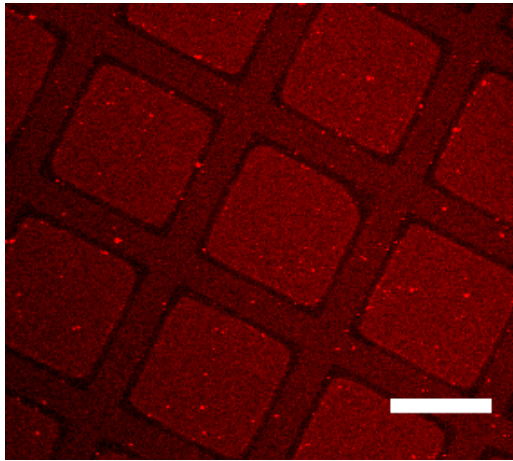
(a) Scale bar 50 μm.
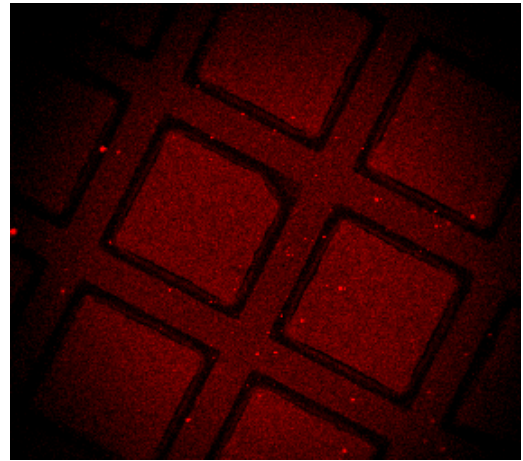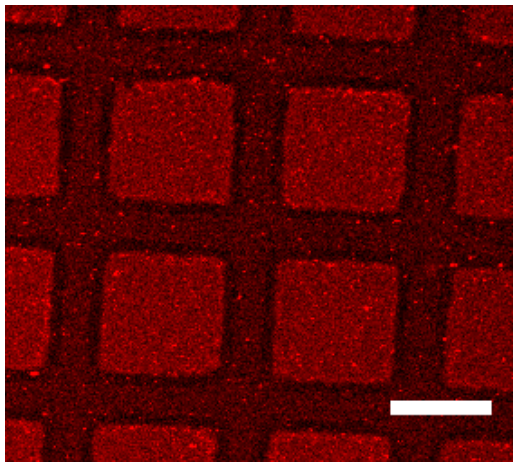
(b) $\epsilon_{sub} \approx 25\%$.

(c) Scale bar 50 μm.
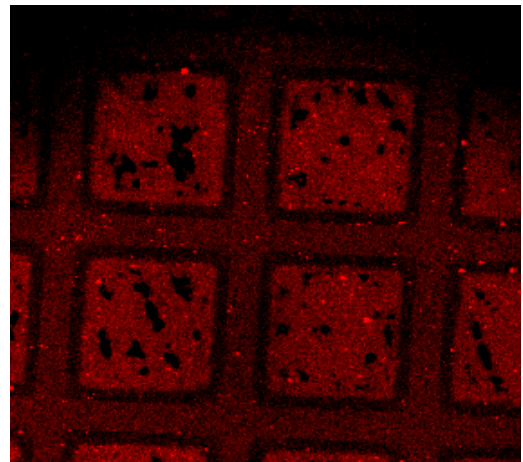
(d) $\epsilon_{sub} \approx 12\%$.

Figure 9.2: A spatially patterned bilayer in a pH 7.5 buffer at $\epsilon_{sub} = 0$ (a) and $\epsilon_{sub} = 25\%$ (b). A spatially patterned bilayer in a pH 6 buffer at $\epsilon_{sub} = 0$ (c) and $\epsilon_{sub} = 12\%$ (d).

grid. These deposits would presumably act to lower the energy required for passage into a stable pore by perturbing the membrane. This would naturally explain the alignment of the pores on the patterned substrate.

Interestingly, close inspection of figure 9.2a reveals more information about how the substrate surface energy organises the membrane response to substrate deformation. Around some of the bilayer squares small protrusions can be identified. These protrusions disappear during substrate expansion when the membrane is sliding and subsequently reappear as the substrate area is compressed. This is in agreement with the observation of lipid tube formation on low surface energy PDMS (chapter 5.4). As the membrane is forced to slide over the region of low surface energy, the change in surface energy allows the bilayer to decouple from the support and project upwards in the form of lipid protrusions; this protrusion formation inhibits further sliding. The same membrane protrusions also appear at lower pH (figure 9.2c), again disappearing and reappearing during substrate expansion and contraction respectively. This suggest that the change in substrate hydrophilicity is the dominant factor in determining the preferred mechanism of stress relaxation in membranes, since the protrusions are observed in both of the pH environments. The low substrate surface energy is the key ingredient for membrane out of plane remodelling.

9.0.1 Conclusions

Here a system in which substrate hydrophilicity may be controlled prior to bilayer deposition is presented. A TEM grid may be used to shield the PDMS surface from the effects of plasma oxidation.

The observed mechanism of substrate stress relaxation (sliding, pore formation or remodelling out the plane) changes as the surface energy varies and agrees with the previous experiments on the substrates prepared using uniform plasma treatment and forming lipid patches *via* the spontaneous fusion of GUVs.

Further work is needed in order to further develop and improve the reproducibility of this method but these experiments could provide new insights into the bilayer-substrate interaction and how this influences membrane behaviour on the elastic substrate.

Chapter 10

Conclusions

A novel device for the support of lipid bilayers has been introduced, described and characterised. The device makes use of the remarkable properties of PDMS. The unique feature of the device is that the substrate is elastic and the substrate area can be reversibly controlled. As a consequence the experiments have assessed the different mechanisms of substrate-stress relaxation available to simple DOPC membranes.

It has been shown that DOPC membranes can be formed on oxidised PDMS and that simple plasma oxidation can be used to create two classes of PDMS substrate for lipid bilayers. The distinction between these two classes of substrate is a zero or non-zero contact angle of a water droplet placed on the surface. If the contact angle is zero then the substrate is classified as hydrophilic; if a contact angle exists then the surface is described as partially hydrophilic. On both classes of substrate membranes have been shown to posses fluidity. This has been demonstrated by fluorescence recovery after photobleaching.

In addition the process of bilayer formation *via* the spontaneous fusion of GUV vesicles has been discussed and shown to depend critically on the substrate hydrophilicity, as well as more delicately on the choice of buffer parameters. Spontaneous GUV fusion has the merit of being accessible to the optical microscope. The entire pathway from vesicle to bilayer can therefore be imaged. Also, the size of the supported membrane patch formed is ideally suited for imaging within the microscope field of view. The ability to record all of the membrane area in experiments provides new insights into supported membrane behaviour.

On partially hydrophilic substrates the membrane is able to mitigate the stress of a changing substrate area by absorbing and projecting lipid protrusions. Such passive means of membrane area regulation have recently being identified in live cells using a similar experimental set-up to the one described here [122]. This mechanism of area regulation therefore sheds new light on the importance of cell-substrate interactions in cell physiology.

On hydrophilic PDMS the response of the membrane to substrate deformation occurs in the plane of the support and has been shown to depend on the choice of buffer pH.

In the low pH regime it is found that the membrane area becomes coupled to the substrate area and the response is dominated by the opening of large hydrophilic pores in the membrane to accommodate the additional support area. These pores have a multitude of interesting applications in supported membrane based devices and research, including targeted drug delivery [157, 124].

In contrast, in the high pH regime it is found that the membrane is able to preserve its integrity by simply allowing the support area to increase or decrease underneath the membrane. This sliding behaviour results in a shear of the interstitial film between the membrane and the substrate. This class of membrane behaviour has implications for the use of supported membrane as coatings to prevent fouling and or improve biocompatibility.

It has additionally been shown that the transition between the membrane-sliding and pore-forming behaviour, on the hydrophilic support, is controlled by the choice of buffer pH and that the transition between the behaviours is reversible and repeatable.

Finally, in an effort to combine the insights gained by studying the GUV fusion process on PDMS substrates with the understanding that emerges from the remodelling of membranes in response of substrate deformation, a first attempt at patterning the bilayer onto a substrate of varying hydrophilicity has been reported. Although requiring refinement, the results are exciting because these results have potential to improve understanding of the importance of the interaction between the membrane and the supporting surface in both biological and technological research efforts.

10.1   Further Work and Unanswered Questions

What follows is a discussion about potential extensions to this work, together with some key measurements that as of yet remain unknown.

Determining the charge of the PDMS

Plasma oxidation produces an unmeasured density of silanol groups at the PDMS surface. The surface pK_a is the pH at which half the surface ionisable groups deprotonate. It would be informative to measure the surface pK_a of PDMS as the pH is varied and as a function of oxidation treatment time. This could be achieved using a streaming potential apparatus.

As well as measuring the surface pK_a it would be desirable to know how the absolute value of the surface charge density of the PDMS varies with plasma oxidation time. From this, estimates of the adhesion energies between the lipid and the substrate could be derived for each set of experiments.

Determining the thickness of the hydration layer

The substrate stress transmitted to the bilayer depends on the thickness of the confined hydration film [44]. The thickness of the hydration film is also a measure of the bilayer substrate adhesion potential W_{ad}. Determination of the interstitial water layer thickness could be achieved through neutron reflectivity. If this value were to change as a function of pH on the hydrophilic substrate, this might explain the transition from the pores to sliding behaviour. Similarly a change in water layer thickness upon transitioning from PDMS of low to high surface energy might explain the transition from remodelling of the membrane out of the substrate plane to the pores and sliding regimes.

Varying the type of lipid

The observed pH dependence suggests that the chemical equilibrium between water and its various dissociation states play an important role in the membrane coupled to the elastic support. Water molecules adjacent to surfaces have been shown, both experimentally and in simulations, to organise themselves in different

ways according to experimental conditions. In addition, water molecules have very different relaxation times in the proximity to phospholipid bilayers [52, 51, 173].

Changing the lipid hydration landscape should therefore influence the membrane behaviour substantially by modifying the cohesive interactions between individual lipids in the membrane. A simple switch from DOPC to 1,2-dioleoyl-sn-glycero-3-phosphoethanolamine (DOPE), could yield interesting behaviour because DOPE lipids can form direct hydrogen bonds without the need for external hydration water as a mediator [152],.

The mechanical properties of lipid membranes are also known to depend on the degree of saturation, cholesterol content, hydrophobic chain length and head group architecture [36, 143, 174].

Systematically varying the lipid type and structure would help discern the importance of lipid cohesion in explaining the behaviour of the membrane patches in response to substrate strain.

Checking for a Change in the Strength of the Membrane as a Function of pH

The literature does not provide a coherent picture of the effect of pH on the yield strength of DOPC lipid membranes. It would be useful to know of any changes in the yield stress properties of the membrane as a function of pH. This would explain both the increased GUV rupture probability at low pH on partially hydrophilic PDMS and the transition from the membrane pore forming to sliding regimes on fully hydrophilic PDMS.

Alternative substrate-bilayer couplings

In the cell the membrane substrate adhesion is heterogeneous and mediated by dynamic ligand receptor couplings. A biofunctionalised PDMS surface that has a density of biotin capped lipids [175] at the surface could be used to reproduce this type of membrane substrate adhesion more faithfully.

The substrate could be coupled to the bilayer *via* ligand-receptor linkages using proteins from the avidin family. This type of membrane substrate coupling could easily be adapted to the device described in this thesis.

The response of this system to substrate deformation could help determine the relative importance of specific versus non-specific substrate adhesion in different membrane-substrate coupling circumstances, furthering understanding the forces felt by the membrane when confined by a surface.

Bibliography

[1]   James A. Rooney. "Hydrodynamic shearing of biological cells". In: *Journal of Biological Physics* 2.1 (1974), pp. 26–40. ISSN: 00920606. DOI: `10.1007/BF02309371`.

[2]   Alberto Moreno-Cencerrado et al. "Investigating cell-substrate and cell–cell interactions by means of single-cell-probe force spectroscopy". In: *Microscopy Research and Technique* 80.1 (2017), pp. 124–130. ISSN: 10970029. DOI: `10.1002/jemt.22706`.

[3]   F. Michor. "What does physics have to do with cancer?" In: *Nature Reviews Cancer* 11.9 (2011), pp. 657–670. ISSN: 1474175X. DOI: `10.1038/nrc3092`. arXiv: `NIHMS150003`.

[4]   Viola Vogel and Michael Sheetz. "Local force and geometry sensing regulate cell functions". In: *Nature Reviews Molecular Cell Biology* 7.4 (2006), pp. 265–275. ISSN: 1471-0072. DOI: `10.1038/nrm1890`. URL: `http://www.nature.com/doifinder/10.1038/nrm1890`.

[5]   Giovanna Tomaiuolo. "Biomechanical properties of red blood cells in health and disease towards microfluidics". In: 051501.2014 (2014), pp. 1–19. DOI: `10.1063/1.4895755`. URL: `http://dx.doi.org/10.1063/1.4895755`.

[6]   Jean-Yves Tinevez et al. "Role of cortical tension in bleb growth". In: *Proceedings of the National Academy of Sciences* 106.44 (2009), pp. 18581–18586. ISSN: 0027-8424. DOI: `10.1073/pnas.0903353106`. eprint: `http://www.pnas.org/content/106/44/18581.full.pdf`. URL: `http://www.pnas.org/content/106/44/18581`.

[7]   S.J. Singer and G.L. Nicolson. "The Fluid Mosaic Model of the Structure of Cell Membranes". In: *Science* 175 (1972), pp. 720–731.

[8]   Markus Deserno. "Mesoscopic membrane physics: Concepts, simulations, and selected applications". In: *Macromolecular Rapid Communications* 30.9-10 (2009), pp. 752–771. ISSN: 10221336. DOI: 10.1002/marc.200900090.

[9]   Nils C. Gauthier, Thomas a. Masters, and Michael P. Sheetz. "Mechanical feedback between membrane tension and dynamics". In: *Trends in Cell Biology* 22.10 (2012), pp. 527–535. ISSN: 09628924. DOI: 10.1016/j.tcb.2012.07.005. URL: http://dx.doi.org/10.1016/j.tcb.2012.07.005.

[10]   David Boal. *Mechanics of the Cell*. Cambridge University Press, 2001. DOI: 10.1017/CBO9780511810954.

[11]   Bidisha Sinha et al. "Cells respond to mechanical stress by rapid disassembly of caveolae". In: *Cell* 144.3 (2011), pp. 402–413. ISSN: 00928674. DOI: 10.1016/j.cell.2010.12.031.

[12]   T. A. Masters et al. "Plasma membrane tension orchestrates membrane trafficking, cytoskeletal remodeling, and biochemical signaling during phagocytosis". In: *Proceedings of the National Academy of Sciences* 110.29 (2013), pp. 11875–11880. ISSN: 0027-8424. DOI: 10.1073/pnas.1301766110. URL: http://www.pnas.org/cgi/doi/10.1073/pnas.1301766110.

[13]   Edward T. Castellana and Paul S. Cremer. "Solid supported lipid bilayers: From biophysical studies to sensor design". In: *Surface Science Reports* 61 (2006), pp. 429–444. ISSN: 01675729. DOI: 10.1016/j.surfrep.2006.06.001.

[14]   L K Tamm and H M McConnell. "Supported phospholipid bilayers." In: *Biophysical journal* 47 (1985), pp. 105–113. ISSN: 00063495. DOI: 10.1016/S0006-3495(85)83882-0.

[15]   Ralf P. Richter, Remi. Berat, and Alain R. Brisson. "Formation of Solid-Supported Lipid Bilayers: An Integrated View". In: 12 (2006), pp. 3497–3505.

[16]   V. Labhasetwar C. Peetla, A. Stine. "Biophysical interactions with model lipid membranes: applications in drug discovery and drug delivery". In: *Mol Pharm.* 6.5 (2009), pp. 1264–1276. ISSN: 1543-8384. DOI: 10.1021/mp9000662. Biophysical.

[17] Motomu Tanaka, Fernanda F. Rossetti, and Stefan Kaufmann. "Native sup-
      ported membranes: Creation of two-dimensional cell membranes on polymer
      supports (Review)". In: *Biointerphases* 3.2 (2008), FA12–FA16. ISSN: 1934-
      8630. DOI: 10.1116/1.2905233. URL: http://avs.scitation.org/doi/10.
      1116/1.2905233.

[18] Erich Sackmann and Motomu Tanaka. "Supported membranes on soft poly-
      mer cushions : fabrication , characterization and applications". In: *Trends
      Biotechnol.* 22.99 (2000), pp. 58–64.

[19] Motomu Tanaka and Erich Sackmann. "Polymer-supported membranes as
      models of the cell surface." In: *Nature* 437.7059 (2005), pp. 656–663. ISSN:
      0028-0836. DOI: 10.1038/nature04164.

[20] Jinwen Zhou et al. "Surface modification for PDMS-based microfluidic de-
      vices". In: *Electrophoresis* 33.1 (2012), pp. 89–104. ISSN: 01730835. DOI: 10.
      1002/elps.201100482.

[21] Tamar Shahal et al. "Poly (dimethylsiloxane) -Coated Sensor Devices for
      the Formation of Supported Lipid Bilayers and the Subsequent Study of
      Membrane Interactions". In: *Langmuir : the ACS journal of surfaces and
      colloids* 24.19 (2008), pp. 11268–11275.

[22] Dennis E Discher. "Tissue Cells Feel and Respon to the Stiffness of Their
      Substrate". In: *Science* 310.5751 (2005), pp. 1139–1143. ISSN: 0036-8075.
      DOI: 10.1126/science.1116995. arXiv: NIHMS150003. URL: http://www.
      sciencemag.org/cgi/doi/10.1126/science.1116995.

[23] Farhang Abbasi, Hamid Mirzadeh, and Ali-Asgar Katbab. "Modification of
      polysiloxane polymers for biomedical applications: a review". In: *Polymer
      International* 50.12 (2001), pp. 1279–1287. ISSN: 0959-8103. DOI: 10.1002/
      pi.783. URL: http://doi.wiley.com/10.1002/pi.783.

[24] Andreu Llobera et al. "Biofunctionalization of PDMS-based microfluidic sys-
      tems". In: *Protocol Exchange* (2011), pp. 1–17. ISSN: 2043-0116. DOI: 10.
      1038/protex.2011.271. URL: http://www.nature.com/protocolexchange/
      protocols/2263.

[25] G.M. Cooper. *The Cell A Molecular Approach*. Second edition. Sinauer Associates, 2000.

[26] Radek Macháň and Martin Hof. "Lipid diffusion in planar membranes investigated by fluorescence correlation spectroscopy". In: *Biochimica et Biophysica Acta - Biomembranes* 1798.7 (2010), pp. 1377–1391. ISSN: 00052736. DOI: `10.1016/j.bbamem.2010.02.014`.

[27] I.W. Hamley. *Introduction to Soft Matter*. Revised edition. Wiley, 2007.

[28] V. A. Parsegian. "Theory of liquid-crystal phase transitions in lipid + water systems". In: *Transactions of the Faraday Society* 62 (1966), pp. 848–860. ISSN: 0014-7672. DOI: `10.1039/tf9666200848`.

[29] W. Helfrich. "Elastic Properties of Lipid Bilayers: Theory and Possible Experiments". In: *Z. Naturforsch* 28.c (1973), p. 6930703.

[30] Markus Deserno. "Fluid lipid membranes: From differential geometry to curvature stresses". In: *Chemistry and Physics of Lipids* 185 (2014), pp. 11–45. ISSN: 00093084. DOI: `10.1016/j.chemphyslip.2014.05.001`.

[31] D Needham and R S Nunn. "Elastic deformation and failure of lipid bilayer membranes containing cholesterol." In: *Biophysical journal* 58.4 (1990), pp. 997–1009. ISSN: 0006-3495. DOI: `10.1016/S0006-3495(90)82444-9`.

[32] E. Evans and W. Rawicz. "Entropy-Driven Tension and Bending Elasticity". In: *Phys rev lett* 64.17 (1990), pp. 2094–2097.

[33] R. Kwok and Evan Evans. "Thermoelasticity of Large Lecithin Bilayer Vesicles". In: *Biophys. J.* 35.September (1981), pp. 637–652.

[34] R Waugh and E.A. Evans. "Thermoelasticity of red blood cell membrane". In: *Biophysical Journal* 26.1 (1979), pp. 115–131. ISSN: 00063495. DOI: `10.1016/S0006-3495(79)85239-X`. arXiv: `10/{\$}26.00` [978-1-4244-7903-0]. URL: `http://linkinghub.elsevier.com/retrieve/pii/S000634957985239X`.

[35] Rumiana Dimova. "Recent developments in the field of bending rigidity measurements on membranes". In: *Advances in Colloid and Interface Science* 208 (2014), pp. 225–234. ISSN: 00018686. DOI: `10.1016/j.cis.2014.03.003`.

[36] W Rawicz et al. "Effect of chain length and unsaturation on elasticity of lipid bilayers." In: *Biophysical journal* 79.1 (2000), pp. 328–339. ISSN: 00063495. DOI: `10.1016/S0006-3495(00)76295-3`.

[37] Marc Fuhrmans et al. "Mechanics of membrane fusion / pore formation". In: *Chem. Phys. Lipids* 185 (2014), pp. 1–20. ISSN: 0009-3084. DOI: `10.1016/j.chemphyslip.2014.07.010`. URL: `http://dx.doi.org/10.1016/j.chemphyslip.2014.07.010`.

[38] D. Peter Tieleman et al. "Simulation of Pore Formation in Lipid Bilayers by Mechanical Stress and Electric Fields". In: *Journal of the American Chemical Society* 125.21 (2003), pp. 6382–6383. ISSN: 0002-7863. DOI: `10.1021/ja029504i`. URL: `http://pubs.acs.org/doi/abs/10.1021/ja029504i`.

[39] Evan Evans et al. "Dynamic Tension Spectroscopy and Strength of Biomembranes". In: *Biophysical Journal* 85.4 (2003), pp. 2342–2350. ISSN: 00063495. DOI: `10.1016/S0006-3495(03)74658-X`. URL: `http://linkinghub.elsevier.com/retrieve/pii/S000634950374658X`.

[40] Evan Evans and Benjamin A. Smith. "Kinetics of hole nucleation in biomembrane rupture". In: *New Journal of Physics* 13 (2011), pp. 0–29. ISSN: 13672630. DOI: `10.1088/1367-2630/13/9/095010`. arXiv: `NIHMS150003`.

[41] Victor Levadny et al. "Rate constant of tension-induced pore formation in lipid membranes." In: *Langmuir : the ACS journal of surfaces and colloids* 29.12 (2013), pp. 3848–52. ISSN: 1520-5827. DOI: `10.1021/la304662p`. URL: `http://www.ncbi.nlm.nih.gov/pubmed/23472875`.

[42] R. P. Rand and V. A. Parsegian. "Hydration forces between phospholipid bilayers". In: *BBA - Reviews on Biomembranes* 988.3 (1989), pp. 351–376. ISSN: 03044157. DOI: `10.1016/0304-4157(89)90010-5`.

[43] S.A. Safran. *Statistical Thermodynamics of Surfaces, Interfaces and Membranes.* First edition. Westview Press, 2003.

[44] Jacob N. Israelachvili. *Intermolecular and Surface Forces.* Third Edition. Elsevier, 2011, p. 706. ISBN: 9780123919274.

[45] John C. Berg. *An Introduction to Interfaces and Colloids: The bridge to the Nanoscience.* World Scientific, 2010.

[46] Udo Seifert and Reinhard Lipowsky. "Adhesion of vesicles". In: *Physical Review A* 42.8 (1990), pp. 4768–4771. ISSN: 10502947. DOI: `10.1103/PhysRevA.42.4768`.

[47] G. T. Linke, R. Lipowsky, and T. Gruhn. "Adhesion of fluid vesicles at chemically structured substrates". In: *European Physical Journal E* 24.3 (2007), pp. 217–227. ISSN: 12928941. DOI: `10.1140/epje/i2007-10232-2`.

[48] Peter S. Swain and David Andelman. "The Influence of Substrate Structure on Membrane Adhesion". In: *Langmuir* 8 (1999), pp. 8902–8914.

[49] J Raedler, H Strey, and E Sackmann. "Phenomenology and Kinetics of Lipid Bilayer Spreading on Hydrophilic Surfaces". In: *Langmuir* 11.11 (1995), pp. 4539–4548. ISSN: 0743-7463. DOI: `10.1021/la00011a058`. URL: `http://pubs3.acs.org/acs/journals/doilookup?in{\_}doi=10.1021/la00011a058`.

[50] Theodore J. Zwang et al. "Formation of supported bilayers on silica substrates". In: *Langmuir* 26.7 (2010), pp. 4598–4601. ISSN: 07437463. DOI: `10.1021/la900181c`.

[51] T Fukuma, M J Higgins, and S P Jarvis. "Direct imaging of individual intrinsic hydration layers on lipid bilayers at Angstrom resolution". In: *Biophysical Journal* 92.10 (2007), pp. 3603–3609. ISSN: 0006-3495. DOI: `DOI10.1529/biophysj.106.100651`.

[52] Michael J Higgins et al. "Structured water layers adjacent to biological membranes." In: *Biophysical journal* 91.7 (2006), pp. 2532–2542. ISSN: 0006-3495. DOI: `10.1529/biophysj.106.085688`. URL: `http://www.sciencedirect.com/science/article/pii/S0006349506719671`.

[53] Jacob N. Israelachvili and H Wennerström. "Role of hydration and water structure in biological and colloidal interactions". In: *Nature* (1996).

[54] Margarita Staykova et al. "Confined bilayers passively regulate shape and stress". In: *Physical Review Letters* 110.January (2013), pp. 1–5. ISSN: 00319007. DOI: `10.1103/PhysRevLett.110.028101`.

[55] R.A.L. Jones. *Soft Condensed Matter: Oxford Master Series In Condensed Matter Physics*. First edition. Oxford University Press, 2002.

[56] J Nissen et al. "Wetting of phospholipid membranes on hydrophilic surfaces - Concepts towards self-healing membranes". In: *European Physical Journal B* 10 (1999), pp. 335–344. ISSN: 14346028. DOI: `10.1007/s100510050862`. URL: `http://www.springerlink.com/index/10.1007/s100510050862`.

[57] Miglena I Angelova and Dimiter S Dimitrov. "Liposome Electro formation". In: *Faraday Discuss. Chem. SO* 81 (1986), pp. 303–311.

[58] Goh Haw Zan et al. "Hemifusion of giant unilamellar vesicles with planar hydrophobic surfaces: a fluorescence microscopy study". In: *Soft Matter* 8 (2012), p. 10877. ISSN: 1744-683X. DOI: `10.1039/c2sm25702e`.

[59] Hélène Bouvrais et al. "Impact of membrane-anchored fluorescent probes on the mechanical properties of lipid bilayers." In: *Biochimica et biophysica acta* 1798.7 (2010), pp. 1333–1337. ISSN: 0006-3002. DOI: `10.1016/j.bbamem.2010.03.026`. URL: `http://dx.doi.org/10.1016/j.bbamem.2010.03.026`.

[60] 2010. URL: `https://www.nature.com/scitable/topicpage/why-are-cells-powered-by-proton-gradients-14373960`.

[61] Yong Zhou and Robert M. Raphael. "Solution pH Alters Mechanical and Electrical Properties of Phosphatidylcholine Membranes: Relation between Interfacial Electrostatics, Intramembrane Potential, and Bending Elasticity". In: *Biophysical Journal* 92.7 (2007), pp. 2451–2462. ISSN: 00063495. DOI: `10.1529/biophysj.106.096362`. URL: `http://linkinghub.elsevier.com/retrieve/pii/S0006349507710500`.

[62] J.S. Easterby R.J. Beynon. *Buffer Solutions; The Basics.* Oxford University Press, Walton Street, Oxford, OX2 6DP: Oxford University Press, 1996.

[63] Urs M. Ferber, Gillian Kaggwa, and Suzanne P. Jarvis. "Direct imaging of salt effects on lipid bilayer ordering at sub-molecular resolution". In: *European Biophysics Journal* 40.3 (2011), pp. 329–338. ISSN: 01757571. DOI: `10.1007/s00249-010-0650-7`.

[64] Georg Pabst et al. "Rigidification of Neutral Lipid Bilayers in the Presence of Salts". In: *Biophysical Journal* 93.8 (2007), pp. 2688–2696. ISSN: 00063495. DOI: `10.1529/biophysj.107.112615`. URL: `http://linkinghub.elsevier.com/retrieve/pii/S0006349507715230`.

[65]   Sergi Garcia-Manyes et al. "Nanomechanics of lipid bilayers: Heads or tails?"
       In: *Journal of the American Chemical Society* 132.37 (2010), pp. 12874–
       12886. ISSN: 00027863. DOI: `10.1021/ja1002185`.

[66]   Catherine C. Logisz and Jennifer S. Hovis. "Effect of salt concentration on
       membrane lysis pressure". In: *Biochimica et Biophysica Acta - Biomembranes*
       1717.2 (2005), pp. 104–108. ISSN: 00052736. DOI: `10.1016/j.bbamem.2005.`
       `10.002`.

[67]   Johannes Schindelin et al. "Fiji: an open-source platform for biological-image
       analysis." In: *Nature methods* 9.7 (2012), pp. 676–82. ISSN: 1548-7105. DOI:
       `10.1038/nmeth.2019`. arXiv: `1081-8693`. URL: `http://www.ncbi.nlm.`
       `nih.gov/pubmed/22743772{\%}0Ahttp://www.pubmedcentral.nih.gov/`
       `articlerender.fcgi?artid=PMC3855844`.

[68]   Dhananjay Bodas and Chantal Khan-Malek. "Hydrophilization and hydropho-
       bic recovery of PDMS by oxygen plasma and chemical treatment-An SEM
       investigation". In: *Sensors and Actuators, B: Chemical* 123.1 (2007), pp. 368–
       373. ISSN: 09254005. DOI: `10.1016/j.snb.2006.08.037`.

[69]   Ryugo Tero. "Substrate effects on the formation process, structure and physic-
       ochemical properties of supported lipid bilayers". In: *Materials* 5.12 (2012),
       pp. 2658–2680. ISSN: 19961944. DOI: `10.3390/ma5122658`.

[70]   Jaroslaw Drelich. "Guidelines to measurements of reproducible contact angles
       using a sessile-drop technique". In: *Surface Innovations* 1.4 (2013), pp. 248–
       254. ISSN: 2050-6252. DOI: `10.1680/si.13.00010`. URL: `http://www.`
       `icevirtuallibrary.com/content/article/10.1680/si.13.00010`.

[71]   Kurt Thorn and Doug Kellogg. "A quick guide to light microscopy in cell
       biology". In: *Mol. Biol. Cell* 27 (2016). DOI: `10.1091/mbc.E15-02-0088`.

[72]   Douglas Murphy. *Fundamentals of Light Microscopy and Electronic Imaging.*
       John Wiley & Sons, Inc., 2001. ISBN: 047125391X.

[73]   Jay T Groves, Raghuveer Parthasarathy, and Martin B Forstner. "Fluores-
       cence imaging of membrane dynamics." In: *Annual review of biomedical en-
       gineering* 10 (2008), pp. 311–338. ISSN: 1523-9829. DOI: `10.1146/annurev.`
       `bioeng.10.061807.160431`.

[74] Joseph R. Lakowicz. *Principles of Fluorescence Spectroscopy Principles of Fluorescence Spectroscopy*. 2006, p. 362. ISBN: 978-0-387-31278-1 (Print) 978-0-387-46312-4 (Online). DOI: `10.1007/978-0-387-46312-4`. arXiv: `arXiv: 1011.1669v3`.

[75] W.W. Webb D. Axelrod, D.E. Koppel, J. Schelessinger, E. Elson. "Mobility Measurement by Analysis of Fluorescence Photobeaching recovery Kinetics". In: *Biophysical journal* 16 (1976), pp. 1055–1069.

[76] D M Soumpasis. "Theoretical analysis of fluorescence photobleaching recovery experiments." In: *Biophysical journal* 41.1 (1983), pp. 95–97. ISSN: 00063495. DOI: `10.1016/S0006-3495(83)84410-5`.

[77] Daniel Blumenthal et al. "Universal Approach to FRAP Analysis of Arbitrary Bleaching Patterns". In: *Nature Publishing Group* 108.2 (2015), pp. 1–9. ISSN: 2045-2322. DOI: `10.1038/srep11655`. URL: `http://dx.doi.org/10.1038/srep11655{\%}5Cnpapers3://publication/doi/10.1038/srep11655`.

[78] Luca Piantanida et al. "Ions Modulate Stress-Induced Nanotexture in Supported Fluid Lipid Bilayers". In: *Biophysical Journal* 113.2 (2017), pp. 426–439. ISSN: 15420086. DOI: `10.1016/j.bpj.2017.05.049`.

[79] Jennifer C. Waters. "Accuracy and precision in quantitative fluorescence microscopy". In: *Journal of Cell Biology* 185.7 (2009), pp. 1135–1148. ISSN: 00219525. DOI: `10.1083/jcb.200903097`.

[80] J. Pascau J.M. Mateos-Pérez. *Image Processing with ImageJ*. First edition. Packt Publishing, 2013.

[81] M.J. Burge W. Burger. *Digital Image Processing: An Algorithmic Introduction Using Java*. First edition. Springer, 2008.

[82] Andrew Grensted. *Otsu Thresholding*. `http://www.labbookpages.co.uk/software/imgProc/otsuThreshold.html`. [Online; accessed 2018-01-08]. 2017.

[83] Nobuyuki Otsu. "A Threshold Selection Method from Gray-Level Histograms". In: *IEEE* 20.1 (1979), pp. 62–66. ISSN: 0018-9472. DOI: `10.1109/TSMC.1979.4310076`.

[84] Wen-Hsiang Tsai. "Document Image Analysis". In: ed. by Lawrence O'Gorman and Rangachar Kasturi. Los Alamitos, CA, USA: IEEE Computer Society Press, 1995. Chap. Moment-preserving Thresholding: A New Approach, pp. 44–60. ISBN: 0-8186-6547-5. URL: http://dl.acm.org/citation.cfm?id=201573.201578.

[85] Tania K. Lind and Marité Cárdenas. "Understanding the formation of supported lipid bilayers via vesicle fusion—A case that exemplifies the need for the complementary method approach (Review)". In: *Biointerphases* 11.2 (2016), p. 020801. ISSN: 1934-8630. DOI: 10.1116/1.4944830. URL: http://avs.scitation.org/doi/10.1116/1.4944830.

[86] Gregory J Hardy, Rahul Nayak, and Stefan Zauscher. "Model cell membranes: Techniques to form complex biomimetic supported lipid bilayers via vesicle fusion." In: *Current opinion in colloid & interface science* 18.5 (2013), pp. 448–458. ISSN: 1359-0294. DOI: 10.1016/j.cocis.2013.06.004. arXiv: NIHMS150003. URL: http://www.ncbi.nlm.nih.gov/pubmed/24031164.

[87] Maria Wallin et al. "Peptide-induced formation of a tethered lipid bilayer membrane on mesoporous silica". In: *European Biophysics Journal* 44.1-2 (2014), pp. 27–36. ISSN: 14321017. DOI: 10.1007/s00249-014-0998-1.

[88] Cunlu Zhao et al. "Extracting local surface charges and charge regulation behavior from atomic force microscopy measurements at heterogeneous solid-electrolyte interfaces". In: *Nanoscale* 7.39 (2015), pp. 16298–16311. ISSN: 2040-3364. DOI: 10.1039/C5NR05261K.

[89] Travers H. Anderson et al. "Formation of Supported Bilayers on Silica Substrates". In: *Langmuir* 25.12 (2009), pp. 6997–7005. ISSN: 0743-7463. DOI: 10.1021/la900181c. URL: http://pubs.acs.org/doi/abs/10.1021/la900181c.

[90] Dimitrios Argyris, David R. Cole, and Alberto Striolo. "Hydration structure on crystalline silica substrates". In: *Langmuir* 25.14 (2009), pp. 8025–8035. ISSN: 07437463. DOI: 10.1021/la9005136.

[91] Joshua A. Jackman et al. "Self-assembly formation of lipid bilayer coatings on bare aluminum oxide: Overcoming the force of interfacial water". In: *ACS*

Applied Materials and Interfaces 7.1 (2015), pp. 959–968. ISSN: 19448252. DOI: `10.1021/am507651h`.

[92] Nam-Joon Cho and Curtis W Frank. "Fabrication of a planar zwitterionic lipid bilayer on titanium oxide". In: *Langmuir* 26.20 (2010), pp. 15706–10. ISSN: 1520-5827. DOI: `10.1021/la101523f`. URL: `http://www.ncbi.nlm.nih.gov/pubmed/20857902`.

[93] Nam Joon Cho et al. "PH-driven assembly of various supported lipid platforms: A comparative study on silicon oxide and titanium oxide". In: *Langmuir* 27.7 (2011), pp. 3739–3748. ISSN: 07437463. DOI: `10.1021/la104348f`.

[94] Selver Ahmed et al. "Hydration repulsion effects on the formation of supported lipid bilayers". In: *Soft Matter* 7.5 (2011), p. 1936. ISSN: 1744-683X. DOI: `10.1039/c0sm01045f`.

[95] Paul S. Cremer and Steven G. Boxer. "Formation and Spreading of Lipid Bilayers on Planar Glass Supports". In: *The Journal of Physical Chemistry B* 103.13 (1999), pp. 2554–2559. ISSN: 1520-6106. DOI: `10.1021/jp983996x`. URL: `http://pubs.acs.org/doi/abs/10.1021/jp983996x`.

[96] Erich Sackmann and Robijn F. Bruinsma. "Cell adhesion as wetting transition?" In: *ChemPhysChem* 3.3 (2002), pp. 262–269. ISSN: 14394235. DOI: `10.1002/1439-7641(20020315)3:3⟨262::AID-CPHC262⟩3.0.CO;2-U`.

[97] C. Tordeux, J. B. Fournier, and P. Galatola. "Analytical characterization of adhering vesicles". In: *Physical Review E - Statistical, Nonlinear, and Soft Matter Physics* 65.4 (2002). ISSN: 15393755. DOI: `10.1103/PhysRevE.65.041912`. arXiv: `0112247 [cond-mat]`.

[98] Holger Schönherr et al. "Vesicle adsorption and lipid bilayer formation on glass studied by atomic force microscopy". In: *Langmuir* 20.26 (2004), pp. 11600–11606. ISSN: 07437463. DOI: `10.1021/la049302v`.

[99] Benjamin L Stottrup, Sarah L Veatch, and Sarah L Keller. "Nonequilibrium behavior in supported lipid membranes containing cholesterol." In: *Biophysical journal* 86.May (2004), pp. 2942–2950. ISSN: 00063495. DOI: `10.1016/S0006-3495(04)74345-3`.

[100] Matthew C. Blosser et al. "Transbilayer Colocalization of Lipid Domains Explained via Measurement of Strong Coupling Parameters". In: *Biophysical Journal* 109.11 (2015), pp. 2317–2327. ISSN: 00063495. DOI: `10.1016/j.bpj.2015.10.031`. URL: `http://linkinghub.elsevier.com/retrieve/pii/S0006349515011066`.

[101] Yong Hoon Kim et al. "Supported lipid bilayer formation by the giant vesicle fusion induced by vesicle-surface electrostatic attractive interaction". In: *Chemical Physics Letters* 420.4-6 (2006), pp. 569–573. ISSN: 00092614. DOI: `10.1016/j.cplett.2006.01.026`.

[102] Chiho Hamai, Paul S Cremer, and Siegfried M Musser. "Single giant vesicle rupture events reveal multiple mechanisms of glass-supported bilayer formation." In: *Biophysical journal* 92.6 (2007), pp. 1988–1999. ISSN: 00063495. DOI: `10.1529/biophysj.106.093831`.

[103] Peter Lenz, Cm Ajo-Franklin, and Sg Boxer. "Patterned supported lipid bilayers and monolayers on poly (dimethylsiloxane)". In: *Langmuir* 26 (2004), pp. 11092–11099. URL: `http://pubs.acs.org/doi/abs/10.1021/la048450i`.

[104] V I Silin et al. "The role of surface free energy on the formation of hybrid bilayer membranes." In: *Journal of the American Chemical Society* 124.49 (2002), pp. 14676–14683. ISSN: 0002-7863. DOI: `Doi10.1021/Ja026585+`. URL: `http://www.ncbi.nlm.nih.gov/pubmed/12465979`.

[105] Kimiko Makino et al. "Temperature- and ionic strength-induced conformational changes in the lipid head group region of liposomes as suggested by zeta potential data". In: *Biophysical Chemistry* 41.2 (1991), pp. 175–183. ISSN: 03014622. DOI: `10.1016/0301-4622(91)80017-L`.

[106] C a Helm, J N Israelachvili, and P M McGuiggan. "Role of hydrophobic forces in bilayers ahesion and fusion". In: *Biochemistry* 31.1987 (1992), pp. 1794–1805.

[107] Christian Sendner et al. "Interfacial water at hydrophobic and hydrophilic surfaces: Slip, viscosity, and diffusion". In: *Langmuir* 25.18 (2009), pp. 10768–10781. ISSN: 07437463. DOI: `10.1021/la901314b`.

[108] Sergi Garcia-Manyes, Gerard Oncins, and Fausto Sanz. "Effect of pH and ionic strength on phospholipid nanomechanics and on deposition process onto hydrophilic surfaces measured by AFM". In: *Electrochimica Acta* 51.24 (2006), pp. 5029–5036. ISSN: 00134686. DOI: `10.1016/j.electacta.2006.03.062`.

[109] Hélène Bouvrais, Lars Duelund, and John H. Ipsen. "Buffers Affect the Bending Rigidity of Model Lipid Membranes". In: *Langmuir* (2013).

[110] Ole G. Mouritsen and Martin J. Zuckermann. "What's so special about cholesterol?" In: *Lipids* 39.11 (2004), pp. 1101–1113. ISSN: 1558-9307. DOI: `10.1007/s11745-004-1336-x`. URL: `https://doi.org/10.1007/s11745-004-1336-x`.

[111] Angelika Kunze et al. "Ion-mediated changes of supported lipid bilayers and their coupling to the substrate. A case of bilayer slip?" In: *Soft Matter* 7.18 (2011), p. 8582. ISSN: 1744-683X. DOI: `10.1039/c1sm05886j`. URL: `http://xlink.rsc.org/?DOI=c1sm05886j`.

[112] Margarita Staykova et al. "Mechanics of surface area regulation in cells examined with confined lipid membranes." In: *Proceedings of the National Academy of Sciences of the United States of America* 108.22 (2011), pp. 9084–9088. ISSN: 0027-8424. DOI: `10.1073/pnas.1102358108`.

[113] Ethan J. Miller, Kislon Voïtchovsky, and Margarita Staykova. "Substrate-led cholesterol extraction from supported lipid membranes". In: *Nanoscale* (2018), pp. –. DOI: `10.1039/C8NR03399D`. URL: `http://dx.doi.org/10.1039/C8NR03399D`.

[114] Reinhard Lipowsky. "Spontaneous tubulation of membranes and vesicles reveals membrane tension generated by spontaneous curvature". In: *Faraday Discussions* (2013), pp. 305–331. ISSN: 1359-6640. DOI: `10.1039/c2fd20105d`.

[115] Aleksey Vishnyakov, Ting Li, and Alexander V. Neimark. "Adhesion of Phospholipid Bilayers to Hydroxylated Silica: Existence of Nanometer-Thick Water Interlayers". In: *Langmuir* 33.45 (2017), pp. 13148–13156. ISSN: 15205827. DOI: `10.1021/acs.langmuir.7b03582`.

[116] Michael M. Kozlov and Leonid V. Chernomordik. "Membrane tension and membrane fusion". In: *Current Opinion in Structural Biology* 33 (2015), pp. 61–67. ISSN: 1879033X. DOI: `10.1016/j.sbi.2015.07.010`. arXiv: `15334406`.

[117] Jianjun Pan et al. "Temperature dependence of structure, bending rigidity, and bilayer interactions of dioleoylphosphatidylcholine bilayers". In: *Biophysical Journal* 94.1 (2008), pp. 117–124. ISSN: 00063495. DOI: `10.1529/biophysj.107.115691`.

[118] Frank Julicher and Reinhard Lipowsky. "Domain-Induced Budding of Vesicles". In: *Physical Review Letters* 70.19 (1993), pp. 2964–2967.

[119] Yonathan Kozlovsky and Michael M. Kozlov. "Membrane fission: Model for intermediate structures". In: *Biophysical Journal* 85.1 (2003), pp. 85–96. ISSN: 00063495. DOI: `10.1016/S0006-3495(03)74457-9`.

[120] Mohammad Rahimi and Marino Arroyo. "Shape dynamics, lipid hydrodynamics, and the complex viscoelasticty of bilayer membranes". In: *Physical Review E - Statistical, Nonlinear, and Soft Matter Physics* 86.1 (2012), pp. 1–15. ISSN: 15393755. DOI: `10.1103/PhysRevE.86.011932`.

[121] Andrew G. Clark et al. "Stresses at the cell surface during animal cell morphogenesis." In: *Current biology : CB* 24.10 (2014), R484–94. ISSN: 1879-0445. DOI: `10.1016/j.cub.2014.03.059`. URL: `http://dx.doi.org/10.1016/j.cub.2014.03.059{\%}5Cnhttp://www.ncbi.nlm.nih.gov/pubmed/24845681`.

[122] Anita Joanna Kosmalska et al. "Physical principles of membrane remodelling during Cell mechanoadaptation". In: *Nature Communications* 8292.10.1038 (2015). DOI: `10.1038/ncomms8292`.

[123] Fredrik Persson et al. "Lipid-Based Passivation in Nano fluidics". In: *Nano letters* 12.5 (2012), pp. 2260–5. ISSN: 1530-6992. DOI: `10.1021/nl204535h`.

[124] Liusheng Zha, Brittany Banik, and Frank Alexis. "Stimulus responsive nanogels for drug delivery". In: *Soft Matter* 7.13 (2011), p. 5908. ISSN: 1744-683X. DOI: `10.1039/c0sm01307b`. URL: `http://xlink.rsc.org/?DOI=c0sm01307b`.

[125] Alf Honigmann et al. "A lipid bound actin meshwork organizes liquid phase separation in model membranes". In: *eLife* 2014.3 (2014), pp. 1–16. ISSN: 2050084X. DOI: `10.7554/eLife.01671`. arXiv: `1402.4608`.

[126] Takeshi Fukuma. "Water distribution at solid/liquid interfaces visualized by frequency modulation atomic force microscopy". In: *Science and Technology of Advanced Materials* 11.March 2017 (2010), p. 033003. ISSN: 1468-6996. DOI: `10.1088/1468-6996/11/3/033003`.

[127] Bongsu Kim et al. "Energy dissipation of nanoconfined hydration layer: Long-range hydration on the hydrophilic solid surface". In: *Scientific Reports* 4 (2014), pp. 1–6. ISSN: 20452322. DOI: `10.1038/srep06499`.

[128] Markus Meuwly, Prashant Kumar Gupta, and Markus Meuwly. "Dynamics and vibrational spectroscopy of water at hydroxylated silica surfaces". In: *Faraday Discussions* 167.0 (2013), pp. 1–18. ISSN: 1359-6640. DOI: `10.1039/C3FD00096F`. URL: `http://dx.doi.org/10.1039/C3FD00096F{\%}5Cnhttp://pubs.rsc.org/en/Content/ArticleLanding/2013/FD/c3fd00096f`.

[129] Matej Kanduč and Roland R. Netz. "From hydration repulsion to dry adhesion between asymmetric hydrophilic and hydrophobic surfaces." In: *Proceedings of the National Academy of Sciences of the United States of America* 112.40 (2015), pp. 12338–43. ISSN: 1091-6490. DOI: `10.1073/pnas.1504919112`. URL: `http://www.pnas.org/content/112/40/12338.abstract{\%}5Cnhttp://www.pnas.org/lookup/doi/10.1073/pnas.1504919112`.

[130] Felix Sedlmeier et al. "Water at polar and nonpolar solid walls". In: *Biointerphases* 3.3 (2008), FC23–39. ISSN: 1559-4106. DOI: `10.1116/1.2999559`. URL: `http://www.ncbi.nlm.nih.gov/pubmed/20408691`.

[131] Peter Jönsson et al. "Mechanical behavior of a supported lipid bilayer under external shear forces." In: *Langmuir : the ACS journal of surfaces and colloids* 25.11 (2009), pp. 6279–86. ISSN: 0743-7463. DOI: `10.1021/la8042268`. URL: `http://www.ncbi.nlm.nih.gov/pubmed/19408897`.

[132] Peter M Kasson and Vijay S Pande. "Molecular dynamics simulation of lipid reorientation at bilayer edges." In: *Biophysical journal* 86.6 (2004), pp. 3744–9. ISSN: 0006-3495. DOI: `10.1529/biophysj.103.029652`. URL: `http://www.`

pubmedcentral.nih.gov/articlerender.fcgi?artid=1304275{\&}tool=
pmcentrez{\&}rendertype=abstract.

[133]   Sven H Behrens and David G Grier. "The charge of glass and silica surfaces".
        In: *Journal of Chemical Physics* 115.14 (2001), pp. 6716–6721. DOI: 10.1063/
        1.1404988. arXiv: 0105149v2 [arXiv:cond-mat].

[134]   P S Swain and D Andelman. "Supported membranes on chemically structured
        and rough surfaces." In: *Physical review. E, Statistical, nonlinear, and soft
        matter physics* 63.5 Pt 1 (2001), p. 051911. ISSN: 1063-651X. DOI: 10.1103/
        PhysRevE.63.051911. arXiv: 0009224 [cond-mat].

[135]   Sabrina Jahn and Jacob Klein. "Hydration Lubrication: The Macromolecular
        Domain". In: *Macromolecules* 48.15 (2015), p. 150715144906006. ISSN: 0024-
        9297. DOI: 10.1021/acs.macromol.5b00327. URL: http://dx.doi.org/10.
        1021/acs.macromol.5b00327.

[136]   Jacob Klein. "Hydration lubrication". In: *Friction* 1.1 (2013), pp. 1–23. ISSN:
        2223-7690, 2223-7704. DOI: 10.1007/s40544-013-0001-7. URL: http://
        link.springer.com/article/10.1007/s40544-013-0001-7{\%}5Cnhttp:
        //link.springer.com/content/pdf/10.1007{\%}2Fs40544-013-0001-
        7.pdf.

[137]   Raya Sorkin et al. "Hydration lubrication and shear-induced self-healing of
        lipid bilayer boundary lubricants in phosphatidylcholine dispersions". In:
        Soft Matter 12 (2016), pp. 2773–2784. ISSN: 1744-683X. DOI: 10.1039/
        C5SM02475G. URL: http://xlink.rsc.org/?DOI=C5SM02475G.

[138]   Magdalena-Carla Corneci et al. "Tribological properties of fluid phase phos-
        pholipid bilayers". In: *Tribology International* 44 (2011), pp. 1959–1968. ISSN:
        0301679X. DOI: 10.1016/j.triboint.2011.08.015.

[139]   Liran Ma et al. "Origins of hydration lubrication." In: *Nature communications*
        6 (2015), p. 6060. ISSN: 2041-1723. DOI: 10.1038/ncomms7060. URL: http:
        //www.ncbi.nlm.nih.gov/pubmed/25585501.

[140]   Roger Oria et al. "Force loading explains spatial sensing of ligands by cells".
        In: *Nature* 552.7684 (2017), pp. 219–224. ISSN: 14764687. DOI: 10.1038/
        nature24662.

[141] Gaël Prado et al. "Viscoelastic Transient of Confined Red Blood Cells". In: *Biophysical Journal* 108.9 (2015), pp. 2126–2136. ISSN: 00063495. DOI: `10.1016/j.bpj.2015.03.046`. URL: `http://linkinghub.elsevier.com/retrieve/pii/S0006349515003082`.

[142] Alejandra Alvarez Albarran et al. "Stimuli-responsive antifouling polyisobutylene-based biomaterials via modular surface functionalization". In: *Journal of Polymer Science, Part A: Polymer Chemistry* 55.10 (2017), pp. 1742–1749. ISSN: 10990518. DOI: `10.1002/pola.28540`.

[143] K Olbrich et al. "Water permeability and mechanical strength of polyunsaturated lipid bilayers." In: *Biophysical journal* 79.1 (2000), pp. 321–7. ISSN: 0006-3495. DOI: `10.1016/S0006-3495(00)76294-1`. URL: `http://www.pubmedcentral.nih.gov/articlerender.fcgi?artid=1300936{\&}tool=pmcentrez{\&}rendertype=abstract`.

[144] F. Brochard-Wyart, P G de Gennes, and O. Sandre. "Transient pores in stretched vesicles:role of leak-out". In: *Physica A* 278 (2000), pp. 32–51.

[145] Eric Olson. "Particle Shape Factors and Their Use in Image Analysis-Part 1: Theory". In: *Journal of GXP Compliance* 15.3 (2011), pp. 85–96. ISSN: 15525791. URL: `http://www.ivtnetwork.com/sites/default/files/ImageAnalysis{\_}01.pdf`.

[146] Mohammad Abu Sayem Karal, Victor Levadnyy, and Masahito Yamazaki. "Analysis of constant tension-induced rupture of lipid membranes using activation energy". In: *Phys. Chem. Chem. Phys.* 18.19 (2016), pp. 13487–13495. ISSN: 1463-9076. DOI: `10.1039/C6CP01184E`. URL: `http://xlink.rsc.org/?DOI=C6CP01184E`.

[147] Sergey A. Akimov et al. "Pore formation in lipid membrane II: Energy landscape under external stress". In: *Scientific Reports* 7.1 (2017), p. 12509. ISSN: 2045-2322. DOI: `10.1038/s41598-017-12749-x`. URL: `http://www.nature.com/articles/s41598-017-12749-x`.

[148] Cynthia a. Stanich et al. "Coarsening dynamics of domains in lipid membranes". In: *Biophysical Journal* 105.July (2013), pp. 444–454. ISSN: 00063495. DOI: `10.1016/j.bpj.2013.06.013`.

[149] O. Sandre, L. Moreaux, and F. Brochard-Wyart. "Dynamics of transient pores in stretched vesicles". In: *Proceedings of the National Academy of Sciences* 96.19 (1999), pp. 10591–10596. ISSN: 0027-8424. DOI: `10.1073/pnas.96.19.10591`. URL: `http://www.pnas.org/cgi/doi/10.1073/pnas.96.19.10591`.

[150] Huey W. Huang, Fang Yu Chen, and Ming Tao Lee. "Molecular mechanism of peptide-induced pores in membranes". In: *Physical Review Letters* 92.19 (2004), pp. 198304–1. ISSN: 00319007. DOI: `10.1103/PhysRevLett.92.198304`.

[151] Piyush Verma, Morgan D. Mager, and N. a. Melosh. "Rough-smooth-rough dynamic interface growth in supported lipid bilayers". In: *Physical Review E - Statistical, Nonlinear, and Soft Matter Physics* 89.1 (2014), pp. 1–5. ISSN: 15393755. DOI: `10.1103/PhysRevE.89.012404`.

[152] E. Orti, J.L. Bredas, and C. Clarisse. *Molecular Biology of the Cell*. Fifth edition. Garland Science, 2002.

[153] Robert J. C. Gilbert, Hagan Bayley, and Gregor Anderluh. "Membrane pores: from structure and assembly, to medicine and technology". In: *Philosophical Transactions of the Royal Society B: Biological Sciences* 372.1726 (2017), p. 20160208. ISSN: 0962-8436, 1471-2970. DOI: `10.1098/rstb.2016.0208`.

[154] Alba Diz-Muñoz, Daniel a. Fletcher, and Orion D. Weiner. "Use the force: Membrane tension as an organizer of cell shape and motility". In: *Trends in Cell Biology* 23.2 (2013), pp. 47–53. ISSN: 09628924. DOI: `10.1016/j.tcb.2012.09.006`.

[155] Bruno Pontes, Pascale Monzo, and Nils C. Gauthier. "Membrane tension: A challenging but universal physical parameter in cell biology". In: *Seminars in Cell and Developmental Biology* 71 (2017), pp. 30–41. ISSN: 10963634. DOI: `10.1016/j.semcdb.2017.08.030`.

[156] Susan Elmore. "Apoptosis: A Review of Programmed Cell Death". In: *Toxicologic Pathology* 35.4 (2007), pp. 495–516. ISSN: 01926233. DOI: `10.1080/01926230701320337`. arXiv: `NIHMS150003`.

[157] Daisuke Matsumoto et al. "Mechanoporation of living cells for delivery of macromolecules using nanoneedle array". In: *Journal of Bioscience and Bioengineering* 122.6 (2016), pp. 748–752. ISSN: 13474421. DOI: `10.1016/j.jbiosc.2016.05.006`.

[158] Víctor García-López et al. "Molecular machines open cell membranes". In: *Nature* 548.7669 (2017), pp. 567–572. ISSN: 14764687. DOI: `10.1038/nature23657`. URL: `http://dx.doi.org/10.1038/nature23657`.

[159] Bengt Kasemo. "Biological surface science". In: *Surface Science* 500.1-3 (2002), pp. 656–677. ISSN: 00396028. DOI: `10.1016/S0039-6028(01)01809-X`.

[160] Joon S. Shim et al. "Formation of lipid bilayers inside microfluidic channel array for monitoring membrane-embedded nanopores of phi29 DNA packaging nanomotor". In: *Biomedical Microdevices* 14.1 (2012), pp. 921–928. ISSN: 1527-5418. DOI: `10.1037/a0038432.Latino`. arXiv: `15334406`.

[161] H Binder and O Zschornig. "The effect of metal cations on the phase behaviour and hydration characteristics of phospholipid membranes". In: *Chem. Phys. Lipids* 115 (2002), pp. 39–61.

[162] Robert Vácha et al. "Mechanism of interaction of monovalent ions with phosphatidylcholine lipid membranes". In: *Journal of Physical Chemistry B* 114.29 (2010), pp. 9504–9509. ISSN: 15205207. DOI: `10.1021/jp102389k`.

[163] William Trewby, Duncan Livesey, and Kislon Voïtchovsky. "Buffering agents modify the hydration landscape at charged interfaces". In: *Soft Matter* (2016), pp. 2642–2651. ISSN: 1744-683X. DOI: `10.1039/C5SM02445E`. URL: `http://xlink.rsc.org/?DOI=C5SM02445E`.

[164] D Leckband and J Israelachvili. *Intermolecular forces in biology.* Vol. 34. 2. 2001, pp. 105–267. DOI: `10.1017/S0033583501003687`.

[165] M G Cacace, E M Landau, and J J Ramsden. "The Hofmeister series: salt and solvent effects on interfacial phenomena." In: *Quarterly Reviews of Biophysics* 30.3 (1997), pp. 241–277. ISSN: 00335835. DOI: `10.1017/S0033583597003363`. URL: `http://journals.cambridge.org/abstract{\_}S0033583597003363`.

[166] J. R. Henriksen and J. H. Ipsen. "Measurement of membrane elasticity by micro-pipette aspiration". In: *European Physical Journal E* 14.2 (2004), pp. 149–167. ISSN: 12928941. DOI: 10.1140/epje/i2003-10146-y.

[167] Kumar Varoon Agrawal et al. "Observation of extreme phase transition temperatures of water confined inside isolated carbon nanotubes". In: *Nature Nanotechnology* 12.3 (2017), pp. 267–273. ISSN: 17483395. DOI: 10.1038/nnano.2016.254. arXiv: caps18.

[168] Alice Sze et al. "Zeta-potential measurement using the Smoluchowski equation and the slope of the current-time relationship in electroosmotic flow". In: *Journal of Colloid and Interface Science* 261.2 (2003), pp. 402–410. ISSN: 00219797. DOI: 10.1016/S0021-9797(03)00142-5.

[169] Ali Eftekhari-bafrooei and Eric Borguet. "Effect of Surface Charge on the Vibrational Dynamics of Interfacial Water". In: (2009), pp. 12034–12035.

[170] J Israelachvili et al. "Recent advances in the surface forces apparatus (SFA) technique". In: *Reports on Progress in Physics* 73.3 (2010), p. 036601. ISSN: 0034-4885. DOI: 10.1088/0034-4885/73/3/036601.

[171] C Drummond, J Israelachvili, and P Richetti. "Friction between two weakly adhering boundary lubricated surfaces in water." In: *Physical review. E, Statistical, nonlinear, and soft matter physics* 67.6 Pt 2 (2003), p. 066110. ISSN: 1063-651X. DOI: 10.1103/PhysRevE.67.066110.

[172] Jianshe Chen and Jason R. Stokes. "Rheology and tribology: Two distinctive regimes of food texture sensation". In: *Trends in Food Science and Technology* 25.1 (2012), pp. 4–12. ISSN: 09242244. DOI: 10.1016/j.tifs.2011.11.006. URL: http://dx.doi.org/10.1016/j.tifs.2011.11.006.

[173] E. A. Disalvo et al. "Structural and functional properties of hydration and confined water in membrane interfaces". In: *Biochimica et Biophysica Acta - Biomembranes* 1778.12 (2008), pp. 2655–2670. ISSN: 00052736. DOI: 10.1016/j.bbamem.2008.08.025.

[174] W Rawicz et al. "Elasticity, strength, and water permeability of bilayers that contain raft microdomain-forming lipids." In: *Biophysical journal* 94.June (2008), pp. 4725–4736. ISSN: 00063495. DOI: 10.1529/biophysj.107.121731.

[175] Bo Huang et al. "Phospholipid biotinylation of polydimethylsiloxane (PDMS) for protein immobilization." In: *Lab on a chip* 6.3 (2006), pp. 369–373. ISSN: 1473-0197. DOI: 10.1039/b515840k.

Appendix A

ImageJ Plugins

A.1 Macro Toolset: Tracking Brightfield Deformation

```
// Brightfield Images -
// 1.) crop Brightfiled, choose 3 features
// 2.) coordinates come from corner of selection rectangle
// 3.) save results table to the Desktop

macro " crop Brightfield [a] " {

        roiManager("reset") ;
        id = getImageID() ;
        msg1 = "select 3 features, add these to the Roi Manager" ;
        waitForUser(msg1) ;
        nRois = roiManager("count") ;
        tNames = newArray("f1","f2","f3")
        for (i=0 ; i<nRois ; i++) {
                roiManager("select",i) ;
                getPixelSize(u,pw,ph) ;
                getSelectionBounds(x0,y0,w,h);
                x = x0*pw ;
```

```
                    y = y0*ph ;
                    print(tNames[i] + "          " +,
                            x + "          " + y + "\n") ;
                    run("Duplicate...", "title="+tNames[i]+" duplicate");
                    roiManager("Deselect") ;
                    selectImage(id);
            }
    }


macro " crop multiple Brightfields [A]   " {

            names = newArray(nImages);
            ids = newArray(nImages);
            roiManager("reset") ;
            msg1 = "select 3 features,
                    add these to the Roi Manager" ;
            waitForUser(msg1) ;
            nRois = roiManager("count") ;
            tNames = newArray("f1","f2","f3")

            for (i=0; i < ids.length; i++){
                    selectImage(i+1);
                    ids[i] = getImageID();
                    names[i] = getTitle();
                    }


            Array.print(names) ;


            for (ii=0; ii<names.length; ii++) {
                    if (endsWith(names[ii], "BF.tif")){
                            print(names[ii]);
                            extractROIs(names[ii]) ;
```

```
                    }

                    }


        function extractROIs(window) {

                for (j=0 ; j<nRois ; j++) {

                        roiManager("select",j) ;

                        selectWindow(window) ;

                        getPixelSize(u,pw,ph) ;

                        getSelectionBounds(x0,y0,w,h);

                        x = x0*pw ;

                        y = y0*ph ;

                        print(tNames[j] + "          " + x +,

                            " " + y + "\n") ;

                        run("Duplicate...", "title="+,

                                tNames[j]+"-"+window,

                                +" duplicate");

                        roiManager("Deselect") ;

                        selectWindow(window) ;

                        }

                }


}



macro " min-max-blur [b] " {


        iD = getImageID();

        T = getTitle() ;

        selectImage(iD);

        run("Duplicate...", "title=bluR duplicate");

        selectWindow("bluR")
```

```
        id2 = getImageID() ;

        rad = "20" ;

        // rad = toString(getNumber("Radius of Filters: ",2)) ;

        run("Minimum...", "radius="+rad+" stack");

        run("Maximum...", "radius="+rad+" stack");

        run("Gaussian Blur...", "sigma="+rad+" stack");

        imageCalculator("Subtract create stack", iD,id2);

        selectImage(id2) ;

        close();

        selectWindow("Result of "+T) ;


}


macro " collect data [c] " {


        msg2 = "Determine minimum feature size: " ;

        waitForUser(msg2) ;

        roiManager("reset") ;

        minSize = toString(getNumber("minimum feature size: ",3)) ;

        run("Analyze Particles...", "size="+minSize+",
                -Infinity display exclude clear add stack ") ;


}


macro " save the results to desktop [d] " {


        string = getString("Name for the coordinate file: ",".xls");

        // string = string+".xls" ;

        saveAs("Results",
                "/Users/liamstubbington/Desktop/"+string);

        // adjust path accordingly
```

```
}


macro " save the log to desktop [f] " {


        string = getString(\Name for the origin file: \.".xls") ;
        saveAs("Log", "/Users/liamstubbington/Desktop/+string) ;


}


macro " median duplicate & threshold [m] " {


        den = getNumber("substack density: ", 3) ;
        D = toString(den) ;
        N = toString(nSlices) ;
        run("Make Substack...", "frames=1-"+N+"-"+D);
        run("Median...", "radius=2 stack");
        setAutoThreshold("Default dark");
        setOption("BlackBackground", false);
        run("Convert to Mask", "method=Default,
                background=Dark calculate");


}


macro " invert LUT [l] " {
        run("Invert LUT");
}


macro " set scale [s] " {


        s = toString(getNumber("microns per pixel: ",0.32)) ;
        run("Set Scale...", "distance=1 known="+s,
```

```
          +" pixel=1 unit=micron");
```

```
}
```

A.2   Macro Toolset: Pre-Processing Fluorescence Images

```
// tool kit for preprocessing images
macro " [s] smooth and apply particle analysis " {

        run("Smooth", "stack");
        setAutoThreshold("Default");
        setOption("BlackBackground", false);
        run("Convert to Mask",
                "method=Default background=Default calculate");
        run("Invert LUT");
        run("Analyze Particles...",
                "size=500-Infinity display exclude
                        clear include add stack");

}


macro " [e] enhance contrast of all open images " {

        for (i=0; i<nImages; i++){
                selectImage(i+1);
                run("Enhance Contrast", "saturated=0.35");
        }
        print("Done!");

}
```

```
macro " [l] data from stack - stack profiler " {


    if (!(selectionType()==0 ||
                    selectionType==5
                            ||selectionType==6))
    exit("Line or Rectangle Selection Required");
    setBatchMode(true);
    run("Plot Profile");
    Plot.getValues(x, y);
    run("Clear Results");
    for (i=0; i<x.length; i++)
        setResult("x", i, x[i]);
    close();
    n = nSlices;
    for (slice=1; slice<=n; slice++) {
        showProgress(slice, n);
        setSlice(slice);
        profile = getProfile();
        sliceLabel = toString(slice);
        sliceData = split(getMetadata("Label"),"\n");
        if (sliceData.length>0) {
            line0 = sliceData[0];
            if (lengthOf(sliceLabel) > 0)
                sliceLabel =
                        sliceLabel+ " ("+ line0 + ")";
        }
        for (i=0; i<profile.length; i++)
            setResult(sliceLabel, i, profile[i]);
    }
    setBatchMode(false);
    updateResults;
```

```
}


macro " extracting contour coordinates " {


        // modify output format
        function printArray(x,title,j) {
                string="";
           for (i=0; i<lengthOf(x); i++) {
                if (i==0) {
                    string=string+title+toString(j)+"\t"+x[i];
                }
                else {
                    string=string+"\t"+x[i];
                        }
            }
    string = string+"\n" ;
    print(string);
        }


        function reScale(X,SF) {
                Y = newArray(lengthOf(X)) ;
                for (ii=0; ii<lengthOf(X); ii++) {
                        Y[ii] = (X[ii])*SF ;
                }
                return Y ;
        }


        for (j=1; j<=nSlices; j++) {
                setSlice(j) ;
                roiManager("Select",j-1);
                // roi = slice - 1
                // run("Interpolate") ;
```

```
            getPixelSize(u,pw,ph) ;

            getSelectionCoordinates(x0,y0) ;

            N = lengthOf(x0) ;

            titleX = "X_" ;

            titleY = "Y_" ;

            x0 = reScale(x0,pw) ;

            y0 = reScale(y0,ph) ;

            printArray(x0,titleX,j) ;

            printArray(y0,titleY,j) ;

        }


}


macro " [o] Otsu threshold the first frame " {


        run("Duplicate...", "title=firstFrame");
        setAutoThreshold("Default");
        run("Convert to Mask"); // OTSU
        getPixelSize(unit,pw,ph,pd) // Calibration
        print("Unit =
                "+unit+"           width =,
                    "+pw+"           height = "+ph)
        run("Invert LUT");
        run("Analyze Particles...", "pixel display clear summarize add");


}


macro " [m] median filter and threshold " {


        run("Duplicate...", "title=median.tif duplicate");
        rad = toString(getNumber("Radius of Filter: ",2))
```

```
        run("Median...", "radius="+rad+" stack");

        setAutoThreshold("Default dark");

        //run("Threshold...");

        setOption("BlackBackground", false);

        run("Convert to Mask", "method=Default
                background=Dark calculate");


}


macro [d] delete outside attached ROI " {


        for (j=1; j<=nSlices; j++) {

                setSlice(j) ;

                roiManager("Select",j-1); /

                // roi = slice -1

                setBackgroundColor(0, 0, 0);

                run("Clear Outside", "slice");

        }


}


macro " [b] background subtraction " {


        iD = getImageID();

        backSub(iD) ;


        function backSub(iD) {

                selectImage(iD);

                run("Duplicate...",
                        "title=bluR duplicate");

                selectWindow("bluR")

                rad = getNumber("Radius of Filters: ",10) ;
```

```
            rad = toString(rad) ;

            run("Minimum...", "radius="+rad+" stack");

            run("Maximum...", "radius="+rad+" stack");

            run("Gaussian Blur...", "sigma="+rad+" stack");

            imageCalculator("Subtract create stack", iD,"bluR");

            selectWindow("bluR") ;

            close();


}
```

A.3   Macro: Extracting Feature Areas

```
// threshold cropped images

// run particle analysis


macro {

        title = getTitle() ;

        selectWindow(title);


        // background subtraction

        rad = toString(getNumber("Radius of Filters: ",20)) ;

        run("Duplicate...", "title=backG duplicate");

        run("Minimum...", "radius="+rad+" stack");

        run("Maximum...", "radius="+rad+" stack");

        run("Gaussian Blur...", "sigma="+rad+" stack");

        selectWindow(title);

        imageCalculator("Subtract create stack", title,"backG");


        // tidy desktop

        selectWindow("backG");

        close();

        selectWindow(title);
```

```
        close();


        // Thresholding
        selectWindow("Result of "+title);
        run("Threshold...");
        waitForUser("Adjust the sliders") ;
        setOption("BlackBackground", false);
        run("Convert to Mask", "method=Default
                background=Light");
        // Smooth and rethreshold
        run("Smooth", "stack");
        run("Threshold...");
        waitForUser("Adjust the sliders again") ;
        run("Convert to Mask", "method=
                Default background=Light");


        // save the binary stack
        newTitle = getString("Title of binary stack: ",
                ".tif") ;
        run("Save",
                "save=/Users/liamstubbington/Desktop/"
                        +newTitle);


        // Apply particle analysis
        run("Set Measurements...", "area center
                perimeter shape stack nan
                        redirect=None decimal=3");
        run("Analyze Particles...", "size=0-Infinity
                display exclude clear
                        include summarize
                                add stack");
} // end Macro
```

Appendix B

Device Assembly

The device assembly procedure is shown schematically in figure B.1 and is summarised in the following list:

- Clean patterned silicon wafer by washing with copious IPA and DI.

- Mix PDMS elastomer with curing agent at a weight ratio of 10:1, remove gas from PDMS mixture by vacuum dessication.

- Fill Petri dish containing patterned silicon wafer with uncured PDMS and spin coat remaining uncured PDMS onto clean petri dish. Use 10 s at 500 rpm followed by 120 s at 2000 rpm.

- Cure PDMS overnight at 50 °C.

- Cut out device from patterned silicon wafer and punch holes in either ends of each channel using the biopsy punch.

- Plasma bond the device to the PDMS thin film spin coated onto the petri dish. Use a pressure of 1 mBar and an exposure time of 30 s on the plasma oxidiser to achieve bonding.

- Clean thick microscope slide (glass) with IPA and dry thoroughly under nitrogen flux. Cut the device from the spin coated PDMS and bond the side with open channels to the clean glass slide.

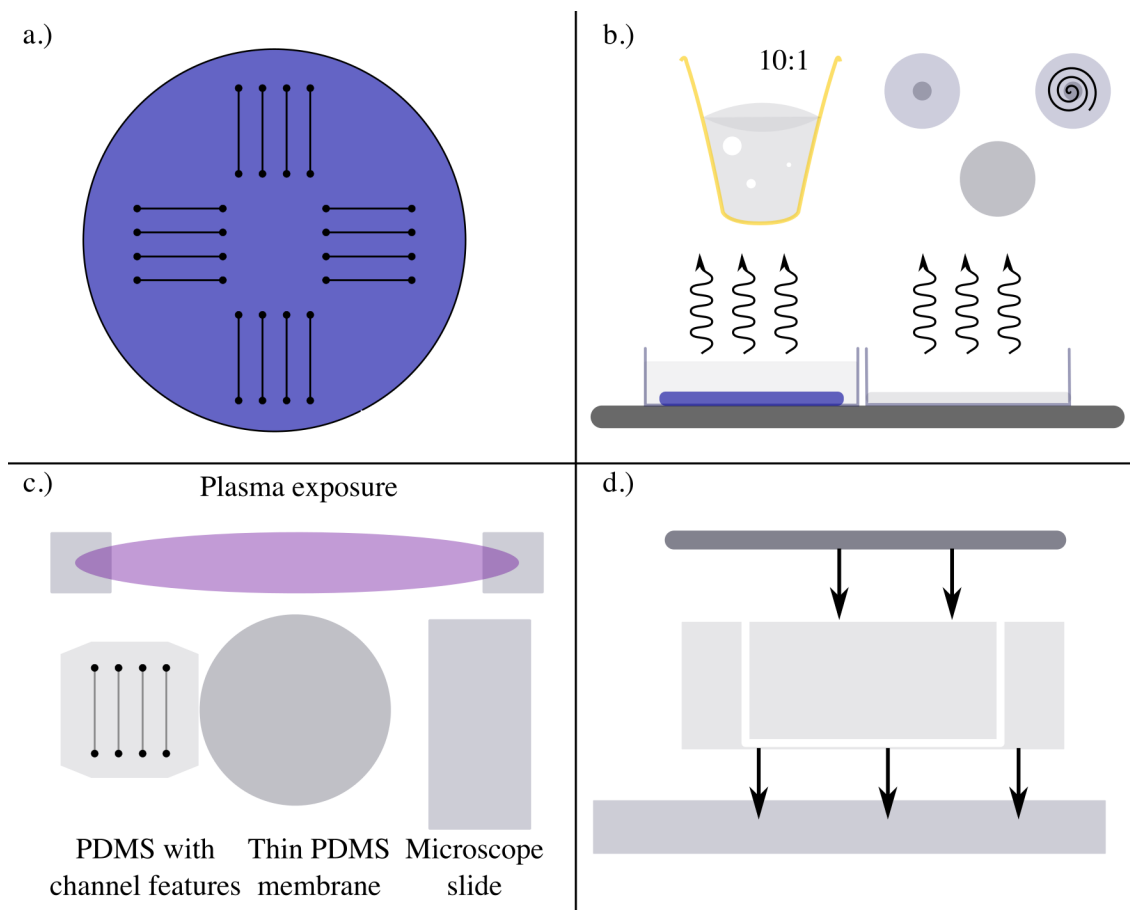- Place device on hot plate for approximately 180 s to finalise bonding.

Figure B.1: a.) Patterned silicon wafer. This is used as a master mould for the microfluidic channels. b.) PDMS is mixed in a 10:1 elastomer to curing agent ratio, degassed and spin coated onto clean Petri dishes. Uncured PDMS is used to cover the silicon master in (a) and left to cure overnight at 55 °C. (c) The device is cut from the cured PDMS and exposed to a low pressure oxygen plasma to activate the surface. (d) The device pieces are assembled. The glass slide forms the base of the channels and the thin PDMS sheet is bonded to the channel exits.

- Break the PDMS thin film at one end of the channel and insert tubing. Device is now ready for bilayer formation and subsequent use.

To ensure good bonding it is sometimes necessary to gently press the two activate surfaces into close contact to squeeze out any air caught between the surfaces. Care must be taken to avoid collapsing the channels when doing this.

Appendix C

Preparing Buffers of Constant Ionic Strength

The calculation for preparing buffers at constant ionic strength can be summarised as follows:

- Choose the ionic strength, I_{total}, of the experiment.

- Choose a buffer with pKa close to the pH at which the experiment is to be conducted.

- Calculate pK'_a. Adjust for temperature and ionic strength corrections.

- Use equation 3.2c to determine the ratio of conjugate acid to base.

- Calculate the ionic strength contribution of the buffer and the counterions, I_{buffer}.

- Determine the concentration NaCl required in order to achieve the desired ionic strength $I_{total} = I_{buffer} + I_{salt}$.

- Prepare the buffer by diluting concentrated stocks in the appropriate proportions.

Appendix D

Measuring the Point Spread Function of the Microscope

A consequence of the finite size of the objective lens is that a point source of light will spread into a pattern known as the PSF.

$$d_{xy} = 0.61\lambda/NA \tag{D.1a}$$

$$d_{xz} = 2n\lambda/NA^2 \tag{D.1b}$$

The Rayliegh criterion is chosen by convention as the minimum distance by which two objects must be displaced in real space in order to be resolved. This is equivalent to the minimum size a sub-resolution object will appear when imaged and is given by equation D.1a in the image plane and along the optical axis by equation D.1b. By imaging an object that is below the resolution limit of the microscope, it is possible to image the PSF of the microscope. Figure D.1 displays the diffraction limited image of a 500 nm fluorescent bead using the $60\times$ oil immersion lens. The maximum spatial resolution of this lens at this illumination wavelength is ≈ 199.8 nm in the plane and 666 nm in the lateral direction. The image is well resolved in the XY plane but spreads considerably in the XZ projection. An asymmetry in the light distribution along the optical axis is also visible, which can be attributed to spherical aberration.
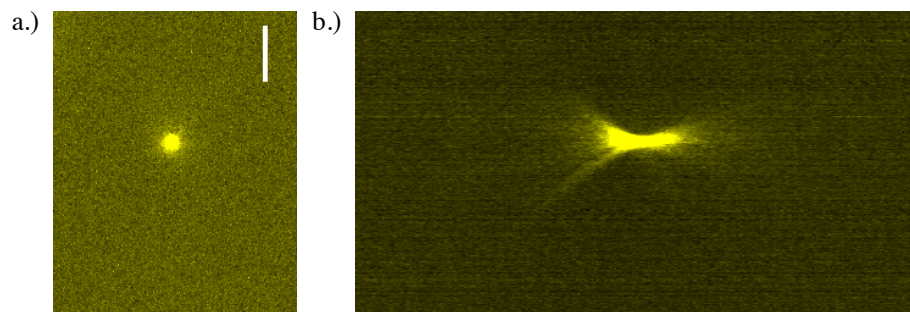
Figure D.1: (a) A single 500nm fluorescent bead imaged with the inverted Nikon Ti using the 60X 1.49NA oil immersion lens, scale bar 5μm. (b) XZ projection of the bead showing the orthogonal diffraction pattern.